NeuroImage 297 (2024) 120685

Contents lists available at ScienceDirect

NeuroImage

journal homepage: www.elsevier.com/locate/ynimg

Review

Systematic review and meta-analysis of automated methods for quantifying enlarged perivascular spaces in the brain

Jennifer M.J. Waymont [a,b], Maria del C. Valdés Hernández [a,b,*], José Bernal [a,b,c,d], Roberto Duarte Coello [a,b], Rosalind Brown [a,b], Francesca M. Chappell [a,b], Lucia Ballerini [e], Joanna M. Wardlaw [a,b]

[a] Centre for Clinical Brain Sciences, the University of Edinburgh, Chancellor's Building, 49 Little France Crescent, Edinburgh EH16 4SB, UK
[b] UK Dementia Research Institute Centre at the University of Edinburgh, UK
[c] German Centre for Neurodegenerative Diseases (DZNE), Germany
[d] Institute of Cognitive Neurology and Dementia Research, Otto-von-Guericke University Magdeburg, Germany
[e] University for Foreigners of Perugia, Perugia, Italy

ARTICLE INFO

Keywords:
Perivascular spaces
Virchow-Robin spaces
Deep learning
Frangi filter
Thresholding
Image processing
Automatic image segmentation
Cerebral small vessel disease
Cerebrovascular disease
Systematic review

ABSTRACT

Research into magnetic resonance imaging (MRI)-visible perivascular spaces (PVS) has recently increased, as results from studies in different diseases and populations are cementing their association with sleep, disease phenotypes, and overall health indicators. With the establishment of worldwide consortia and the availability of large databases, computational methods that allow to automatically process all this wealth of information are becoming increasingly relevant. Several computational approaches have been proposed to assess PVS from MRI, and efforts have been made to summarise and appraise the most widely applied ones. We systematically reviewed and meta-analysed all publications available up to September 2023 describing the development, improvement, or application of computational PVS quantification methods from MRI. We analysed 67 approaches and 60 applications of their implementation, from 112 publications. The two most widely applied were the use of a morphological filter to enhance PVS-like structures, with Frangi being the choice preferred by most, and the use of a U-Net configuration with or without residual connections. Older adults or population studies comprising adults from 18 years old onwards were, overall, more frequent than studies using clinical samples. PVS were mainly assessed from T2-weighted MRI acquired in 1.5T and/or 3T scanners, although combinations using it with T1-weighted and FLAIR images were also abundant. Common associations researched included age, sex, hypertension, diabetes, white matter hyperintensities, sleep and cognition, with occupation-related, ethnicity, and genetic/hereditable traits being also explored. Despite promising improvements to overcome barriers such as noise and differentiation from other confounds, a need for joined efforts for a wider testing and increasing availability of the most promising methods is now paramount.

1. Introduction

Perivascular spaces (PVS), also referred to as 'Virchow-Robin spaces' (VRS), are fluid-filled cavities surrounding the blood vessels of the brain. PVS are thought to facilitate the uptake of cerebrospinal fluid (CSF) and the removal of metabolic waste products from the brain, but the precise involvement in these processes in humans remains elusive (Wardlaw et al., 2020). PVS are increasingly visible in brain imaging or at autopsy as they become enlarged. Enlarged PVS are associated with increased age (Francis et al., 2019), other markers of small vessel disease (SVD) (Duering et al., 2023; Wardlaw et al., 2013), and may be more prevalent in individuals with vascular risk factors (e.g., hypertension) (Zhu et al., 2010). A high burden of enlarged PVS may be associated with worse brain health outcomes, including increased risk of vascular dementia (more so than Alzheimer's disease (AD) (Smeijer et al., 2019) and stroke (Debette et al., 2019).

PVS appear as ovoid or tubular structures, with bright (hyperintense) signal in T2-weighted (T2w) magnetic resonance imaging (MRI) and

* Corresponding author at: Centre for Clinical Brain Sciences, the University of Edinburgh, Chancellor's Building, 49 Little France Crescent, Edinburgh EH16 4SB, UK.
E-mail address: m.valdes-hernan@ed.ac.uk (M.C. Valdés Hernández).

https://doi.org/10.1016/j.neuroimage.2024.120685
Received 18 March 2024; Received in revised form 20 May 2024; Accepted 10 June 2024
Available online 22 June 2024

dark (hypointense) signal in T1-weighted (T1w) MRI, and are occasionally visible on fluid-attenuated inversion recovery (FLAIR) imaging (Duering et al., 2023; Wardlaw et al., 2013). Larger ovoid PVS may appear similar to lacunes—also round CSF-filled cavities and thus with similar signal characteristics to PVS (Duering et al., 2023; Valdés Hernández et al., 2013). PVS may also coalesce with one another forming clusters or irregular strings, exhibit tortuosity, have irregular diameters, and may traverse adjacent imaging slices, complicating their quantification when using multiple 2D slices from images with anisotropic voxels, commonly acquired in clinical practice.

Several automated and semi-automated computational pipelines and methods have been developed to quantify PVS. These methods are heterogeneous in terms of their implementation, validation, and application (Barisano et al., 2022a; Moses et al., 2023; Pham et al., 2022). The principles and drawbacks of some of these methods have been summarised previously (Barisano et al., 2022a; Moses et al., 2023; Pham et al., 2022), and suggestions about further requirements to increase the understanding of PVS by means of their computational assessment using MRI have been drawn (Pham et al., 2022). But there has been also a wealth of computational developments to either enhance performance of previously developed methods, establish their limits of validity, or reduce noise effects, or increase the accuracy of their output, which have not been summarised or reviewed. Neither has this wealth of information been systematically identified or meta-analysed.

The relevance of PVS has become increasingly evident in areas not studied before such as in relation to the occlusion of sinonasal cavities (Sáenz de Villaverde Cortabarría et al., 2023; Valdés Hernández et al., 2024b), in patients with the metabolic syndrome (Hayden, 2023), or in patients with amyotrophic lateral sclerosis (Schreiber et al., 2023) and, with it, the efforts in improving the accuracy of the currently accepted as state-of-the-art computational methods to assess them in the presence of confounding pathology such as white matter hyperintensities (WMH) or lacunes. Consequently, we systematically reviewed and meta-analysed the literature in an attempt to fill this void. In this systematic literature review of (semi-/fully-) automated quantification of PVS, we not only identify and meta-analyse the data from the PVS quantification methods that have been developed, and summarise how they have been applied in studies of PVS associations with health and lifestyle indicators, but also analyse the improvements to these methods, and the impact of the computational efforts around this topic.

2. Methods

2.1. Protocol registration

We registered this systematic review protocol with the International Prospective Register of Systematic Reviews (PROSPERO), registration number: CRD42022359951 (September 2022). We planned to meta-analyse estimates where methodological and clinical characteristics of contributing studies were similar.

2.2. Search strategy

We searched PubMed, Web of Science, and Google Scholar for literature published between January 1990 and September 2023. We also included any hand-selected papers identified from references in relevant literature reviews. Three reviewers (JMJW, MCVH, and JB) conducted the literature search. Each paper was assessed by two reviewers and discrepancies were resolved by discussion. After running pilot searches, we decided on the following search terms (Table 1).

2.3. Inclusion and exclusion criteria

We included studies that described the development, improvement, or application of computational (i.e., semi-/automated) PVS quantification methods in human brain MRI.

Table 1
Search strategy.

Grouping	Terms
#1	"Perivascular spaces" OR "PVS" OR "EPVS" OR "Virchow-Robin spaces" OR "VRS"
#2	"Enlarged" OR "Dilated" OR "Visible" OR "Dysfunction" OR "Enlargement" OR "Visibility" OR "Dilation"
#3	#1 AND #2
#4	Comput* OR "Segmentation" OR Quantif* OR Algorithm* OR "Estimation" OR Automat* OR Semi-automat* OR Semiauto*

Search: #3 AND #4

Exclusion criteria included records without accompanying full-text; studies not reported in English; animal model/pre-clinical studies; studies of PVS using only visual or manual (i.e., non-computational) PVS quantification; studies reporting computational lesion quantification that has not been applied to PVS; studies reporting results from the application of a computational PVS quantification methods but which did not cite or describe the PVS quantification method in-text or in a prior publication or provide any detail. Studies on non-parenchymal fluid dynamics and glymphatic clearance function metrics were also excluded.

2.4. Data extraction and risk of bias assessment

Six reviewers (JMJW, JB, RDC, RB, LB, and MCVH) extracted the data. To cross-check data entry, a reviewer (MCVH) performed double extraction independently and blind to extraction results. We grouped studies into 'method development' (i.e., the paper focuses primarily on the development and validation of a new proposal for identifying, quantifying, or segmenting PVS), 'improvement/validation' (i.e., the paper either provides evidence of a certain PVS quantification issue or proposes an approach to deal with it), and 'application' (i.e., the paper uses a previously presented approach to assess PVS to analyse results in relation to clinical data) categories, and extracted relevant data accordingly. For all studies, we extracted data relating to year of publication, authors, MR sequences/field strengths, population type and sample size. For 'method development' and 'improvement/validation' studies, we extracted data relating to pre-processing steps, reference standards, computational PVS method used, and accuracy and/or validation results. For 'application' studies, we additionally extracted more detailed information on population type, variables assessed in relation to PVS burden, and results.

We conducted a risk of bias assessment on included studies, based on the QUADAS-2 quality assessment tool (Whiting et al., 2011). Risk of bias plots were produced using the Risk of Bias Visualization tool (McGuinness and Higgins, 2020).

2.5. Statistical analysis

We conducted frequency analyses for the data extracted, and tabulated the results. For categorical variables (e.g., computational approach, MRI sequences, etc.), possible values were coded to enable the frequency analyses. Forest plots were generated using MedCalc (https://www.medcalc.org/). For articles reporting correlation coefficients, fixed effects were determined using a Fisher Z transformation of these coefficients. The random effects model (DerSimonian and Laird, 1986) general estimate was given after analysing heterogeneity using the I^2 and Cochran's Q statistics (Higgins et al., 2003). We also used bar charts to facilitate comparability in the numeric results.

3. Results

3.1. Search results

We identified 2978 potentially relevant records. Before screening,

we removed 354 results because they were duplicates or were not in English. During title and abstract screening, we screened titles and abstracts of 2624 records, and excluded 2427 of them. We sought retrieval of the remaining 197. Among these, five were not accessible either publicly or via our institutional library, five were conference abstracts, and two considered PVS quantification for histology samples. Therefore, 185 studies were ultimately assessed for eligibility. From them, 73 studies were ineligible and 112 studies that met our criteria were included in this review. A flow chart of the identification and screening process is provided in Fig. 1.

3.2. Overview of included studies

Of the 112 included studies, 45 fitted under 'method development', eight under 'improvement', and 59 under 'application'. Four separate PVS quantification methods participated in the Vascular Lesions Detection Challenge 2021, as documented in Sudre et al. (2022). We treat them as four distinct records, thus increasing the count of 'method development' studies to 48, and the total number of studies to 115. Overviews of all included studies within these three categories are presented in their respective sections (method development: 3.3, Table 7; improvement: 3.4, Table 9; application: 3.5, Table 10).

3.2.1. Publication timeline

The earliest record identified was published in 2002 (Kruggel et al., 2002). Method development publications became more prevalent from around 2016 onwards reaching a peak in 2019 (16.67% from all publications in this category), and publications applying computational PVS

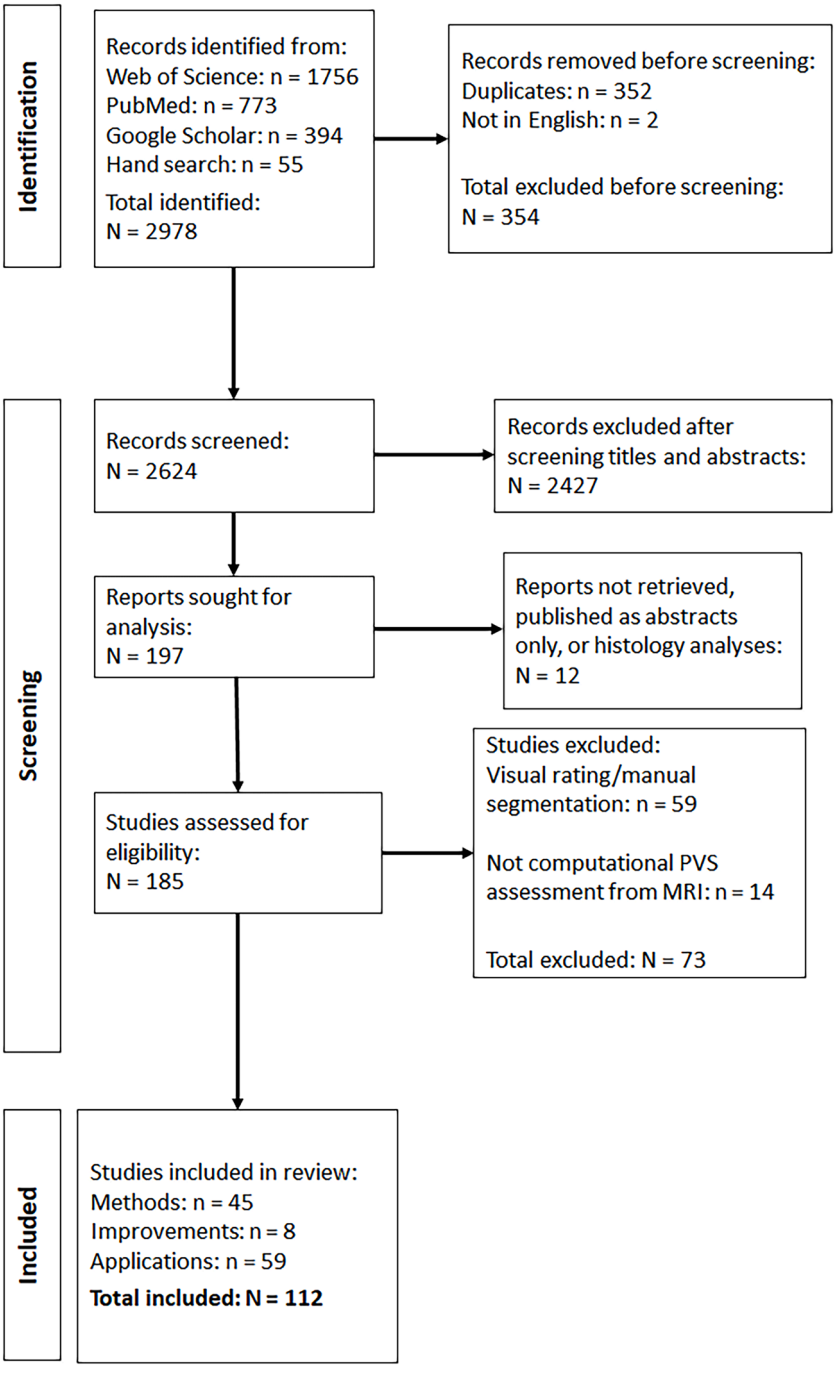

Fig. 1. Flow chart of identification, screening, and selection process.

quantification increased from around 2020 (Fig. 2). Supplementary Table 1 provides a breakdown of publications by type and year.

3.2.2. Populations and sample sizes

Clinical (i.e., patient) and non-clinical (e.g., healthy volunteers, community cohorts) samples have been used in the development, improvement, and application of computational PVS quantification methods, with non-clinical samples (e.g., community-dwelling cohorts) forming the largest proportion by a small margin in 'method developments' and 'improvement' groups. Four sources describing methods (Uchiyama et al., 2008, 2009; Zhang et al., 2016, 2017) did not specify the type of population. Table 2 shows population type overall and by method/improvement/application categories. From the 51 studies that included a clinical sample, 23 included a control population. From the clinical samples, patients with cerebrovascular or neurodegenerative diseases were more represented than patients with psychiatric conditions, communicable diseases, or genetic diseases.

Age groups of populations ranged from children and adolescents through to older adults. Studies comprising only older adults (60+ years) and population studies including adults from 18 years old onwards prevailed. Ten studies (predominantly method development studies) did not provide information about participants' age. Table 3 shows population age groupings used in all and each of the study categories.

Samples sizes ranged from one to 39,976 participants. Two studies that used *in-silico* and/or physical phantoms (Duarte Coello et al., 2023, 2024) did not involve the use of human data. The median sample size across all study types was 106 participants (IQR = 456.5). Application studies had the largest median sample size (161 participants) but also the greatest variance (IQR = 482.5). Sample sizes distribution by groups are shown in Table 4.

3.2.3. MRI sequences and field strengths

The included studies used a variety of MRI sequences, including T1w, T2w, proton density (PD), fluid-attenuated inversion recovery (FLAIR), and T2*w. Across all study types, the combined use of T1w and T2w MRI was the most frequently used (27.83% of studies), followed by the use of T2w imaging only (20.87% of all studies). One study used synthesised T2-type images for the development of a Digital Reference Object to evaluate PVS enhancement methods (Bernal et al., 2022). Although many studies of all types reported a combination of two or more sequence types, the majority used a single sequence, either T1w or T2w, to identify the PVS. Frequencies of individual and combined sequences are presented in Table 5.

The most commonly used MR field strengths were, in order, 3T, 1.5T, and 7T. Method development studies used 1.5T imaging more often than 3T or 7T (50.00%, 33.33%, 22.92%, respectively), with seven studies using MRI acquired at two different magnetic fields and one study (Dubost et al., 2019c) using MRI acquired at three different magnetic fields: 1T, 1.5T and 3T. In general, 17 studies used imaging from more than one field strength, typically a combination of 1.5T and 3T images or of 3T and 7T. Five 'method development' studies and one 'improvement' study (Paz et al., 2009) did not report the magnetic field of the MRI used. Application studies more commonly used 3T imaging (71.19%). One application study (Jokinen et al., 2020) used a small number of images from a 0.5T scanner. Frequencies of field strengths used in the included studies are presented in Table 6.

3.2.4. Voxel sizes and slice thickness

Voxel sizes varied amongst the samples. Fourteen out of the 48 methods proposed were 2D, owed to the anisotropy of the voxels in the images of the samples used. Consequently, application studies using those methods comprised images with largely anisotropic voxels (e.g., $0.4 \times 0.4 \times 5$ or 6 mm^3) (Tables 7 and 10). But not all 3D methods studies used images with isotropic voxels, as in many cases pipelines involved resampling and interpolation to convert the images to 1 mm isotropic (Table 7).

3.3. Method development studies

Summaries of all method development studies (N = 48) are presented in Table 7, ordered by year of publication. Twenty-seven were journal articles, 16 published in conference proceedings, and five in preprint repositories. It is worth noting that the four methods showcased by Sudre et al. (2022) submitted as part of the challenge organised by the publication authors were, at the time this review was conducted, in a preprint repository. Despite the semi-automatic method proposed by Smith et al. (2020) being also at a preprint repository, this method per-se has already been applied by a clinical study (Langan et al., 2022).

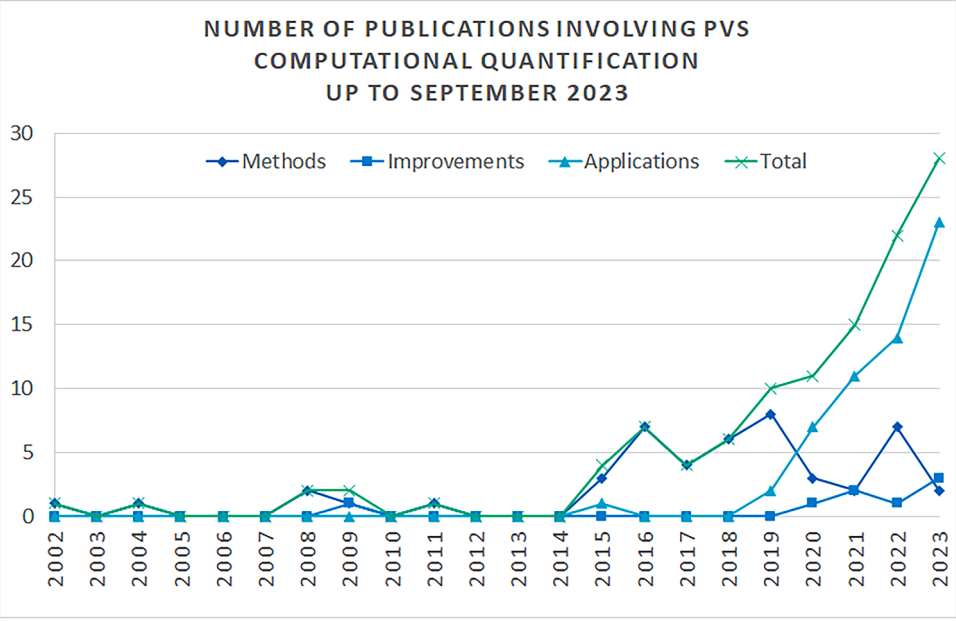

Fig. 2. Line graph showing number of computational PVS quantification papers published between 2002 and September 2023.

Table 2
Population types and clinically-relevant demographic groups.

	All		Method		Improvement		Application	
	N	%	N	%	N	%	N	%
Clinical	51	44.35	17	35.42	4	50.00	30	50.85
Non-clinical only	58	50.43	27	56.25	2	25.00	29	49.15
Unspecified	4	3.48	4	8.33	0	0	0	0
Cerebrovascular disease	18	15.65	6	12.50	3	37.50	9	15.25
Independently living older adults	31	26.96	12	25.00	1	12.50	18	30.51
Neurological / Neurodegenerative conditions	15	13.04	9	18.75	1	12.50	5	8.47
Twins / Familial	3	2.61	2	4.17	0	0	1	1.69
Occupation-related	2	1.74	0	0	0	0	2	3.39
Psychiatric condition	4	3.48	1	2.08	0	0	3	5.08
Communicable diseases	1	0.87	0	0	0	0	1	1.69
Genetic diseases	5	4.35	1	2.08	0	0	4	6.78

Legend: N: number of sources, %: Percentage with respect to the sources in each group (Note: in the Improvement category two studies did not use any human sample but phantoms and/or mathematical models)

Table 3
Population age groups.

	All		Method		Improvement		Application	
	N	%	N	%	N	%	N	%
Older adult (>60)	34	29.56	10	20.83	1	12.50	22	37.29
Middle adult (40-59)	3	2.61	0	0	0	0	3	5.08
Young adult (18-39)	10	8.70	7	14.58	0	0	3	5.08
Adult (18+)	23	20.00	10	20.83	3	37.50	10	16.95
Mid/Older adult (>40)	18	15.65	11	22.92	0	0	7	11.86
Young/Mid adult (18-59)	4	3.48	1	2.08	1	12.50	2	3.39
Child and adolescent (<18)	4	3.48	0	0	0	0	5	8.47
Child, adolescent, and young adult (<40)	1	0.87	0	0	0	0	1	1.69
Adult unspecified	3	2.61	0	0	1	12.50	2	3.39
Older adult unspecified	3	2.61	2	4.17	0	0	1	1.69
Young adult unspecified	1	0.87	1	2.08	0	0	0	0
Unspecified	10	8.70	6	12.50	2*	25.00	3	5.08
Total	115	100	48	100	8	100	59	100

Legend: N: number of sources, %: Percentage with respect to the number of sources in each group,
* : Not applicable, as no human data is used (studies on mathematical/phantom approaches only)

Table 4
Range and average sample sizes (N).

Study categories	Min	Max	Median	IQR [Q1 Q3]
All	0	39,976	106	[38 494.5]
Method development	1	2202	86	[19 272]
Improvement	0	747	50	[7.5 102]
Application	12	39,976	161	[57.5 540]

3.3.1. Computational methods

Seven of the 48 'method development' studies used a semi-automated approach, while the remaining 41 used a fully automated one. Broadly speaking, computational methods included filtering, machine learning, deep learning, combined approaches and intensity thresholding (i.e., as main technique) (Table 7). It is worth noting that most, if not all papers, involve thresholding. CNNs for example, often output a response map that is thresholded to get the binary masks. Also, filtering techniques generate a response that is thresholded to obtain the PVS proxies. The most frequent approach was the use of deep learning,

Table 5
MR sequence combinations.

	All		Method		Improvement		Application	
	N	%	N	%	N	%	N	%
T1w only	13	11.30	3	6.25	0	0	10	16.95
T2w only	24	20.87	17	35.42	5	62.50	2	3.39
PD only	3	2.61	2	4.17	1	12.50	0	0
T1w, T2w	32	27.83	13	27.08	0	0	19	32.20
T1w, T2*w	1	0.87	0	0	0	0	1	1.69
T1w, FLAIR	4	3.48	1	2.08	0	0	3	5.08
T1w, T2w, FLAIR	11	9.56	3	6.25	0	0	8	13.56
T1w, T2w, PD	1	0.87	1	2.08	0	0	0	0
T1w, T2w, Other	2	1.74	1	2.08	0	0	1	1.69
T2w, T2*w, FLAIR	1	0.87	1	2.08	0	0	0	0
T1w, T2w, T2*w, FLAIR	15	13.04	5	10.42	0	0	10	16.95
T1w, T2w, FLAIR, PD	7	6.09	1	2.08	1	12.50	5	8.47
T1w, T2w, FLAIR, Other	0**	0	0	0	0	0	0**	0
Total	115 *	100	48	100	8*	100	59	100

Legend: N: number of sources, %: Percentage with respect to the number of sources in each group
* : MRI sequences are not relevant for one of the Improvement papers.
** : An application study has T1w, T2w, FLAIR, and 3DFlow MRI, but only uses T1w and T2w for PVS segmentation.)

Table 6
MRI field strengths used.

	All		Method		Improvement		Application	
	N	%	N	%	N	%	N	%
1.5T	45	39.13	24	50.00	1	14.28	20	33.90
3T	61	53.04	16	33.33	3	42.86	42	71.19
7T	18	15.65	11	22.92	2	28.57	5	8.47
1T	1	0.87	1	2.08	0	0	0	0
0.5T	1	0.87	0	0	0	0	1	1.69
Unclear/ Unreported	6	5.22	5	10.42	1	14.28	0	0
More than one magnetic field	17	14.78	8	29.17	0	0	9	15.25

Legend: N: number of sources, %: Percentage with respect to the number of sources in each group

Table 7
Method development study summaries.

Study	Overview	Computational method	Reference standard	MRI info	Sample	Outcome features	Results
(Kruggel et al., 2002)	PVS segmented using Markov models. 1. Run Reversible Jump Markov Chain Monte Carlo algorithm on data. 2. Non-linear registration to template space	Stochastic geometry. Fully automated, 3D	None described	T1w 0.86 × 1.5 × 0.86 mm^3 vox size, (resampled to $1mm^3$), T2w. 3T	Older adults. N = 37	Total count, volume and location (figure showing spatial occurrence)	None described. Figure of cumulative spatial distribution of PVS segmented in the 37 T1w images shown.
(Descombes et al., 2004)	Automatic method to detect and segment PVS by modelling the PVS geometry and spatial distribution with a Marked Point Process in T1W images, optimised with a Reversible Jump Markov Chain Monte Carlo algorithm and simulated annealing.	Stochastic geometry. Fully automated, 3D	Visual count	T1w 0.9 × 0.9 × 1.5 mm^3 vox size (resampled to $1mm^3$). 1.5T	Older adults. N =37	Total count and location (figure showing spatial occurrence)	Correlation between visual scores and computational counts 0.77, ICC of counts between two experts 0.97, and between one expert and the automatic count 0.87. Type I error (false positives) 13% and type II error (false negatives) 2.7%
(Uchiyama et al., 2008)	Lesion segmentation by top-hat transform and thresholding. Neural network to distinguish lacunar infarcts from PVS using 6 features.	Thresholding and neural network. Fully automated, 2D	Visual inspection	T1w used during post-processing to separate lacunar infarcts from PVS, T2w 0.47 × 0.47 × 5.00 mm^3 vox size. Slice gap: 2mm, 1.5T	Unspecified. N = 109	Location, PVS size, PVS irregularity (1-C/L, C=length of circle of the same area as the segmented region, L=boundary length of segmented region) T1w and T2w signal intensity difference between lesion and surroundings.	AUC=0.945 to classify lacunar infarcts from PVS.
(Wuerfel et al., 2008)	Semi-automated PVS quantification used to explore PVS as an MRI marker of inflammatory activity in the brain.	Thresholding. Semi-automated, 3D	Visual inspection	T1w ($1mm^3$), T2w (3mm thick), FLAIR (3mm thick)., 1.5T	MS., N = 75	Total volume (raw and fractional), Count	Semi-auto PVS quantification vs. manual PVS quantification ICC = 1 (N = 4)
(Uchiyama et al., 2009)	Lesion segmentation by top-hat transform and thresholding. Neural network to distinguish lacunar infarcts from PVS using 6 feature. (As in (Uchiyama et al., 2008)).	Thresholding and neural network. Fully automated, 2D	Visual inspection	T1w used during post-processing to separate lacunar infarcts from PVS, T2w 0.47 × 0.47 × 5.00 mm^3 vox size., Slice gap: 2mm, MRA., 3T, 1.5T	Unspecified. N =109	Location, PVS size, PVS irregularity (1-C/L, C=length of circle of the same area as the segmented region, L=boundary length of segmented region), T1w and T2w signal intensity difference between lesion and surroundings.	AUC=0.945 to classify lacunar infarcts from PVS, sensitivity=93.3% and specificity=75% for detection of lacunar infarcts.
(Ramirez et al., 2011)	Segmentation tools for subcortical hyperintensities and intracranial tissue.	Thresholding. Semi-automated, 3D	Manual segmentation	T1w 0.859 × 0.859 × (1.2-1.4) mm^3 T2w 0.781 × 0.781 × 3 mm^3, PD 0.781 × 0.781 × 3 mm^3 vox size (all co-registered to T1w). 1.5T	Dementia. , N = 20	Total volume	Global ICC 0.99 and local ICC 0.97.
(Cai et al., 2015)	PVS segmentation using image gradients. Step 1. Compute image gradients using MATLAB. Step 2. Segment white matter region. Step 3. Interpolate 0.42 ×	Thresholding. Fully automated, 2D	None described.	T2w 0.42 × 0.42 × 1.00 mm^3 vox size., 7T	Alzheimer's disease (AD) N = 5 and controls N = 3 (Total N=8)	Location (figure showing spatial occurrence), Total volume (fractional)	Segmentation performance described qualitatively, with illustration. No performance metrics provided.

(*continued on next page*)

Table 7 (*continued*)

Study	Overview	Computational method	Reference standard	MRI info	Sample	Outcome features	Results
	0.42 × 1 mm scans to 0.40 × 0.40 × 0.40 mm. Step 4. Compute maximum intensity projection and colour-code it using cyan-hot colour map. Step 5. Edge-detection and component connectivity analysis.						
(Pereira et al., 2015)	Tool that integrates pre-processing, tissue and ROI segmentation, detection, and visualisation of PVS, using a modification of the method described in (Descombes et al., 2004), allowing the user to check and edit the response.	Stochastic geometry. Semi-automated, 3D	Visual inspection	T1w 1 mm^3 vox size., 1.5T	Mild stroke. , N = 9	PVS segmentation and visualisation	Study describes an automated tool with graphic interface that allows user interaction to confirm automatic responses. Performance metrics not provided.
(Ramirez et al., 2015)	PVS segmentation using a modified version of Lesion explorer. Step 1. Skull stripping using Brain Sizer. Step 2. Brain parcellation using SABRE. Step 3. Fuzzy c-means on T1w to segment brain tissues. Step 4. Subcortical hyperintense regions are found using an intensity-based rejection strategy. Step 5. Fuzzy c-means to segment brain tissues. Step 6. Reclassification of small subcortical hyperintense regions (here PVS) based on T1w and T2w intensity, as well as WMH/lacunes based on T1w, T2w, and PD signal. Step 7. Manual edit of PVS masks.	Thresholding. Semi-automated, 3D	Visual rating scores (Patankar and MacLullich-Potter-Wardlaw scales)	T1w 0.859 × 0.859 × (1.2-1.4) mm^3, T2w 0.781 × 0.781 × 3 mm^3, PD 0.781 × 0.781 × 3 mm^3 (all co-registered to T1w). 1.5T	Dementia. N = 297	Total volume	Correlation: Patankar - CSO: 0.84; Patankar - BG: 0.75; MacLullich-Potter-Wardlaw - CSO: 0.82; MacLullich-Potter-Wardlaw - BG: 0.26
(Ballerini et al., 2016)	Proposes using the ordered logit model to estimate the parameters of the Frangi filter to obtain the maximum likelihood of a vessel-like structure to be a PVS in the CSO by estimating the count of PVS that most probably fall in the visual score given by the neuroradiologist in this brain region.	Frangi filtering and thresholding. Fully automated, 3D	Visual rating scores (MacLullich-Potter-Wardlaw scale)	T2w 1 × 1 × 2 mm^3(resampled to 1mm^3), 1.5T	Older adults (age ~72.6 years). N = 60	Total volume, total counts (in the CSO)	Spearman rho correlation between PVS volume and visual scores 0.75 and between computational counts and visual scores 0.69.
(González-Castro et al., 2016b)	BG PVS scores using bag of visual words (BoW): SIFT and textons; and Support	Machine learning classifier (SVM). Fully automated, 2D	Visual rating scores (MacLullich-	T2w 0.94 × 0.94 × 6.5 mm^3, 5 mm thick, 1.5 mm inter-slice gap, 1.5T	Mild stroke., N = 264	Dichotomised PVS score in BG	Accuracy: SIFT: 82.34%, textons: 79.61%

(*continued on next page*)

Table 7 (*continued*)

Study	Overview	Computational method	Reference standard	MRI info	Sample	Outcome features	Results
	Vector Machine (SVM)		Potter-Wardlaw scale)				
(González-Castro et al., 2016a)	BG PVS rating (0: scores of 0-1; 1: scores of 2-4) using SVM and texture features. Step 1. ICV and CSF segmentation using optiBET and FAST. Step 2. Subcortical structure segmentation using FSL tools and the multispectral colour fusion technique. Step 3. Manual selection of slices with highest counts. Step 4. Manual delineation of the basal ganglia. Step 5. Contrast enhancement using CLAHE. Step 6. Thresholding 0.43 times the maximum intensity level. Step 7. Blob counting. Step 8. Texture extraction (discrete wavelet transform, wavelet statistical features, Haralick features, local binary patterns). Step 9. SVM classifies based on extracted features	Machine learning classifier (SVM). Fully automated, but manual intervention to select and delineate the ROI, 2D	Visual rating scores (MacLullich-Potter-Wardlaw scale)	T2w 0.94 × 0.94 × 6.5 mm^3, 5 mm thick, 1.5 mm inter-slice gap, 1.5T	Mild stroke. , N = 264	Dichotomised PVS score in BG	Accuracy = 80.03; True Negative Rate = 79.36; True Positive Rate = 80.67
(Park et al., 2016)	Random forest with Haar features. Step 1: correct intensity inhomogeneity, skull strip, segment tissues, modality co-registration. Step 2: extract Haar features. Step 3: fit features into random forest. Step 4: repeat steps 2 and 3 five times using auto-context to refine segmentation results (Inputs – first classifier: Haar features; second classifier: Haar features + prediction map first classifier; and so on).	Machine learning classifier (random forest). Fully automated, 3D	Manual segmentation	T1W MPRAGE 0.65 × 0.65 × 0.65 mm3 voxel size. T2W 3D variable flip angle turbo SE 0.4 × 0.4 × 0.4 mm3 or 0.5 × 0.5 × 0.5 mm3 voxel sizes, 7T Reconstructed images had the same voxel sizes as acquired images. No interpolation applied during image reconstruction	Healthy adults. , N = 17	PVS segmentation, PVS volume, length, and thickness (total and individual)	Manual x Automated Average measurements for best configuration performance: DSC = 0.73 (SD 0.05), sensitivity = 0.69 (SD 0.09), PPV = 0.80 (SD 0.07)
(Wang et al., 2016b)	Semi-automatic PVS segmentation: Slice selection in BG, Ovoid region delineation in BG, linear intensity adjustment, thresholding.	Thresholding. Semi-automated, 2D	Visual rating scores (MacLullich-Potter-Wardlaw scale)	T1w, T2w (Stroke sample: 0.47 × 0.47 × 6 mm^3, elderly sample: 1 × 1 × 2 mm^3) T2*w, FLAIR., 1.5T	Mild stroke, N = 110 (testing sample), Community-dwelling older N=16, (method development)	Total and individual PVS count and volume in BG	BGPVS volume increased with BGPVS count (67.27, p <0.001). BGPVS computational count was positively associated with WMH visual rating (PVH: 2.20, DWMH: 1.92, p<0.001), WMH volume (0.065, p<0.001), and whole brain atrophy visual rating (1.01, p<0.001).

(*continued on next page*)

Table 7 (*continued*)

Study	Overview	Computational method	Reference standard	MRI info	Sample	Outcome features	Results
(Zhang et al., 2016)	Random forest with features from steerable, optimally oriented flux, and Frangi filters. Step 1: skull strip, segment tissues, modality co-registration. Step 2: extract features. Step 3: fit features into random forest.	Frangi filtering and machine learning. Fully automated, 3D	Manual segmentation	T1w: 0.65 × 0.65 × 0.65 mm^3, T2w: 0.5 × 0.5 × 0.5 mm^3 (or 0.4 × 0.4 × 0.4 mm^3), 7T	Unspecified. N =10	PVS segmentation (Vascular features are extracted to train the Random Forest)	Manual x Automated DSC = 0.6 - 0.66
(Zong et al., 2016)	Two aims. 1. Develop a sequence for better visualising PVS at 7T. 2. Quantify PVS. Steps for quantification: Step 1. Intensity inhomogeneity correction using N3. Step 2. Skull stripping using BET. Step 3. Tissue segmentation with FAST. Step 4. Modality co-registration using FLIRT. Step 5. Frangi vesselness filtering. Step 5. Binarisation. Step 6. Connected component analysis to remove small (<0.8mm) or (>30 mm) PVS. Step 7. Manual correction. Step 8. Morphology analysis to extract PVS diameter, length, and volume.	Frangi filtering and thresholding. Fully automated, 3D	None described	T1w: 0.41 × 0.41 × 0.4 mm^3, T2w: 0.65 × 0.65 × 0.65 mm^3. 7T	Healthy adults., N = 6	Length, volume, and diameter distributions of PVS	No performance metrics reported. Qualitatively, sequence optimisation leads to higher contrast and "much larger numbers of PVSs in young healthy subjects (age 21–37 years) than previously reported"
(Dubost et al., 2017)	GP- Unet for lesion detection. Step 1: Registration to MNI space. Step 2: ROI computation using FreeSurfer and ROI smoothing using gaussian kernel. Step 3: GP-Unet for lesion segmentation	Deep learning (CNN). Fully automated, 3D	Visual count	PD: 0.49 × 0.49 × 0.8 mm^3., 1.5T	Rotterdam Scan Study., N = 1642	Lesion heatmaps	True Positive Rate = 62.0, number of false positives (Fpav) = 1.5 and False Discovery Rate = 31.4
(González-Castro et al., 2017)	Automated classification of BG PVS burden. Descriptors: wavelet transform-based, local binary patterns, and Bag of Words using scale-invariant feature transform (SIFT) descriptors, Classifier: SVM with radial basis function kernel.	Machine learning classifier (SVM). Fully automated, 2D	Visual rating scores (MacLullich-Potter-Wardlaw)	T2w: 0.469 × 0.469 × 6 mm^3, slices 5 mm thick, 1 mm gap, 1.5T	Mild Stroke., N = 264	Dichotomised PVS scores in BG	Cross-correlation K=0.62-0.67, AUC = 0.90-0.93.
(Hou et al., 2017)	PVS segmentation. Step 1: Image enhancement (Haar transform). Step 2: Image denoising (BM4D). Step 3: PVS segmentation (Vesselness filter and Random forest classifier).	Frangi filtering and machine learning (random forest). Fully automated, 3D	Manual segmentation	T2w: 0.4 × 0.4 × 0.4 mm^3 or 0.5 × 0.5 × 0.5 mm^3., 7T	Healthy adults. , N = 17	PVS segmentation	DSC 0.75, PPV 0.73 and SN 0.77
(Zhang et al., 2017)	Structured random forest with features	Frangi filtering and machine	Manual segmentation	T1W: 0.65 × 0.65 × 0.65 mm^3, T2W: 0.5	Unspecified. N = 19	PVS segmentation	Manual x Automated DSC = 0.66 (SD 0.03),

(*continued on next page*)

Table 7 (*continued*)

Study	Overview	Computational method	Reference standard	MRI info	Sample	Outcome features	Results
	from steerable, optimally oriented flux, and Frangi filters. Step 1: skull strip, segment tissues, modality co-registration. Step 2: extract features. Step 3: fit features into random forest	learning (random forest). Fully automated, 3D		× 0.5 × 0.5 mm3 (or 0.4 × 0.4 × 0.4 mm^3)., 7T			SN = 0.65 (SD 0.04), PPV = 0.68 (SD 0.04)
(Ballerini et al., 2018)	PVS segmentation using the Frangi filter. Step 1. Segment CSO region of interest using Lesion Explorer. Step 2. Run Frangi filter. Step 3. Binarisation. All parameters were optimised against visual scores via ordered logistic modelling.	Frangi filtering and thresholding. Fully automated, 3D	Visual rating scores (MacLullich-Potter-Wardlaw scale)	T1w SDS: 0.86 × 0.86 × 1.4 mm^3, MSS: 1.02 × 0.9 × 1.02 mm^3 voxel size, T2w SDS: 0.78 × 0.78 × 3 mm^3, MSS: 0.47 × 0.47 × 6 mm^3 voxel size, 1.5T	Dementia from Sunnybrook Dementia Study (SDS), Mild stroke (MSS)., N = 365	PVS segmentation in CSO, PVS scores in CSO	SDS: PVS count in slice with max count vs visual score - ρ = 0.74; total PVS count vs visual score - ρ = 0.67; total PVS volume vs visual score - ρ = 0.53. MSS: PVS total count and volume correlates with visual rating scores (Spearman's ρ = 0.47, $p < 0.001$ and ρ = 0.57, $p < 0.001$, respectively)
(Boespflug et al., 2018)	PVS segmentation using 4 types of images. Step 1: ROI extraction. Step 2: Intensity normalisation. Step 3: Cluster isolation. Step 4: Morphological constraint algorithm to fit lines.	Morphology analysis and thresholding. Fully automated, 3D	Visual count	T1w: 1 mm isotropic voxel size, T2w and PD: 0.938 × 0.938 × 2 mm^3, FLAIR 0.938 × 0.938 × 3 mm^3, 3T	Older adults. , N =14	Total PVS count and volume, and morphology (linearity, volume, width) for each PVS	Correlations with visual scores (MacLullich-Potter-Wardlaw scale): r=0.58-0.69
(Jung et al., 2018)	PVS enhancement. Densely connected deep CNN.	Deep learning (CNN). Fully automated, 3D	Heuristically enhanced PVS	T2w: 3D, algo. Used 60 × 60 × 60 voxel patches, 7T	Healthy adults. , N = 17	Enhanced T2w image	PSNR 38.739 dB and SSIM 0.976
(Lian et al., 2018)	PVS segmentation. Step 1: Image enhancement (Haar transform). Step 2: Image denoising (BM4D). Step 3: Fully Convolutional Network.	Deep learning (CNN). Fully automated, 3D	Manual segmentation	T2w 0.5 × 0.5 × 0.5 mm^3 or 0.4 × 0.4 × 0.4 mm^3., 7T	Healthy adults. , N = 20	PVS segmentation	DSC 0.77, PPV 0.83 and sensitivity 0.74
(Martinez-Ramirez et al., 2018)	PVS in sporadic and hereditary cerebral amyloid angiopathy. PVS segmentation in 1 slice using semi-manual technique. Step 1: Selection of the slice. Step 2: Intensity adjustment. Step 3: Thresholding. Step 4: Manually create a mask containing the PVS inside the White matter. Step 5: Subtract both masks. Step 6: Manual correction.	Thresholding. Semi-automated, 2D	Visual rating scores (MacLullich-Potter-Wardlaw scale)	1.5T scanner: T1w 1.5 × 1.5 × 1.5 mm^3, T2w 0.859 × 0.859 × 4 mm^3, 3T scanner: T1w FOV 224mm x 177mm x 168mm, does not provide matrix size, T2w 0.5 × 0.5 × 3.6 mm^3, FLAIR 1.125 × 0.8025 × 10 mm^3.	Hereditary CAA carriers., N = 54	PVS total volume in BG and CSO	ICC for CSO-PVS relative volume measurement between two expert readers = 0.93
(Niazi et al., 2018)	PVS for early diagnosis of Mild Cognitive Impairment. Step 1. Heuristically compute WM and Basal ganglia. Step 2: Compute image gradient. Step 3: Threshold gradient.	Thresholding. Fully automated, 2D	Visual inspection	T2w: 0.4 × 0.4 × 2 mm^3 voxel size., 3T	MCI., N = 29	PVS segmentation in WM and BG, total volume and count (density) in WM and BG	Automated PVS vs. visual counting = 0.77% false positive pixels Automated PVS vs. visual counting = 19.39% false negative pixels

(*continued on next page*)

Table 7 (*continued*)

Study	Overview	Computational method	Reference standard	MRI info	Sample	Outcome features	Results
(Dubost, Adams, et al., 2019)	3D regression convolutional neural network (CNN) to automatically score BG PVS, where the score corresponds with the count in one slice as per Adams et al., 2015.	Deep learning (CNN). Fully automated, 3D	Visual counting	PD: 0.49mm x 0.49mm x 0.8mm., 1.5T	Rotterdam Scan Study., N = 2063	PVS scores and saliency maps (in BG only)	Best results: ICC=0.803, MSE=4.85; ICC=0.787, MSE=4.65. In Reproducibility set (46 scans), best model: ICC=0.93±0.02
(Dubos et al., 2019b)	PVS rating using deep CNN in midbrain, hippocampus, basal ganglia and centrum semiovale. Step 1: Bias field correction. Step 2: Freesurfer. Step 3: ROI cleaning. Step 4: Deep CNN per ROI. - Extends (Dubost, Adams, et al., 2019) to other three brain regions (one CNN per region), uses different CNN architecture (lighter models, introduces skip connections between blocks, and uses global pooling instead of two fully connected layers of 2000 neurons), and provides a more elaborate evaluation.	Deep learning (CNN): small ResNet adapted for regression in a 3D image. Fully automated, 3D	Visual rating scores (UNIVRSE consortium)	T2w: 0.49mm x 0.49mm x 0.8mm., 1.5T	Rotterdam Scan Study., N = 1485	PVS scores in 4 regions	Interclass correlation coefficients between 0.75 and 0.88
(Dubost et al., 2019c)	PVS quantification by 2 methods: (1) a neural network with 4 convolutional layers and a max-pooling layer which output the number of PVS (CNN) (2) a GP-Unet to enable weakly supervised detection of PVS.	Deep learning (CNN). Fully automated, 3D	Visual rating scores	T1w, T2w: 0.5mm x 0.5mm x 0.8mm., 1.5T, 3T, 1T	Rotterdam Scan Study, Magdeburg PACS., N = 1676	PVS scores and attention maps	Pearson correlation: CNN: 0.52 (CSO), 0.25 (BG), 0.33 (hippocampi); GP-Unet: 0.78 (CSO), 0.31 (BG), 0.51 (hippocampi). Mean absolute errors: CNN: 6.39 (CSO), 5.49 (BG), 3.0 (hippocampi); GP-Unet: 5.58 (CSO), 5.67 (BG), 2.58 (hippocampi). Note: values presented in text and in tables differ.
(Jung et al., 2019)	60 × 60 × 60 voxel patches, 3D Dense neural network (CNN) to enhance the quality of the PVS	Filtering and deep learning (CNN). Fully automated, 3D	Heuristically enhanced PVS	T2w: 0.5mm x 0.5mm x 2mm., 7T	Healthy adults., N = 17	Enhanced image	PSNR 47.98dB and SSIM 0.975
(Schwartz et al., 2019)	PVS segmented by stepwise local homogeneity search of white matter-masked T1w, constrained by FLAIR hyperintensity, and further constrained by width, volume, and linearity measurements.	Morphological detection. Fully automated, 3D	Visual inspection	3D T1w 1 mm isotropic, 2D FLAIR 0.966mm x 0.968mm x 2mm., 3T, 1.5T	Alzheimer's disease, Older adults., N = 44	PVS segmentation	Visual vs automatic correlation r=.72 p<0.0001. Repeated measures correlation: single slice r=.87, p<0.0001, whole brain r=.77, p=.001
(Sepehrband et al., 2019)	T1w - T2w PVS enhancement. Step 1: Bias filter correction. Step 2: Co-registration. Step	Frangi filtering and thresholding. Fully automated, 3D	Visual rating scores (MacLullich-Potter-Wardlaw scale)	3D T1w 0.7 mm isotropic, 3D T2w 0.7mm isotropic ., 7T	Human Connectome Project., N = 900	PVS segmentation, Total PVS volumes and counts in BG and CSO	Lin's concordance coefficient = 0.81 and Pearson's correlation coefficient = 0.61

(*continued on next page*)

Table 7 (*continued*)

Study	Overview	Computational method	Reference standard	MRI info	Sample	Outcome features	Results
	3: Non-local filtering to remove noise. Step 4: T1w/T2w image. Step 5: Frangi filter.						
(Sudre et al., 2019)	3D region-based deep learning model (HighResNet convolutional neural network architecture implemented in niftynet and which operates in ROIs) to detect and characterise lacunes and/from PVS (both considered extremely small objects, abbreviated as ESO). It improves 2D Mask-R-CNN models (not previously used for this purpose), and outputs: a) a probability "score" map and b) boxes encircling the PVS or lacunes. It does not segment the PVS or lacunes.	Deep learning (CNN). Fully automated, 3D	Probabilistic boxes for manually segmented PVS and lacunes, from two observers.	T1w, T2w, FLAIR, all 3D 1mm, Isotropic., 7T	Older adults., N = 16	Probabilistic boxes identifying presence of PVS and lacunes	Sensitivity of 72.7%, median overlap positive agreement of 59% for boxes/voxels agreed by all raters, and 30% when at least one rater disagreed.
(van Wijnen et al., 2019)	PVS detected by Fully Convolutional Neural Network using Distance Maps: Euclidean (EDM), geodesic (GDM), intensity (IDM) distance maps	Deep learning (CNN). Fully automated, 3D	Manual annotation	T2w 0.49 × 0.49 × 0.8 mm^3., 1.5T	Rotterdam Scan Study., N = 2202	PVS detection	On test set: EDM: FAUC=45.761, Sensitivity= 53.63; DGM: FAUC=50.757, Sensitivity= 55.26; IDM: FAUC=53.078, Sensitivity=55.35
(Choi et al., 2020)	PVS segmentation. Step 1: ROI segmentation using FreeSurfer. Step 2: Frangi Filter. Step 3: CNN for removing false positives.	Frangi filtering and deep learning (CNN). Fully automated, 3D	Manual segmentation	3D T1w, 3D T2w both 0.7 mm isotropic., 3T	Human Connectome Project., N = 1210	PVS segmentation and regional (BG and WM) volumes	ICC 0.98 (validation set N = 10).
(Dubost et al., 2020)	PVS counts are predicted using a weakly supervised detection method using neural networks that compute attention maps (GP-UNet). The approach is weakly supervised because only image-level counts are entered for training. Step 1. Put image through network. Step 2. Retrieve activation map but ignore those regions where attention maps contained negative values. Step 3. Non-maximal suppression. Step 4. Candidates with the highest responses are deemed as most likely candidates.	Deep learning (CNN). Fully automated, 3D	Manual annotation	T2w 0.49 × 0.49 × 0.8 mm^3., 1.5T	Rotterdam Scan Study., N = 2202	PVS detection, segmentation, volume (and count) in 4 regions: hippocampi, midbrain, BG and CSO	Manual x Automated: FAUCs = 72.0 +- 13.3; Sensitivity = 62.1+-8.7; Average number of false positives = 2.33+-1.71, Average number of false negatives = 2.44+-2.01
(Smith et al., 2020)	Semi-automated MATLAB tool (GUI) for PVS	Frangi filtering and thresholding.	Manual segmentation	T2w (any resolution can be accepted), 7T	MS., N = 1	PVS segmentation, visualisation and editing	83% of PVS match with the ground truth and 94% of the ground

(*continued on next page*)

Table 7 (*continued*)

Study	Overview	Computational method	Reference standard	MRI info	Sample	Outcome features	Results
	segmentation, editing, and visualisation. Needs ROI as input and uses Frangi filter.	Semi- automated, 2D and 3D					truth match with the segmentation.
(Boutinaud et al., 2021)	3D deep learning method that uses an auto-encoder and a U-Net to segment PVS in deep white matter (DWM) and BG from T1W images.	Deep learning (CNN). Fully automated, 3D	Manual segmentation	T1w 1 mm isotropic., 3T	Healthy adults., N = 1832	PVS segmentation and regional volumes in BG and deep WM	In 10 people's data, DSC=0.51 in DWM and 0.66 in BG; and 0.64 in DWM (0.71 in BG) for PVS cluster detection (volume threshold of 0.5 within a range of 0 to 1). Dice values above 0.90 could be reached for detecting PVSs larger than 10 mm3 and 0.95 for PVS larger than 15 mm3. When applied to a sample of n=1782, agreement with a semi-quantitative visual rating done by an independent expert rater for DWM R^2(thr0.1) = 0.38, R^2(thr0.5) = 0.45, R^2(thr0.9) = 0.47, p < 0.001, and BG R^2(thr0.1) = 0.02, R^2(thr0.5) = 0.05, R^2(thr0.9) = 0.04, p < 0.001.
(Yang et al., 2021)	PVS rating using CNN-based deep learning model using 3 slices of the T2w (basal ganglia only). Step 1: Preprocessing (ROI extraction and image enhancement). Step 2: CNN. Output: PVS rating.	Deep learning (CNN). Fully automated, 2D	Visual rating scores	T1W 1 mm isotropic, T2w 0.573 × 0.573 × 5 mm^3., 3T	Alzheimer's Disease. , N = 96	BG PVS scores	Correlation 0.9169 with p=0.0001 for images, and 0.9335 with p=0.0001 for subjects.
(Ranti et al., 2022)	PVS segmentation using the Frangi filter in a MATLAB GUI. Step 1. WM segmentation using FreeSurfer. Step 2. Fill holes in WM mask. Step 3. Frangi filtering. Step 4. Boundary voxel removal. Step 5. Intensity and Frangi based binarisation. Step 6. Manual correction.	Frangi filtering and thresholding. Semi-automated, 2D or 3D.	Manual segmentation	T1w, T2w 0.4 × 0.4 mm in-plane resol. interpolated to 0.2 × 0.2 mm, thickness=2 mm, and 0.6 mm inter-slice gap., 7T	MDD N=21 and healthy controls N=27. , Total N = 48	PVS total volume, count, density, PVS individual length and width (median values given)	Manual x Automated: Sensitivity = 82.9, Specificity = 91.9; Semi-automated x Semi-automated (two raters): Dice = .9914, inter-rater reliability = 97.8.
(Spijkerman et al., 2022)	Automated detection and quantification of PVS. Binary PVS probability maps created using kNN classifier using T1w, T2w and vesselness values.	Machine learning classifier (kNN). Fully automated, 3D	Manual annotation in a single slice CSO right hemisphere	T1w 1mm^3, T2w 0.7 mm-isotropic., 7T	Healthy adults., N = 50	Total count, density, and individual PVS lengths and tortuosity	Bland-Altman: smaller PVS count identified by automated method compared to human. ICC (absolute/consistency) = 0.64/0.75. DSC = 0.61 between automated and manually labelled.
(Sudre et al., 2022), 'BigrBrain'	U-Net, Dice loss, 225 × 225 patches size.	Deep learning (CNN). Fully automated, 2D	Manual annotation in selected 2D slices	T1w, T2w, FLAIR., SABRE sample: 1.09 × 1.09 × 1.0 mm^3, RSS sample: 0.49 × 0.49 × 0.8 mm^3, 3T, 1.5T	Rotterdam Scan Study, SABRE., N = 106	PVS detection and segmentation, Total PVS volume and count	F1=35.81, AED=14.50, Mean Dice=61.09, AVD=45.30

(*continued on next page*)

Table 7 (*continued*)

Study	Overview	Computational method	Reference standard	MRI info	Sample	Outcome features	Results
(Sudre et al., 2022), 'Neurophet'	Mask RCNN, Losses: BCE, Focal, & MAE.	Deep learning (CNN). Fully automated, 2.5D	Manual annotation in selected 2D slices, 2.5D	T1w, T2w, FLAIR., SABRE sample: 1.09 × 1.09 × 1.0 mm^3, RSS sample: 0.49 × 0.49 × 0.8 mm^3, 3T, 1.5T	Rotterdam Scan Study, SABRE., N = 106	PVS detection and segmentation, Total PVS volume and count	F1=0, AED=29, Mean Dice=28.23, AVD=390.15
(Sudre et al., 2022) 'TeamTea'	nnU-Net, Dice loss, 256 × 224 patches size.	Deep learning (CNN). Fully automated, 2D	Manual annotation in selected 2D slices	T1w, T2w, FLAIR., SABRE sample: 1.09 × 1.09 × 1.0 mm^3, RSS sample: 0.49 × 0.49 × 0.8 mm^3 3T, 1.5T	Rotterdam Scan Study, SABRE., N = 106	PVS detection and segmentation, Total PVS volume and count	F1=17.12, AED=41, Mean Dice=55.07, AVD=106.05
(Sudre et al., 2022) 'TheGPU'	Random forest (minimal detail reported).	Machine learning classifier (random forest). Fully automated, 2D	Manual annotation in selected 2D slices	T1w, T2w, FLAIR. SABRE sample: 1.09 × 1.09 × 1.0 mm^3, RSS sample: 0.49 × 0.49 × 0.8 mm^3, 3T, 1.5T	Rotterdam Scan Study, SABRE., N = 106	PVS detection and segmentation, Total PVS volume and count	F1=38.92, AED=16, Mean Dice=72.38, AVD=45.20
(Williamson et al., 2022)	PVS graded by ResNet-152. Each image (512 × 512 × 16) input to a 3D convolutional layer (7 × 7 × 7, 64 filters) with ReLu activation and batch normalization, followed by a series of 50 residual units, each with 3 convolutional layers.	Deep learning (CNN). Fully automated, 3D	Visual rating scores (MacLullich-Potter-Wardlaw scale)	T2w (5 sites, 24-36 slices, median=32)., 7T	Stroke. , N = 262	PVS scores	Accuracy/AUC of 0.802/0.834 on the training set, 0.768/0.847 on the validation set, and 0.897(95% CI = [0.758, 0.971])/0.879 on the test set. On the held-out test set, specificity=0.96, sensitivity=0.80, and F1=0.86
(Lan et al., 2023)	Weakly supervised conditional random field recurrent neuronal network (CRF-RNN). Combines Frangi filter with U-Net using conditional random field theory, optimised using weighted cross entropy loss function training patch selection.	Deep learning (CNN) and Frangi filtering. Fully automated, 3D	Scan-rescan interclass correlation 0.97, 33% manual corrected by 2 raters	T1w, T2w from two protocols: 0.7 mm isotropic and 0.8 mm isotropic, 3T	Healthy female volunteers from the Human Connectome Project (N=400)	PVS segmentation, saliency map	Frangi FP = 0.0067 ± 0.0063; WPSS FP = 0.0093 ± 0.0069; U-Net FP = 0.0146 ± 0.0096. WPSS and U-Net trained using QC data: Frangi FP = 0.0068 ± 0.0060, WPSS FP = 0.0020 ± 0.0026, U-Net FP = 0.0033 ± 0.0035.
(Rashid et al., 2023)	Implements a lightweight U-Net adapted for PVS detection and investigates different combinations of information from SWI, FLAIR, T1-weighted (T1w), and T2-weighted (T2w) MRI sequences to inform best sequence combination for the task using deep learning in a multi-ethnic cohort.	Deep learning (CNN). Fully automated, 2D	Manual segmentations in 21 subjects	FLAIR, T1w, T2w 1 mm isotropic, SWI 1 × 1 × 1,5 mm^3, 3T	21 MESA participants with age range from 64 to 94 years	PVS segmentation	T2w MRI is the most important for accurate PVS detection, and the incorporation of SWI, FLAIR and T1w MRI in the deep neural network had minor improvements in accuracy and resulted in the highest sensitivity and precision (sensitivity = 0.82, precision = 0.83).

Note: The MRI sequence(s) underlined is(are) the one(s) used specifically to generate the PVS assessments. The non-underlined MRI sequences in each case are used in pre-/post-processing. Legend: PVS: Perivascular Spaces, AUC: Area Under the (ROC) Curve, FAUC: F stat (ratio of two variances) of the AUC from two measurements (e.g. manual vs. automatic) CI: Confidence Interval, CNN: Convolutional Neural Networks, GUI: Graphic Unit Interface, AED: Absolute Error Difference, ICC: Intra-class Correlation Coefficient, AVD: Absolute Volume Difference, DSC: Dice Similarity Coefficient, BG: basal ganglia, CSO: centrum semiovale, FOV: Field Of View, CLAHE: Contrast Limited Adaptive Histogram Equalization, FP: False Positives, SWI: Susceptibility Weighted Images, MDD: Major Depressive Disorder, WM: White Matter, GM: Grey Matter, DWM: Deep White Matter, PSNR: Peak Signal-to-Noise Ratio, SSIM: Structural Similarity Index Metric, PPV: Positive Predictive Value, SABRE: Southall And BRent Revisited study, MESA: Multi-Ethnic Study of Atherosclerosis, WPSS: Weakly Supervised Perivascular Spaces Segmentation, PVH: periventricular hyperintensities, DWMH: deep white matter hyperintensities, MSE: Mean Squared Error, MAE: Mean Absolute Error, F1: accuracy metric that combines the precision and recall scores of a model by computing how many times a model made a correct prediction across the entire dataset, QC: Quality Control, TPR: True Positive Rate, FDR: False Discovery Rate, CNN: Convolutional Neural Network, SIFT: Scale Invariant Feature Transform, SD: Standard Deviation.

proposed in 16 studies (33.33%). Frequencies of all types of approaches proposed are presented in Table 8.

From all the sources in this category, only nine provide their code in a public repository, 28 do not provide the code, and one provides via to request the code (Supplementary Table 2). The rest use publicly available resources like the Frangi vesselness filter (Frangi et al., 1998) implementation by Dirk-Jan Kroon (2009) hosted by MATLAB Central File Exchange (https://www.mathworks.com/matlabcentral/fileexchange/24409-hessian-based-frangi-vesselness-filter), or the 3D multi-radii optimally oriented flux responses for curvilinear structure analysis implementation by Max W.K. Law (2013) also hosted by MATLAB Central File Exchange (https://www.mathworks.com/matlabcentral/fileexchange/41612-optimally-oriented-flux-oof-for-3d-curvilinear-structure). The FMRIB Software Library (FSL, https://fsl.fmrib.ox.ac.uk/fsl/fslwiki) is the preferred software used for sequence co-registration, occasionally for brain extraction, and in two sources (González-Castro et al., 2016b, 2017) it is also used for generating priors of the basal ganglia region. AFNI (https://afni.nimh.nih.gov/) is used by two sources (Boespflug et al., 2018; Williamson et al., 2022) for co-registration and skull-stripping, and elastix (https://elastix.lumc.nl/) is used for co-registration by one (Spijkerman et al., 2022). Not all methods correct for b1 inhomogeneities in the magnetic field, compensate for the presence of noise, or refer to a software/algorithm for normalising the intensities of the images prior to segmentation. The software most commonly used for generating the regions of interest is Freesurfer (https://surfer.nmr.mgh.harvard.edu/) (See Supplementary Table 2).

3.3.2. Model training

Thirty-two (66.68%) of the 48 quantification methods developed required training. Training and validation approaches included 'leave one out' (5 studies, 10.42%), 'k-fold cross-validation' (7 studies, 14.58%) and variations involving training data in one subset of data and testing in another (14 studies, 29.17%), training in one subset, validating in another, and testing in a further subset (4 studies, 8.33%), and a progressive/iterative training including altering thresholds and increasing sample sizes (2 studies, 4.17%).

3.3.3. Reference standard

The reference standard, or 'ground truth', most frequently used in PVS quantification method development was visual rating scores (13 studies, 27.08%). Other visual reference standards included visual count of PVS (5 studies, 10.42%) and 'visual inspection' (often lacking further detail of what this entailed, but where mentioned included differentiating PVS from lacunes; 5 studies, 10.42%). Manual segmentation was used in 11 (22.92%) studies, and manual annotation in eight (16.67%).

Table 8
Types of computational approaches.

	N	%
Classical image processing		
Intensity thresholding	7	14.58
Frangi filtering + Thresholding	6	12.50
Machine learning		
Stochastic geometry	3	6.25
Support Vector Machine (SVM)	3	6.25
Random Forest (RF)	2	4.17
Convolutional Neural Networks (CNN)	16	33.33
K-Nearest Neighbours (KNN)	1	2.08
Classical image processing ± Machine learning		
Intensity thresholding + Neural network	2	4.17
Frangi filtering + RF	3	6.25
Filtering + CNN	1	2.08
PVS Morphological detection (width, length, size)	2	4.17
Frangi filtering + CNN	2	4.17

Legend: N: number of sources, %: Percentage with respect to the 48 sources in the Method development group

Three studies (6.25%) did not describe a ground truth or reference standard, and a further 3 studies (6.25%) used more idiosyncratic reference standards (e.g., heuristically enhanced PVS, and probabilistic boxes for previously manually segmented PVS).

3.3.4. Populations and sample sizes

A brief overview of populations and sample sizes across all study types is provided in Section 3.2.2, Tables 2–4. The most frequent age group in which computational PVS quantification methods have been developed was in mid- and older adults (participants aged 40 years and over; 11 studies, 22.92%), followed by general adult (18 years and over; 10 studies, 20.83%), and older adult (60 years and over; 10 studies, 20.83%). Non-clinical populations were more widely represented than clinical (27 studies, 56.25% non-clinical, 17 studies, 35.42% clinical). Of the method development studies that used clinical populations, medical conditions within these populations included hereditary conditions (one study involving hereditary cerebral amyloid angiopathy carriers; 2.08%), six studies involving stroke patients (i.e., cerebrovascular; 12.5%), nine studies with samples with neurological or neurodegenerative diseases (e.g., Alzheimer's disease, multiple sclerosis; 18.75%), and one study involving patients with major depressive disorder; 2.08%). However, there is considerable overlap between the samples used by the different studies. Fig. 3 comparatively illustrates the distribution of sample sizes of the studies in this category. Dubost et al. (2019a), Dubost et al. (2019c), Dubost et al. (2017, 2020), Dubost et al. (2019b) and van Wijnen et al. (2019) use more than 1000 scans from the Rotterdam Scan Study. A manually annotated subset of it is used in the four studies described by Sudre et al. (2022). Ballerini et al. (2018) and Ramirez et al. (2011, 2015) use data from the Sunnybrook Dementia Study. Ballerini et al. (2018), González-Castro et al. (2016b, 2016a, 2017) and Wang et al. (2016b) all use scans from the Edinburgh Mild Stroke Studies. Other common data sources used are the Human Connectome Project (Choi et al., 2020; Lan et al., 2023; Sepehrband et al., 2019), the Lothian Birth Cohort 1936 (Ballerini et al., 2016; Wang et al., 2016b), the Multi-Ethnic Study of Atherosclerosis (MESA) cohort (Rashid et al., 2023) and the Southall And BRent REvisited (SABRE) ((Sudre et al., 2022), 4 participating studies). All these are well-known clinical and population studies with data available either by request to the data holders or through public databases, which would facilitate comparability in the results. However, it is unclear if PVS reference segmentations could be made available, as they are not included in any of the primary data sources mentioned. Studies using small or not publicly available samples (22 studies), or which did not specify the source of data used (4 studies) made up 54.17% of the total number of studies.

3.3.6. Assessing computational PVS quantification

A number of different approaches to assessing the quality of PVS quantification were used. This, together with the heterogeneity in image acquisitions and settings, make direct comparisons difficult. More commonly used assessments include measures of associations between computational output and reference standard (e.g., correlations), measures of accuracy (e.g., false positive/false negatives, ROC analyses), and measures of spatial agreement. Eighteen studies calculated association (correlation, regression) with reference standard measurements or scores (Table 7). We used the best performance reported amongst the myriad of evaluations carried out by each study, to discuss the overall performance of the different methods by category (i.e., semi-automatic vs. automatic, CNNs vs. conventional filtering, etc.) and estimate the overall magnitude of these correlations (Fig. 4). Not surprisingly, semi-automated methods (Ramirez et al., 2011; Wuerfel et al., 2008) achieved the highest correlation between observer-derived measurements. The approach presented by Choi et al. (2020), which uses a CNN to remove false positives from segmentation priors derived from thresholding the output from the Frangi filter, also reported very high intra-class correlation coefficient, but this was only validated in 10 scans. The

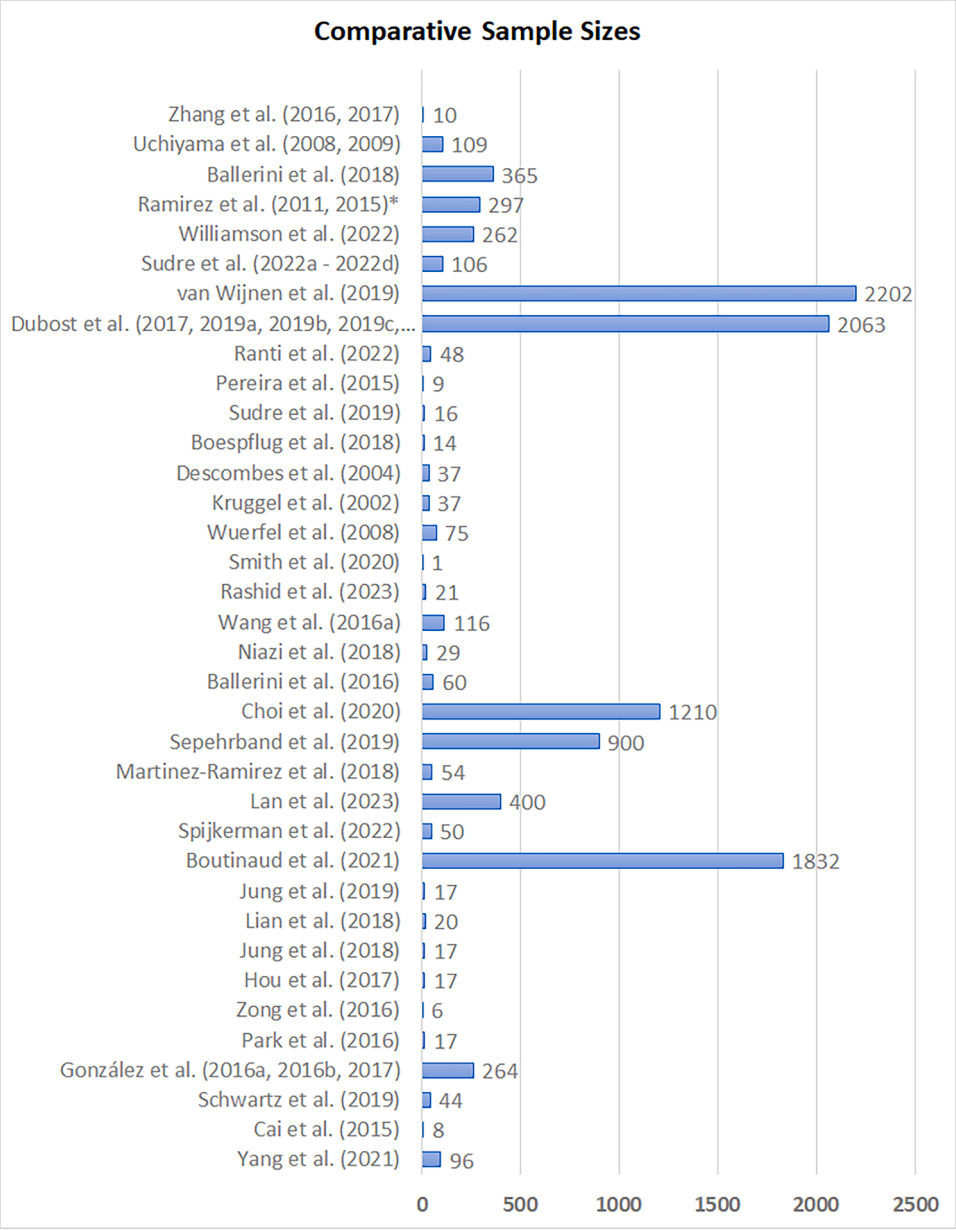

Fig. 3. Comparative sample sizes of the studies in the method development category. Dubost et al. and Ramirez et al. used overlapped subsamples from the same data sources. For these cases, the largest sample is represented in the graph.

publication describing the filtering approach proposed by Boespflug et al. (2018), reported the highest variability in the method's performance. Overall, correlations were on average $\beta = 0.881$, 95% CI = [0.869 0.892] (see diamond in pooled analysis of Fig. 4).

Accuracy metrics varied, largely depending on the reference standard, but all methods reporting accuracy results used various metrics (Table 7 and Supplementary Table 3). Average Dice similarity coefficient (DSC) values from sources that report them are illustrated in Fig. 5. The majority are between 0.6 and 0.8. Only (Ranti et al., 2022) stands out with a value of 0.9914 (Table 7, Fig. 5).

3.4. Improvement studies

Summaries of all improvement studies identified, which fitted our inclusion criteria (N = 8), are presented in Table 9. Targets for quantification improvement included image compression, motion artefacts and noise in general, image texture, comparison of vessel likelihood filters, and any source from which to derive useful recommendations for improving any of the methods developed up to date. Three sources are chapters in conference proceeding books (Bernal et al., 2020, 2021; Duarte Coello et al., 2023). The rest are journal publications.

3.4.1. Computational approach

Five out of the eight studies in this category utilised Frangi filtering and thresholding approaches (with three also assessing RORPO and/or Jerman filters). One study used a Deep Learning (CNN) approach (Zong et al., 2021), and two used mathematical observer models (Duarte Coello et al., 2024; Paz et al., 2009).

3.4.2. Reference standards

Three of the eight studies used visual rating scores (Bernal et al., 2020, 2021; Valdés Hernández et al., 2024a), two used visual assessment of the results (Paz et al., 2009; Valdés Hernández et al., 2024a), one used data without motion artefacts (Zong et al., 2021), and three

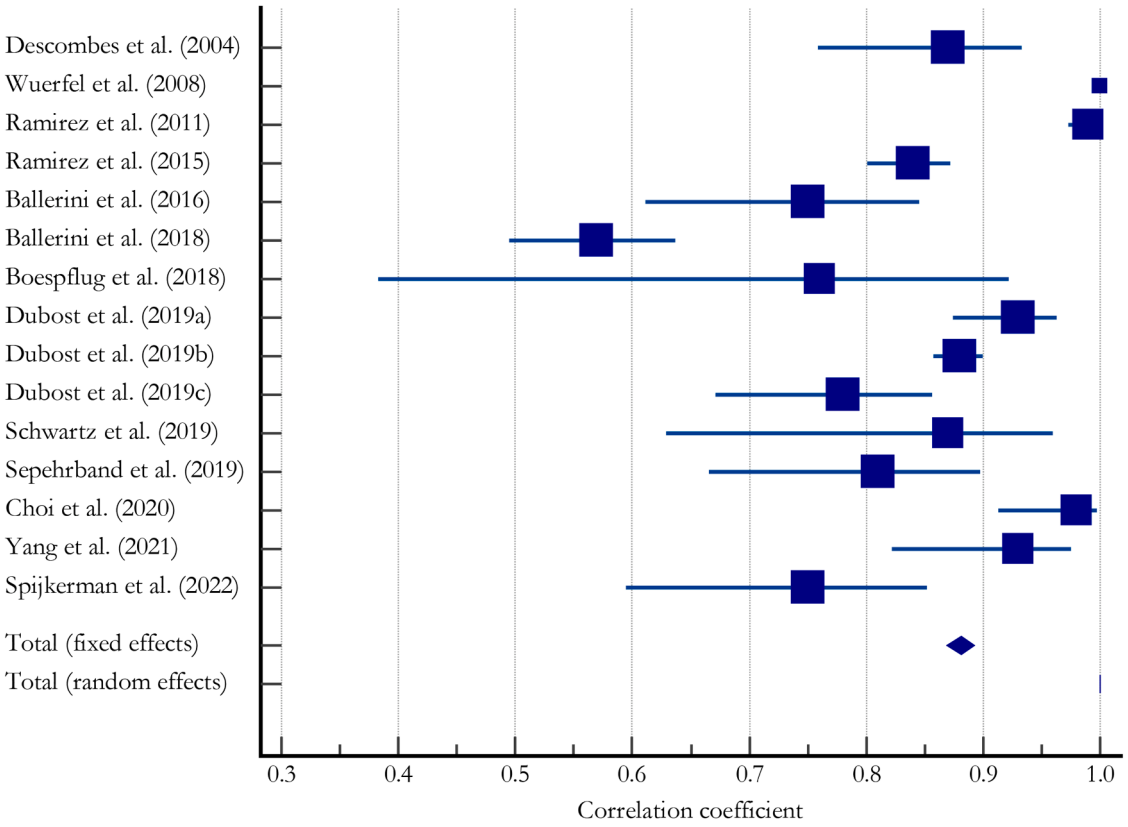

Fig. 4. Forest plot of correlation coefficients of best performance PVS quantification results (MedCalc (https://www.medcalc.org/)). Square size indicates relative sample size, diamond indicates pooled fixed and random effects correlation coefficients. (Dubost et al. 2019a refers to Dubost, Adams et al. 2019, Dubost et al., 2019b refers to Dubost, Yilmaz et al., 2019 and Dubost et al., 2019c refers to Dubost, Dünnwald, et al. 2019).

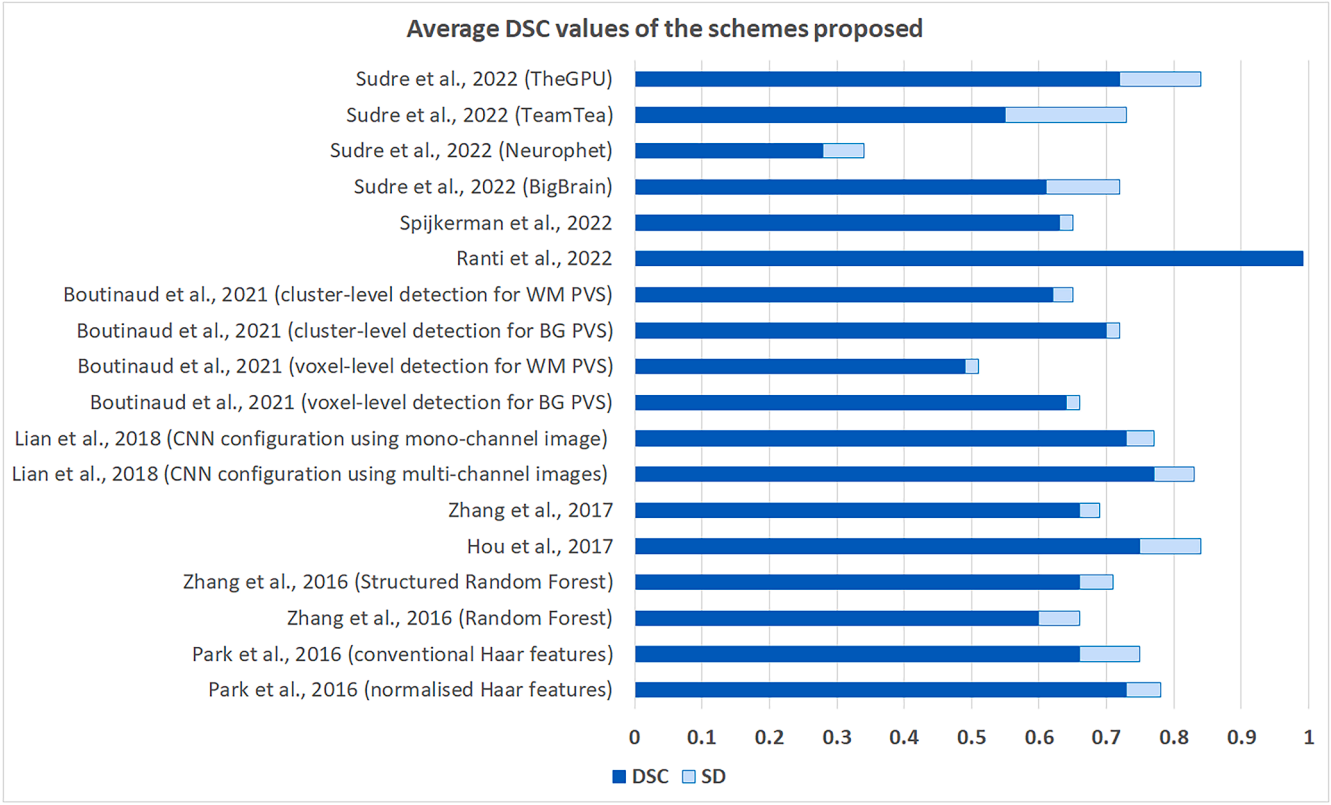

Fig. 5. Average DSC and standard deviations (interquartile range for the schemes proposed in Sudre et al. (2022)) results for each of the schemes proposed.

Table 9
Computational PVS quantification improvement study summaries.

Study	Overview	Approach	Reference standard	MRI sequences	Sample N	Result
(Paz et al., 2009)	Determines level of compression that allows for the detection of small lesions (including PVS)	Mathematical observer models	Visual assessment	T2w., Unspecified	MS., N = 10	The blurring effect introduced by the JPEG 2000 compression technology does not jeopardize the lesion detection task when using bit rates higher than 0.125 bpp.
(Bernal et al., 2020)	Framework for improving PVS segmentation by analysing image texture (i.e., energy, contrast, correlation, homogeneity, entropy and variance) and filtering when required (i.e., if the texture analysis suggest the image is noisy), using a total variation filter.	Frangi filtering and thresholding	Visual rating scores	T2w., 3T	Mild stroke., N = 60	Combination of all 6 textural features improved classification in noisy vs. less noisy/clean (AUC=88.8%), R2 values were approximately 13% and 40% for count and volume of PVS in the basal ganglia in original scans, and increased to 30% and 47% for the same measurements when filtered. In the CSO, the improvement in R2 values was from 0.73% to 11% for counts and from 7.55% to 35% for volume. Overall, the scheme proposed improves the PVS quantification, but it is unclear if can be extended to other protocols/ images from other scans.
(Bernal et al., 2021)	Explores motion artefact reduction. PVS segmented using Frangi filter. Step 1: quality assessment. Step 2: if images are of bad quality (contain motion artefacts), filter them by manually removing segments of k-space displaying errors. Step 3: filter images with Frangi filter. Step 4: threshold.	Frangi filtering and thresholding	Visual rating scores	T2w., 3T	Mild stroke., N = 60	Visual x Automated Counts: pBG = 0.50, pCSO=0.34; Visual x Automated Volume: pBG = 0.72, pCSO = 0.86. This proof-of-concept paper shows that processing images depending on their quality leads to improved results.
(Zong et al., 2021)	Determines effect of motion artefacts and motion correction of PVS quantification.	Deep learning (CNN)	Data without motion artefacts	T2w., 7T	Healthy adults., N = 39	Without motion correction (MC), VF, and count decreased significantly with increasing head rotation. MC improved PVSV visualization in all cases with severe motion artefacts. While both raters agreed on the improvements of PVSV visibility by MC in all cases with severe motion artefacts, the agreement was only 43% in other cases. MC decreased diameter in white matter (WM) and increased VF, count, and contrast in basal ganglia and WM. The changes of VF, count, and contrast after MC strongly correlated with motion severity. MC eliminated the significant dependences of VF and count on rotation and reduced the inter-subject variations of VF and count.
(Bernal et al., 2022)	Compares different vesselness filtering methods with synthetic data and shows quantification problems.	Frangi, Jerman, RORPO filtering and thresholding	T2w-like images with synthetically generated PVS-like tubular structures (i.e., cylinders)	T2w-like synthesised data	Synthetic data	RORPO best when voxels isotropic. Performance of all filters affected by image quality. Filters unable to distinguish PVS from hyperintense structures. Area under precision-recall curve dropped substantially (Frangi: from 94.21 [IQR 91.60, 96.16] to 43.76 [IQR 25.19, 63.38]; Jerman: from 94.51 [IQR 91.90, 95.37] to 58.00 [IQR 35.68, 64.87]; RORPO: from 98.72 [IQR 95.37, 98.96] to 71.87 [IQR 57.21, 76.63] without and with other

(*continued on next page*)

Table 9 (*continued*)

Study	Overview	Approach	Reference standard	MRI sequences	Sample N	Result
						hyperintense structures, respectively.
(Duarte Coello et al., 2024)	Uses a purpose-built digital reference object to construct an in-silico phantom for establishing the limits of validity of PVS quantification, and validates it using a physical phantom. Uses cylinders of different sizes as models for PVS. Also evaluates the influence of 'PVS' orientation, and different sets of parameters of the two vesselness filters that have been used for enhancing tubular structures, namely Frangi and RORPO filters, in the measurements' accuracy.	Frangi or RORPO filtering and thresholding.	Ideal values, physically measured using a hole gage and a calliper in the physical phantom, or derived from the cylinder equation in the in-silico phantom	T2w contrast using a turbo spin-echo sequence (Physical phantom imaged at 7T)	Synthetic data	PVS measurements in MRI are only a proxy of their true dimensions, as the boundaries of their representation are consistently overestimated. The success in the use of the Frangi filter relies on a careful tuning of several parameters. Alpha= 0.5, beta= 0.5 and c= 500 yielded the best results. RORPO does not have these requirements and allows detecting smaller cylinders in their entirety more consistently in the absence of noise and confounding artefacts. The Frangi filter seems to be best suited for voxel sizes equal or larger than 0.4 mm-isotropic and cylinders larger than 1 mm diameter and 2 mm length. 'PVS' orientation did not affect measurements in data with isotropic voxels.
(Duarte Coello et al., 2023)	Curve approximation for accurate estimation of PVS morphometrics: length and diameter, out from PVS segmentations.	Approximation of the connected component to a Bezier curve	Ideal values, derived from counting the voxels in a binarised curve, derived from a PVS-DRO with voxel size of 0.35 × 0.35 × 0.35 mm3	Not applicable	Not applicable	The Bézier curve approximation performs better than the ellipsoid, being closer to the ideal measurements. For diameter: MSE Bezier=0.26mm, MSE ellipsoid=7.74mm, For length: MSE Bezier=0.051mm, MSE ellipsoid=10.34mm
(Valdés Hernández et al., 2024a)	Evaluates modifications and alternatives to a state-of-the-art PVS segmentation method that uses a vesselness filter to enhance PVS discrimination, followed by thresholding of its response, applied to brain magnetic resonance images (MRI) from patients with sporadic small vessel disease acquired at 3T.	Frangi or Jerman filtering and thresholding.	Visual rating scores (McLullich-Potter-Wardlaw), and visual inspection	T1w (1 mm isotropic), T2w (0.90 mm × 0.937 mm × 0.937 mm), 3T (SWI and FLAIR are used for visual assessment of the results)	Mild stroke, N=228. (mean age (SD): 65.77 (11.17) years, 34% female)	The method is robust against inter-observer differences in threshold selection, but separate thresholds for each region of interest (i.e., BG, CSO, and midbrain) are required. Noise needs to be assessed prior to selecting these thresholds, as effect of noise and imaging artefacts can be mitigated with a careful optimisation of these thresholds. PVS segmentation from T1w images alone, misses small PVS, therefore, underestimates PVS count, may overestimate individual PVS volume especially in the basal ganglia, and is susceptible to the inclusion of calcified vessels and mineral deposits. Visual analyses indicated the incomplete and fragmented detection of long and thin PVS as the primary cause of errors, with the Frangi filter coping better than the Jerman filter.

Legend: PVS: perivascular spaces, T1w: T1-weighted MRI sequence, T2w: T2-1weighted MRI sequence, SWI: Susceptibility Weighted Imaging, FLAIR: Fluid-Attenuated Inversion Recovery MRI sequence, SD: Standard Deviation, RORPO: Ranking Orientation Responses of Path Operators, IQR: Inter-Quartile Range, BG: basal ganglia region, CSO: centrum semiovale region, PVS-DRO: PVS Digital Reference Object, MSE: Mean Squared Error3.4.1. Computational approach

used measurements of synthetically-generated cylindrical structures (Bernal et al., 2022; Duarte Coello et al., 2023, 2024) as reference standards.

3.4.3. MR sequences and field strengths

All studies aimed at improving the detectability and segmentation accuracy of PVS used T2w imaging, or synthesised T2w-like images in one case, as this is the preferred sequence to identify PVS as per STRIVE recommendations (Wardlaw et al., 2013). Three studies used 3T images, two used 7T images, and one study did not specify field strength. The study that used T1w images (Valdés Hernández et al., 2024a) found inconsistencies in the results compared with those from T2w, and suggested these might reflect presence of vessel mineralisation, hypointense, as PVS, in T1w MRI sequence.

3.4.4. Populations and sample sizes

Populations used in improvement studies included clinical groups (multiple sclerosis, mild stroke), and healthy adults. Three studies used synthetic data. Sample sizes ranged from N = 10 to N = 228 participants, although one study (Bernal et al., 2022) used intensity values from T2w

images from 700 community-dwelling older individuals, in addition to WMH probability distribution maps derived from 47 patients with systemic lupus erythematosus to generate the Digital Reference Object used for the evaluations.

3.4.5. Improvement study results

Each of the eight improvement studies had different targets (Table 9). One study examined image compression (Paz et al., 2009), finding that JPEG 2000 compression does not jeopardise PVS detectability when bit rates are greater than 0.125bpp. One study proposes a framework for PVS quantification by analysing image texture features and applying a total variation filter if necessary, to improve PVS quantification in noisy versus less noisy or clean imaging (AUC = 88.8%) (Bernal et al., 2020). Three studies examined the impact of motion artefacts on PVS quantification, finding that correcting motion artefacts improved PVS quantification when using Frangi filtering plus thresholding (Bernal et al., 2021) and when using a convolutional neural network approach (Zong et al., 2021), or that simply using higher thresholds after filtering for noisy images compared with the thresholds used for clean images will be enough (Valdés Hernández et al., 2024a). Comparison of the performance of Frangi, RORPO and Jerman filters for highlighting PVS candidates was the subject of three studies. One study compared the three filtering approaches and found that RORPO performed best in isotropic imaging, but that all filter types were unable to distinguish between PVS and other hyperintense features (Bernal et al., 2022). Another compared Frangi with Jerman and found more incomplete and fragmented detection of long and thin PVS with Jerman than with Frangi (Valdés Hernández et al., 2024a). Another compared the performance of RORPO and Frangi in phantoms to conclude that RORPO, in addition of having less adjustment requirements, detected smaller cylinders in their entirety more consistently while Frangi seemed to be best suited for voxel sizes equal or larger than 0.4 mm-isotropic and cylinders larger than 1 mm diameter and 2 mm length (Duarte Coello et al., 2024). One study diverges from the rest in terms of aims (Duarte Coello et al., 2023), as its focus is the improvement in the accuracy of the quantification of the PVS morphometrics, namely length and width, and not in the detection or segmentation of PVS *per se*. PVS morphometrics are traditionally assessed by measuring the maximum and minimum diameters of the ellipsoid that encircles each PVS (Ballerini et al., 2020b). The traditional approach, implemented in Matlab by the function regionprops3, is accurate if the PVS are linear and straight, but not if they are curved or elongated with irregular shapes. Three sources have linked data/code repositories: Bernal et al. (2022), Duarte Coello et al. (2024), and Valdés Hernández et al. (2024a) to enable compatibility in follow-up improvements, reproducibility, and fair comparability of these results with those from further analyses.

3.5. Application studies

Summaries of all included application studies (N = 59) are presented in Table 10. Methodological and clinical differences between the studies ruled out meta-analysis of the estimates obtained.

3.5.1 Factors explored in relation to PVS burden

Application studies explored a range of factors in relation with PVS. These are: PVS morphology and topology (6 studies, 10.17%), broad epidemiology (typically clinical risk factors and cognitive/functional outcomes, 19 studies, 32.20%) in the presence or not of a pathology or disabling event (e.g., in patients with stroke, traumatic brain injury, or Parkinson's disease, 4 studies), pathophysiology and manifestation of a particular disease or disorder (e.g., Parkinson's disease, Huntington's disease, autism, obstructive sleep apnoea, COVID, diabetes mellitus, among others, 22 studies, 37.29%), vascular function or vascular disease (including concurrent SVD lesions and white matter hyperintensity burden, 13 studies, 22.03%), cognition (10 studies, 16.95%), sleep (5 studies, 8.47%), retinal vasculature parameters (2 studies, 3.39%), space flight duration (2 studies, 3.39%), and one study exploring PVS in relation to preterm birth. Often, multiple factors or themes were explored (e.g., PVS associated with cognition and established disease or disorder). Two studies (3.39%) investigated, in the same sample, various aspects of PVS heritability in twins (Choi et al., 2020; Lee et al., 2021).

3.5.2. Computational PVS quantification methods used

Many of the computational methods used in the application studies have been described in Section 3.3, and have been applied directly or used as the basis of PVS quantification approaches in application studies. The most frequently applied method was thresholding the response of the Frangi filter, as described by Ballerini et al. (2016, 2018) (12 studies) or in the frameworks proposed by Sepehrband et al. (2019) (10 studies), Smith et al. (2020) (1 study), or Ranti et al. (2022) (1 study), which in total make up for 54.24% of the application studies. Ten studies use CNN configurations, mainly U-Net and U-ResNet (16.95%), to assess PVS burden, and four studies use this approach to post-process the output from the Frangi filter. Morphological detection as proposed by Schwartz et al. (2019), followed by thresholding is used in six studies, while a study uses the morphological detection approach described by Sato et al. (1998).

Computational PVS quantification methods applied but not described in Section 3.3. include approaches based on Guerrero et al. (2018) method (a deep learning/CNN approach), Yushkevich et al. (2006) method (a semi-automated, 6-connected voxel active contours approach), and seven in-house methods (including thresholding and filtering methods, and approaches based on Dubost et al. (2019b) and Sepehrband et al. (2019) methods). One study refers using the 2D U-Net approach for multisite learning as developed by Remedios et al. (2020) for segmenting haemorrhages in CT scans. These were not among 'method development' papers included in this review as they did not independently meet inclusion criteria (e.g., the quantification approach may not have been designed explicitly for PVS detection (Guerrero et al., 2018; Remedios et al., 2020), or may have relied heavily on a manual component (Yushkevich et al., 2006)). A list of the computational PVS quantification approaches and the frequency of their use in the application studies identified in this review is presented in Table 11.

3.5.3. MR sequences and field strengths

Frequencies of MR sequences and field strengths used in 'application' studies in comparison with other study types are outlined in Section 3.2.3, Tables 5 and 6. The most common combinations of MR sequences used in these studies were T1w and T2w (19 studies). This was also the combination of sequences used by Choi et al. (2020), which can be considered both: a 'method development' and an 'application' study. T1w alone, and the combination of T1w, T2w, T2*w and FLAIR (10 studies each) were also commonly used. This combination, however, was not used specifically for identifying PVS, but was used by full pipelines to extract regions of interest and obtain other imaging markers that were analysed by the studies in relation to PVS.

Application studies most frequently used 3T imaging (42 studies, 71.19%), although a large proportion used 1.5T imaging (20 studies, 33.9%) and only five studies used 7T (8.47%). This differs from method development studies, where distribution of field strengths was fairly evenly distributed, with a slight bias towards 1.5T imaging.

3.5.4. Population types and sample sizes

Application studies were almost evenly split between those using a clinical population (50.85%) and those using only a non-clinical population (49.15%). Participants were most commonly independently living older adults (>60 years; 18 studies, 30.51%), followed by patients with cerebrovascular disease-related phenotype (e.g., stroke patients, hypertensive patients, patients with artherosclerosis) (9 studies, 15.25%). In terms of population characteristics, application and method development studies shared similar distribution (i.e., proportion). Median sample size of PVS application studies was N = 161 (IQR = 482.5), with two multicentre epidemiological studies with sample sizes greater than

Table 10
Application study summaries.

Study	Overview	PVS quantification method	MRI sequences	Sample N	Results
(Berezuk et al., 2015)	Correlation between PVS and sleep.	(Ramirez et al., 2011)	T1w, T2w., 3T	Adults with stroke risk. N = 26	Sleep efficiency negatively correlated with PVS (ρ = -0.47, p = .03) and BG PVS (ρ = -0.54, p = .01). Wake after sleep onset positively correlated with BG PVS (ρ = 0.52, p = .02) and negatively correlated with duration of N3 (ρ = -0.53, p = .01)
(Wang et al., 2016a)	Exploration of peripheral blood markers in association with basal ganglia PVS in patients with recent minor ischemic stroke.	(Wang et al., 2016b)	T1w, T2w, FLAIR., 1.5T	Mild ischaemic stroke patients. , N = 100	Univariate analysis found BG PVS count and volume increased with age (p = .003, = .02). BG PVS count increased with hypertension (p = .013), but not PVS vol. No association found for BG PVS count or vol with sex, smoking, or diabetes. Univariate analysis found association between BG PVS count and thrombosis: F 1 + 2 (p = .05) and TAT (p= .013), and BG PVS vol and TAT (p = .037). Associations lost significance after adjusting for age, sex, and risk factors, but endothelial function (vWF) became negatively associated with BG PVS count (p = .032).
(Valdés Hernández et al., 2019)	Exploration of Huntington's Disease (HD) in Colombian family groups, with regards to neuroimaging (volumetrics, PVS burden) and cognitive, behavioural, and motor factors.	(Wang et al., 2016b)	T1w, T2w, FLAIR., 1.5T	Huntington's Disease (patients, families)., N = 29	GM volume in BG and thalami differentiated manifest disease vs. disease vulnerability in HD families. PVS burden was predictive of reduced fluid intelligence in HD patients, but not in vulnerable group. Raven's matrices best discriminator between overt HD vs. vulnerability to disease.
(Ballerini et al., 2020b)	Application of computational PVS segmentation in the CSO, and assessment of association of PVS volume, count, and morphology, with vascular risk and WMH.	(Ballerini et al., 2016)	T1w, T2w, FLAIR., 1.5T	LBC1936., N = 533	PVS segmentation acceptable for 77% of participants. No significant differences in successful segmentation, other than small age difference (unsuccessful were older by 51 days on average). Visual PVS score correlated positively with all computational PVS measures. All PVS measures (score and comp) correlated with WMH (visual and volume), with computational measures other than count showing stronger association. Greater PVS size and width associated with hypertension and stroke. No association between PVS and diabetes, CVD, or cholesterol.
(Ballerini et al., 2020a)	Associations between morphological measurements of the retinal vasculature, obtained from fundus camera images, and of features of Small Vessel Disease (SVD), as white matter hyperintensities (WMH) and perivascular spaces (PVS), obtained from MRI brain scans.	(Ballerini et al., 2018)	T1w, T2w, T2*w, FLAIR. 1.5T	LBC1936., From N = 866, 381 had both retina measurements and PVS. 478 had both Retina and WMH.	Arteriolar bifurcation coefficients, vessel tortuosity and fractal dimension predicted WMH volume in 23% of the trials. Arteriolar widths, venular bifurcation coefficients, and venular tortuosity predicted PVS in up to 99.6% of the trials.
(McGrory, et al., 2020a)	Comparison of computationally-derived PVS morphologies with retinal vessel morphologies in older people.	(Ballerini et al., 2018)	T1w, T2w, T2*w, FLAIR., 1.5T	LBC1936., N = 381.	Increasing total PVS volume and count associated with decreased central retinal artery equivalent (CRAE) in left eye (vol B = -0.17, count B = -.184, p < .01).
(Choi et al., 2020)	Investigate heritability of MRI-visible PVS in healthy young adult twins and non-twin siblings.	(Choi et al., 2020)	T1w, T2w, 3T	N=138 monozygotic, N=79 dizygotic twin pairs, and N=133 nontwin sibling pairs (age 28.7 ± 3.6 years) from the Human Connectome Project	In univariate analysis, heritability estimates of BG PVS was 65.8%, and for WM PVS it was 90.2% after adjusting for age and sex. In bivariate analysis, both BG PVS and WM PVS showed low to

(*continued on next page*)

Table 10 (*continued*)

Study	Overview	PVS quantification method	MRI sequences	Sample N	Results
					moderate genetic correlations (0.30–0.43) but high shared heritabilities (71.8–99.9%) with corresponding regional and intracranial volumes. Older age was significantly associated with larger PVS volume in both regions even after adjusting for clinical and volumetric variables, while blood pressure was not associated with PVS volume although there was weak genetic correlation.
(Jokinen et al., 2020)	Exploration of global SVD burden on longitudinal cognitive and functional outcomes (baseline and 3- and 7-year follow-up included).	(Guerrero et al., 2018)	T1w, T2w, FLAIR., 1.5T, 0.5T	LADIS study., N = 561	PVS volume significant predictor of processing speed performance ($p = .047$) and decline in processing speed ($p < .001$), and of decline in memory ($p = .009$) and in total VADAS score ($p < .001$). PVS volume was not significant predictor of disability or death at 7-year follow up. Combined measures of global burden of SVD-related brain changes were a more powerful predictor of cognitive decline than individual features.
(Liu et al., 2020)	Relationships between visible VRS on MRI and seizures, to detect changes in glymphatic function.	In-house method (Frangi filtering)	T1w, T2w, FLAIR., 3T	Idiopathic Generalised Epilepsy (IGE) children, (N = 32) and controls (N = 30)	Visible PVS counts were higher in IGE than control group (IGE: 234.34 ± 113.88 vs. Control: 111.83 ± 52.46; P < 0.001). Similar results were found in PVS volume (IGE: 1377.47 ± 778.79 mm3 vs. Control: 795.153 ± 452.49 mm3; P = 0.001). Visible PVS counts and volume positively correlated with seizure duration (r_counts = 0.638, r_volume = 0.639; P < 0.001) and gradually decreased with time after seizure onset (r_counts = −0.559, r_volume = −0.558; P < 0.001).
(Piantino et al., 2020)	Exploration of morphological characteristics of PVS and their association with demographic factors in adolescents.	(Schwartz et al., 2019)	T1w, T2w., 3T	Adolescents., N = 118	Males had higher PVS number than females (male mean = 98.4 (+/- 50.5), female mean = 70.7 (+/- 36.1); p < .01). PVS burden was bilaterally symmetric, with PVS more common in frontal and parietal lobes than occipital/ temporal. Age and pubertal status not associated with PVS burden.
(Valdés Hernández et al., 2020)	Associations of CSO-PVS volume and count with brain IDs and cognitive abilities in 700 community-dwelling individuals from the Lothian Birth Cohort 1936 who underwent detailed cognitive testing and multimodal brain MRI at mean age 72.7 years.	(Ballerini et al., 2018)	T1w, T2*w., 1.5T	LBC1936., N = 540	CSO-PVS burden is not directly associated with general cognitive ability in older age.
(Zong et al., 2020)	Characterisation of morphology of perivascular spaces and their enclosed blood vessel. Exploration of age, spatial heterogeneity, and dynamic changes (with carbogen breathing).	(Lian et al., 2018)	T1w, T2w., 7T	Healthy adults., N = 46	PVSV count and volume fraction significantly increase with age in BG. rCNR increased with age in BG, MB, and WM. PVSV diameter showed positive association with age, but not significant. Carbogen breathing significantly increased PVSV volume fraction in BG and WM, and significantly increased rCNR in thalamus, BG, and WM compared to air breathing.
(Barisano et al., 2021)	Exploratory analysis of PVS pathophysiology: PVS burden and clinical, cognitive, and emotion factors in healthy adults	(Sepehrband et al., 2019)	T1w, T2w., 3T	Human Connectome Project., N = 897	Mean WM PVS vol = 5.03 cm (+/- 2.15). PVS ratios highest in WM adjacent to cingulate, insula, supramarginal gyrus; smallest ratios in WM underlying cuneus, entorhinal cortex, frontal pole. PVS volume higher in older and male participants. BMI, time of day

(*continued on next page*)

Table 10 (*continued*)

Study	Overview	PVS quantification method	MRI sequences	Sample N	Results
					(of scan), and genetics significantly associated with PVS. Average numbers of hours of sleep and the sleep quality index were not associated with PVS ratios.
(Chan et al., 2021)	Quantification of the percent volume of regional PVS (excluding cortex) in patients with early Huntington disease (HD) and exploration of the relationship between PVS and disease severity.	In-house method described in-text. Thresholding.	T1w, T2w., 3T	Huntington's disease., N = 48	Patients with HD had the greatest percent volume of PVS in the putamen (left putamen: odds ratio 2.06 [95% confidence interval (CI) 1.62–2.62], HD 3.27% [95% CI 2.83–3.78] vs controls 1.62% [95% CI 1.32–1.97], $p < 0.001$; right putamen: odds ratio 1.66 [95% CI 1.33–2.08], HD 3.43% [95% CI 2.94–4.01] vs controls 2.09% [95% CI 1.79–2.45], pfdr < 0.001) and several white matter regions compared to controls. PVS increased with disease severity.
(Hamilton et al., 2021)	Association between SVD and longitudinal cognitive performance in older adults (Lothian Birth Cohort 1936).	(Ballerini et al., 2018)	T1w, T2w, FLAIR., 1.5T	LBC1936., N = 540	All cognitive scores declined significantly over 9-year period. With covariates, total SVD negatively associated with slope of general cognitive ability and processing speed, but not verbal memory or visuospatial ability. SVD burden accounted for 4% variance in slow of cog ability and 5% variance in slope of processing speed. SVD burden associated with greater decline in general cog prior to FDR and without covariates. No significant association between SVD burden and other cognitive variables. SVD burden associated with overall decline in cognitive ability.
(Hamilton et al., 2021)	Association between SVD and domain-specific cognition in (community-dwelling) older adults.	(Ballerini et al., 2018)	T1w, T2w, FLAIR., 1.5T	LBC1936., N = 540	Computational SVD score negatively associated with cognitive domains, remaining significant after covariates included. SVD burden accounted for 13% variance in general cognition, 14% variance in processing speed, 7% variance in verbal memory, and 3% variance in visuospatial ability. Independent negative association found between SVD burden and processing speed.
(Huang, Zhu, et al., 2021)	Associations between PVS volume and imaging, vascular, cognitive, and demographic factors in healthy adults.	(Lian et al., 2018)	T1w, T2w, FLAIR, MRA., 3T	Healthy adults., N = 103	Age and hypertension positively associated with BG PVS volume (B = 0.224, $p = .023$; B = 0.282, $p = .004$). Deep WM PVS positively associated with intracranial volume (B = 0.262, $p = .007$).
(Huang et al., 2021a)	Exploration of relationship between WMH, PVS, and interstitial fluid.	(Lian et al., 2018)	T1w, T2w, FLAIR, DTI., 3T	Older adults. , N = 136	Most PVS spatially connected to dWMH (89%). PVS and WMH volumes significantly positively correlated (r = .002, $p < .001$). Free water found to mediate PVS x WMH association in whole sample (B = .069, $p = .037$) and in subset with high WMH load (B = .118, $p = .006$).
(Lee et al., 2021)	Assessment of spatial similarity (Dice, structural similarity, mean squared error) of PVS in adult twin and non-twin sibling pairs (Human Connectome Project).	(Choi et al., 2020)	T1w, T2w., 3T	Human connectome project., N = 700	PVS most spatially similar within MZ twins (Dice = 0.38, SSIM = 0.96, MSE = .005), with significantly higher Dice and SSIM and significantly lower MSE than DZ twins ($p < .001$, $p = .015$, $p = .004$) and NT siblings (all $p < .001$). Results suggest genetic influence on PVS location.

(*continued on next page*)

Table 10 (*continued*)

Study	Overview	PVS quantification method	MRI sequences	Sample N	Results
(Piantino et al., 2021)	Exploration of PVS in association with morbidity following mild TBI in veterans.	(Boespflug et al., 2018; Schwartz et al., 2019)	T1w., 3T	Veterans., N = 56	PVS number and volume positively correlated across hemispheres ($p <$ .001). PVS N and vol highest in temporal lobes. Number of mTBIs in military and sBP both significantly related to PVS N and vol. Age significantly associated with PVS vol. After adjustment for covars, each additional mTBI sustained in military had average 0.1 increase in (ln) PVS number/cm3 of WM and 0.1 increase in (ln) PVS vol (mm3)/cm3 of WM. No association found for mTBI outside military, blast mTBI without LOC, or poor sleep with PVS vol or N. No difference in PVS burden between clinically high sBP and normal sBP categories. Significant interaction between poor sleep and N military mTBI on PVS vol ($p = .04$ in poor sleep vs good sleep). Low significant positive correlation between PVS N and vol and severity of post-concussive symptoms ($p = .03$ and $p = .04$, respectively). Significant correlation between PVS N and vol and post-concussive balance problems ($p = .0002$ each).
(Ranti et al., 2021)	Assessment of link between PVS and trauma.	Unspecified	Unspecified., 7T	MDD. , N unspecified.	After controlling for age and gender, number of traumatic live events correlated positively with PVS volume in MDD patients (r = .5, $p = .028$) and in the overall population (r = .34, $p = .024$). Age correlated with PVS count (r = .37, $p = .013$), volume (r = .53, $p <$ .001), and density (r = .68, $p <$ .001).
(Sepehrband et al., 2021)	Exploration of PVS volume in association with mild cognitive impairment and associated neuroradiological findings.	(Sepehrband et al., 2019)	T1w, FLAIR., 3T	Alzheimer's Disease., N = 596	Early MCI patients have altered PVS presence compared to normal controls, irrespective of amyloid-B. Lower PVS presence in anterosuperior medial temporal lobe (1.29 times lower PVS fraction in MCI than cognitively normal). Higher PVS fraction in CSO in females (1.47 times higher PVS vol fraction in cognitively impaired).
(Wang et al., 2021)	Compute quantitative and morphological PVS features and to assess their associations with vascular risk factors and cerebral small vessel disease.	(Lian et al., 2018)	T1w, T2w., 3T	Healthy adults., N = 161	WM-PVS visual score and count were associated with hypertension, WM-PVS size was associated with diabetes, WM-PVS and BG-PVS were associated with CSVD markers, especially white matter hyperintensities, WM/BG-PVS quantitative measures were widely associated with vascular risk factors and CSVD markers.
(Barisano et al., 2022)	The effect of prolonged spaceflight on cerebrospinal fluid and perivascular spaces of astronauts and cosmonauts	(Sepehrband et al., 2019)	T1w, 3T	NASA astronauts (N=24); ROS cosmonauts (N=13); ESA astronauts (N=not reported); Healthy volunteers (N=13); Shuttle NASA astronauts (N=7)	PVS enlarged long-duration spaceflight. WM-PVS were correlated with a reduction in the subarachnoid space at the vertex. WM-PVS increase was correlated with mission duration. BG-PVS were associated to previous spaceflight experience.
(Barnes et al., 2022)	Topological relationship between PVS and WMH, and potential PVS influence on WMH progression across 3 scanning waves.	(Ballerini et al., 2018)	T1w, T2w, T2*, FLAIR., 1.5T	LBC1936., N = 29	Most deep WMH clusters were adjacent to or enclosed PVS (77% wave 1, 76% wave 2, 69% wave 3). In WMH clusters that increased most between scan waves, most

(*continued on next page*)

Table 10 (*continued*)

Study	Overview	PVS quantification method	MRI sequences	Sample N	Results
					increased around PVS (wave 1-2 = 73%, wave 2-3 = 72%).
(Cheng et al., 2022)	Determine risk factors for hippocampal cavities in a marginally housed population, to shed light on possible aetiology, one of which is that they are PVS.	In-house intensity-based thresholding 3D segmentation	T1w, 3T	Marginally housed population (N=240)	On average, a 1 mmHg greater systolic blood pressure was associated with a 2.17% greater total hippocampal cavity (i.e, ~PVS) volume (95% CI = [0.57%, 3.79%], p = .0076), while each cigarette smoked per day trended toward a 2.69% greater total hippocampal (~PVS) volume (95% CI = [−0.87%, 5.54%], p = .058). A diagnosis of stimulant dependence was associated with a 95.6% greater total hippocampal (~PVS) volume (95% CI = [5.39%, 263.19%], p = .0335). Hypertension and diagnosis of stimulant dependence were associated with a greater total volume of hippocampal cavities (i.e., ~PVS).
(Donahue et al., 2022)	Examine relationship between PVS volume and magnetic resonance spectroscopy metabolites in Parkinson's Diseaase.	(Ballerini et al., 2018) as used in (Sepehrband et al., 2019)	T1w, 3T	Idiopathic Parkinson's Disease patients (N=17)	Greater PVS volume was associated with higher levels of choline-containing compounds (Cho; P = 0.047) in frontal white matter and lower PVS volume with higher levels of N-acetyl compounds (NAA; P = 0.012) in anterior middle cingulate cortex.
(Haddad et al., 2022)	Comparison of Diffusion Tensor Imaging Metrics in Normal-Appearing White Matter to Cerebrovascular Lesions and Correlation with Cerebrovascular Disease Risk Factors and Severity	(Ramirez et al., 2015)	T1w, T2w, T2*w, FLAIR, fMRI, DTI, 3T	Ontario Neurodegenerative Disease Research Initiative (ONDRI) study participants (N=152)	FA in NAWM was inversely related to hypertension and modified Rankin scale (mRS). There were differences between conventional DTI metrics, FA, MD in cerebral vascular lesions and healthy tissue types. FA in PVS was not significantly different from FA in NAGM, but differed from the rest of the normal and abnormal tissue types.
(Hupfeld et al., 2022)	Exploration of longitudinal effects of long (~6 month) spaceflight on PVS, with pre-launch and post-landing measures.	(Schwartz et al., 2019)	T1w., 3T	Astronauts., N = 11	PVS identified in all participants at all time-points. No statistically significant changes in PVS characteristics from pre- to post-flight in whole group. Novice astronauts showed increase in total PVS vol from pre- to post-flight while experienced astronauts showed decrease (p = .02). No difference in PVS between SANS/no SANS experience.
(Kamagata et al., 2022)	Examine the association of MRI indices of glymphatic system (i.e., PVS VF, NAWM, ALPS) with amyloid deposition and cognition in Mild Cognitive Impairment and Alzheimer Disease	(Sepehrband et al., 2019)	DWI, T1w, FLAIR, 3T	AD (N=36), MCI (N=44), cognitively normal (N=31) from ADNI-2 database	Patients with AD had significantly higher total, WM, and basal ganglia PVS VF (Cohen d = 1.15–1.48; p < 0.001) and FW-WM (Cohen d = 0.73; p < 0.05) and a lower ALPS index (Cohen d = 0.63; p < 0.05) than healthy controls. Meanwhile, the MCI group only showed significantly higher total (Cohen d = 0.99; p < 0.05) and WM (Cohen d = 0.91; p < 0.05) PVSVF.
(Langan et al., 2022)	Identify and quantify differences in perivascular spaces between a group of 10 COVID-19 patients and a similar subset of controls to determine whether PVS might be biomarkers of COVID-19-mediated neuroinflammation.	(Smith et al., 2020)	T1w., 7T	COVID-19., N = 19	PVS count was significantly higher in COVID-19 patients compared to healthy controls (p = 0.0373). There was no statistically significant difference between other PVS measures or intracranial volume metrics between groups.
(Li et al., 2022)	Explore the association of PVS with duration of simple febrile seizures-(SFS) in children	PVS segmented by FSL and custom algorithm following (Ballerini et al., 2018)	T1w, T2w, FLAIR, 3T	Children N=105 (with SFS lasting more than 5 min N=30, 5 min or less N=40, and seizure free controls N=35)	PVS counts were lower (P<.001) in the SFS≤5min (445.80±66.10) and the control (430.77±182.55) than in SFS>5min (642.70

(*continued on next page*)

Table 10 (*continued*)

Study	Overview	PVS quantification method	MRI sequences	Sample N	Results
					±100.62). It was similar for PVS volume (SFS>5min, 8514.63 ±835.33mm3, SFS≤5min, 6390.43±692.74 mm3, control, 6048.37±111.50 mm3; P<.001). However, in the SFS≤5min, PVS measurements were lower than in the SFS>5min (P<.001). PVS measurements were positively correlated with seizure duration and inversely correlated with the course following seizure onset and MRI scan time in both SFS groups.
(Lysen et al., 2022)	Determine whether sleep is associated with perivascular spaces on brain magnetic resonance imaging (MRI).	(Dubost et al., 2019b)	T1w, T2w, T2*, FLAIR., 1.5T	Rotterdam Scan Study., N = 559	Actigraphy estimated sleep efficiency was associated with higher PVS load in the centrum semiovale; no associations of any other sleep characteristics with higher PVS load in the basal ganglia, hippocampus, or midbrain.
(Moses et al., 2022)	Investigate PVS as a marker of disease severity and neurodegeneration in patients with behavioural variant frontotemporal dementia (FTD), through the association between PVS burden and disease severity (given by cognitive composite score and CSF t-tau)	(Schwartz et al., 2019)	T1w, 3T	Possible/probable behavioural variant FTD patients N=12	Cognition total composite scores were associated with PVS burden (PVS cluster ß = −0.802e–3, p ≤ 0.001; PVS volume ß = −1.30e–3, p ≤ 0.001), as well as change in the cognition total composite score and the change in PVS volume (ß = 4.36e–3, p = 0.046) over 1 year. CSF t-tau was associated with number of PVS clusters (ß = 2.845, p = 0.036), and change in CSF t-tau and the change in the number of PVS (ß = 1.54, p < 0.001) and PVS volume (ß = 13.8, p = 0.003) over 1 year, change in NfL and the change in PVS volume (ß = 1.40, p = 0.045). Within the "non-progressor" group (n = 7), there was a significant relationship between the change in the CSF total-tau (t-tau) levels and the change in the PVS burden (PVS cluster (ß = 1.46, p = 0.014; PVS volume ß = 14.6, p = 0.032), and between change in NfL levels and change in the PVS burden over time (PVS cluster ß = 0.296, p ≤ 0.001; PVS volume ß = 3.67, p = 0.002).
(Perosa et al., 2022)	Investigation of histopathological correlates of PVS and relationship with vascular amyloid-B in cerebral amyloid angiopathy (CAA) using deep learning algorithm (3D Unet).	In-house method based on (Dubost et al., 2019b) and (Sepehrband et al., 2019)	*Ex-vivo* compared to *in-vivo*., T2w., 3T, 7T (N = 2)	Cerebral Amyloid Angiopathy., N = 24	MRI-visible PVS corresponded to enlarged spaces around blood vessels in WM on histopathology. Spaces contained cells and extracellular material. PVS burden positively associated with CAA severity (total CAA + myelin rarefaction = 52% of PVS variance). PVS large around WM portion of perforating cortical arteries affected by CAA. PVS in hereditary CAA comparable with sporadic CAA.
(Ramirez et al., 2022)	Exploration of association between small and large BG PVS, cognition, and motor/non-motor features in patients with Parkinson's Disease.	(Yushkevich et al., 2006)	T1w, T2w, FLAIR, PD., 3T	Parkinson's Disease., N = 13	In small BG-PVS group, significant association between BG-PVS counts and scores in MDS-UPDRS Part I [Daily non-motor symptoms] (p = .008) and Part II [Daily motor symptoms] (p = .024), but not Parts III and IV. Patients in large BG-PVS group had significant associations with BG-PVS counts and scores in MDS-UPDRS Part III (p < .0001) and Part IV (p = .001), but not Parts I

(*continued on next page*)

Table 10 (*continued*)

Study	Overview	PVS quantification method	MRI sequences	Sample N	Results
					and II. No significant correlation between BG-PVS count and MoCA score.
(Vikner et al., 2022)	Investigate 5-Year Associations among Cerebral Arterial Pulsatility, PVS Dilation, and White Matter Lesions in cognitively normal older individuals	(Boespflug et al., 2018; Schwartz et al., 2019)	T1w, T2w, FLAIR, 4D flow., 3T	Older adults., N = 178 baseline, N = 114 follow-up	White matter lesions and PVS predict increases in pulsatility index (PI), lacunes are unrelated to Pulsatility Index (PI). PVS intercept x ICA PI slope: R=0.23, $p = 0.025$; PVS intercept x Distal PI slope: R = 0.32, $p = .002$.
(Aribisala et al., 2023)	Explore the relationship between sleep quality, PVS and brain health markers in ageing	(Ballerini et al., 2016)	T2w, 1.5T	Community-dwelling older participants in the LBC1936 study (N=388)	High burden of PVS at age 73 (volume, count, and visual scores), was associated with faster deterioration in white matter: reduction of NAWM volume (β = −0.16, P = 0.012) and increasing white matter damage metric (β = 0.37, P < 0.001) between ages 73 and 79. On SEM, centrum semiovale PVS burden mediated 5% of the associations between sleep parameters and brain changes.
(Bown et al., 2023)	Explore relationship between baseline PVS burden and neuropsychological performance (cross-sectional and longitudinal) and aortic stiffness.	(Remedios et al., 2020)	T1w, 3T	Cognitively unimpaired (N=169), early MCI (N=27), MCI (N=131)	Higher aortic stiffness related to greater BG-PVS volume (β = 7.0 × 10−5, p = 0.04). Higher baseline PVS volume was associated with worse baseline information processing (β = -974, p = 0.003), executive function (β = -81.9, p < 0.001), and visuospatial performances (β = -192, p = 0.02) and worse longitudinal language (β = -54.9, p = 0.05), information processing (β = -147, p = 0.03), executive function (β = -10.9, p = 0.03), and episodic memory performances (β = -10.6, p = 0.02). Results were similar for PVS count.
(Butler et al., 2023)	Determine whether MRI-based measurements of glymphatics (DTI-ALPS and PVS volumes) differed between traumatic brain injury (TBI) and non-TBI subjects.	(Sepehrband et al., 2019)	T1w, T2w, 3T	TBI (N=37) and controls (N=13)	Manual x Automated: Correlation between PVS volume and manual PVS count (R = 0.901, P < 0.001) and visual score (R = 0.842, P < 0.001). PVS volumes and DTI-ALPS did not correlate (R=-0.108; P=0.46). No difference in PVS between TBI and controls (P=0.16). Perivascular space volume did not differ in subjects with traumatic brain injury as compared with controls and did not correlate with blood levels of neurofilament light chain, suggesting it may be a less sensitive measure for injury-related perivascular clearance changes.
(Charisis et al., 2023)	Assessment of risk factors and clinical importance of PVS by Whole-Brain Investigation in the Multi-Ethnic Study of Atherosclerosis	(Rashid et al., 2023)	T1w, T2w, FLAIR, 3T	Community-based subjects (N=1026) from the Multi-Ethnic Study of Atherosclerosis (MESA)	Manual x Automated Sensitivity = 82%; Precision = 83%. BG PVS volume was positively associated with age (β = 3.59 × 10−3), systolic blood pressure (β = 8.35 × 10−4), use of antihypertensives (β = 3.29 × 10−2), and negatively associated with Black race (β = −3.34 × 10−2). Thalamic PVS volume was positively associated with age (β = 5.57 × 10−4) and use of antihypertensives (β = 1.19 × 10−2). Insular region PVS volume was positively associated with age (β = 1.18 × 10−3). Brainstem PVS volume was smaller in Black

(*continued on next page*)

Table 10 (*continued*)

Study	Overview	PVS quantification method	MRI sequences	Sample N	Results
					than in White participants ($\beta = -5.34 \times 10-3$). Frontoparietal PVS volume was positively associated with systolic blood pressure ($\beta = 1.14 \times 10-4$) and negatively associated with age ($\beta = -3.38 \times 10-4$). Temporal region PVS volume was negatively associated with age ($\beta = -1.61 \times 10-2$), being Chinese American ($\beta = -2.35 \times 10-1$) and being Hispanic ($\beta = -1.73 \times 10-1$).
(Chen et al., 2024)	By assessing the glymphatic function in children with attention-deficit hyperactivity disorder (ADHD), aims to determine whether PVS differ between ADHD and typical developing children.	(Ballerini et al., 2018)	T1w, T2w, FLAIR, 3T	Pediatric ADHD (N=47), age- and gender-matched typical developing children (N=52)	PVS volume (mean, 15.514 mL vs. 11.702 mL) and PVS volume ratio in the ADHD group were larger than those in the TD group (all $p < 0.001$).
(Duperron et al., 2023)	Investigate GWAS associations of SVD markers. Only 2/18 cohorts applied a quantitative approach to score PVS burden automatically, which was later dichotomised on the top quartile for uniformity with the rest of the cohorts. Method of analysis: meta-regression.	(Dubost et al., 2019b)	T1w, T2w, 1.5T, 3T	N=31,700 participants from the UK Biobank and the Rotterdam Scan Study III (out from 40.095 from 18 population-based cohorts)	24 genome-wide significant PVS risk loci were associated with white matter PVS in young adults ($N = 1,748$; 22.1 ± 2.3 yr) and were enriched in early-onset leukodystrophy genes and genes expressed in foetal brain endothelial cells. Mendelian randomization supported causal associations of high blood pressure with BG and hippocampal PVS, and of BG PVS and hippocampal PVS with stroke, accounting for blood pressure.
(Evans et al., 2023)	Identify determinants of PVS burden in a pooled analysis of multiple cohort studies using one harmonized PVS rating method and automatic count.	(Dubost et al., 2019b)	T1w or T2w, 1.5T and/or 3T	Adults from 20 to 96 years old from various studies N=39,976	The average count of PVS in the 4 regions increased from the age 20 years (0–1 PVS) to 90 years (2–7 PVS). Men had more mesencephalic PVS (OR [95% CI] = 1.13 [1.08–1.18] compared with women), but less hippocampal PVS (0.82 [0.81–0.83]). Higher blood pressure, particularly diastolic pressure, was associated with more PVS in all regions (ORs between 1.04–1.05). Hippocampal PVS showed higher counts with higher high-density lipoprotein cholesterol levels (1.02 [1.01–1.02]), glucose levels (1.02 [1.01–1.03]), and APOE ε4-alleles (1.02 [1.01–1.04]). WMH volume and presence of lacunes were associated with PVS in multiple regions, but most strongly with the basal ganglia (1.13 [1.12–1.14] and 1.10 [1.09–1.12], respectively).
(Hicks et al., 2023)	Associations of PVS with brain lesions, brain age, sleep, and clinical outcomes in chronic Traumatic Brain Injury (TBI)	(Schwartz et al., 2019)	T1w, FLAIR, 3T	Patients with Traumatic Brain Injury (TBI) N=100, controls N=75	The TBI group had greater burden of PVS (prevalence ratio rate [PRR] = 1.29, $p = 0.013$). In TBI: the presence of bilateral lesions was associated with greater PVS burden (PRR = 1.41, $p = 0.021$), PVS burden was not associated with sleep quality, sleep duration, emotional distress or brain age. It was associated with verbal memory ($\beta = -0.42$, $p = 0.006$), but not with other cognitive domains.
(Jian et al., 2023)	Study the correlation between PVS and WMH in patients with a recent small subcortical infarct	(Wang et al., 2016b)	T1w, T2w, FLAIR, 3T	Patients with recent small subcortical infarct (RSSI) N=215	Patients with moderate-to-severe BG-PVS had higher DWMH and PWMH severity than those with mild BG-PVS, both in terms of volume and grade, but no significant difference in WMH

(*continued on next page*)

Table 10 (*continued*)

Study	Overview	PVS quantification method	MRI sequences	Sample N	Results
					severity between patients with mild vs. moderate-to-severe CSO-PVS. From multivariate analysis DWMH volume (β = 0.311; p = .002) and PWMH volume (β = 0.296; p = .004) were independently associated with BG-PVS. BG-PVS volume was correlated with PWMH volume (r = .589; p < .001) and DWMH volume (r = .596; p < .001).
(Karvelas et al., 2023)	Identify PVS correlates with other SVD features and cognition in CADASIL.	(Boespflug et al., 2018), and curvilinear filter from (Sato et al., 1998)	T1w, T2w, FLAIR, 3T	24 individuals with CADASIL and 24 age and sex matched controls (N=48)	CADASIL and control groups did not exhibit differences in mean PVS volumes. However, increased PVS volumes in CADASIL were associated with increased WMH volume (β=0.57, p=0.05), Clinical Dementia Rating (CDR) Sum-of-Boxes score (β=0.49, p=0.04), and decreased brain parenchymal fraction (BPF) (β=-0.03, p=0.10). Two central hub proteins were identified in protein networks associated with PVS volumes: CXCL8/IL-8, and CCL2/MCP-1.
(Kern et al., 2023)	Evaluate whether intensive systolic blood pressure (SBP) treatment affects PVS structure	(Sepehrband et al., 2019, 2021)	T1w, T2w, FLAIR, 3T	N=610 participants in Systolic PRessure INtervention Trial (SPRINT)	At baseline (N=610) greater PVS volume fraction was associated with older age, male sex, non-Black race, concurrent CVD, WMH, and brain atrophy. At follow-up (N=381) intensive treatment was associated with decreased PVS volume fraction relative to standard treatment (interaction coefficient: −0.029, p = 0.029). Reduced PVS volume fraction was also associated with exposure to calcium channel blockers (CCB).
(Kim et al., 2023a)	Explore the association of PVS burden with age	(Choi et al., 2020)	T1w, T2w, 3T	3 datasets from Human Connectome Project N=1789	Age was related to PVS volume in all regression models (R2 range, 0.41-0.55; P < .001). Age-PVS volume relationships were altered at the mid-30s and age 55 years; BG-PVS and WM-PVS volumes negatively correlated with age until the mid-30s (β, -1.2 and -7.8), then positively until age 55 years (β, 3.3 and 54.1) and beyond (β, 3.9 and 42.8; P < .001). The 90th percentile for PVS grades was grade 1 for age 49 years and younger, grade 2 for age 50-69 years, and grade 3 for age 70 years and older (overall, grade 2) for BG-PVS, and grade 3 for age 49 years and younger and grade 4 for age 50 years and older (overall, grade 3) for WM-PVS.
(Kim et al., 2023b)	Explore the association of PVS burden with age, sex and preterm birth	(Ballerini et al., 2018)	T1w, T2w, 3T	Human Connectome Project Neonates N=244	For BG PVSs, all neonates showed either grade 0 (90 of 244; 37%) or grade 1 (154 of 244; 63%), and for WM PVSs, most neonates showed grade 0 (227 of 244; 93%). Negative correlation of BG-PVS fraction with postmenstrual age at MRI (r = −0.008; P < .001). No evidence of sex differences for BG PVS volume (P = .07) or BG PVS fraction (P = .28). The BG PVS volume was smaller in preterm neonates than in term neonates (median, 45.3 mm3 vs 49.9, respectively; P = .04).

(*continued on next page*)

Table 10 (*continued*)

Study	Overview	PVS quantification method	MRI sequences	Sample N	Results
(Li et al., 2023)	Use deep learning U-shaped networks (U-Net) to explore the PVS distribution in Huntington's Disease (HD) patients and controls	(Boutinaud et al., 2021)	T1w, T2w, 7T	N=106: 49 healthy controls, 32 pre-HD individuals and 25 HD patients	Significantly increased BG-PVS in HD patients and in pre-HD individuals compared to controls. BG-PVS was closely related to cognitive decline and BG atrophy.
(Lynch et al., 2023)	Study the normative time course of PVS alterations with age through the characterization of the influence of age, sex and cognitive performance on PVS anatomical characteristics in a large cross-sectional cohort of healthy subjects across the lifespan.	(Sepehrband et al., 2019)	T1w, T2w, 3T	N=~1400 healthy volunteers ages 8-90	Age is associated with wider and more numerous MRI-visible PVS over the course of the lifetime with spatially-varying patterns of PVS enlargement trajectories. In particular, regions with low PVS volume fraction in childhood are associated with rapid age-related PVS enlargement (e.g., temporal regions), while regions with high PVS volume fraction in childhood are associated with minimal age-related PVS alterations (e.g., limbic regions). PVS burden was significantly elevated in males compared to females with differing morphological time courses with age.
(Park et al., 2023)	Study the relevance of PVS dilatation to normal aging across the lifespan by exploring changes in different characteristics of PVS dilatation across a wide range of age	(Choi et al., 2020)	T1w, T2w, 3T	N=1220 healthy subjects ages 18-100	PVS could be detected with a higher probability for older subjects than for younger subjects. For the random forests model that used 90 PVS features, RMSE in estimating the subjects' age was 9.53 ± 0.09 years, and the correlation between estimated age and actual age was 0.875 ± 0.003. The combined set of PVS burden and location features provided the best estimation performance.
(Sibilia et al., 2023)	Understand the potential interactions between PVS, cortisol, hypertension, and inflammation in the context of cognitive impairment	(Sepehrband et al., 2019), but only using T1w	T1w, 3T	ADNI-1 population with all biomarker info (N=465, age range=55-90). But final sample is N=456 after removing outliers from PVS segmentation	In the centrum semiovale, higher levels of inflammation reduced cortisol associations with PVS volume fraction. PVS were negatively associated with ACE only when interacting with TNFr2 (a transmembrane receptor of TNF). BG PVS were positively associated with TRAIL (a TNF receptor inducing apoptosis).
(Shih et al., 2023)	Analyze the relationship between sleep and the PVS in cognitively healthy adults across the aging continuum.	(Sepehrband et al., 2019)	T1w, T2w, 3T	N=725 cognitively healthy participants (36–100 years old) from the HCP-Aging Lifespan Release 2.0.	Older adults who had better sleep quality and sleep efficiency had larger BG-PVS volume fraction. However, sleep measures were not associated with CSO-PVS volume fraction. BMI influenced the BG-PVS across middle-aged and older participants. The effect of sleep quality on PVS volume fraction was mediated by BMI. There were significant differences in PVS volume fraction across racial/ethnic groups.
(Sotgiu et al., 2023)	Explore the associations between brain PVS and autism: clinical and pathogenic implications	(Sepehrband et al., 2019) but without filtering. Applies intensity thresholding	T1w, T2w, 1.5T	ASD patients N=65 and controls N=71	Higher WM-PVS associated with male sex (p=0.01), not significant correlation with ASD severity and younger age. PVS related with insomnia but not with epilepsy or IQ.
(Tachibana et al., 2024)	Determine the association between BP and PVS volumes and to examine the interactions of vascular risk factors, exercise, dementia diagnosis, MCI diagnosis, and presence of APOE e4 carrier.	In-house U-ResNet (4 convolutional filters downscaling and 4 upscaling)	T1w, 1.5T, 3T	N=9296 community dwelling subjects of age >=65	Mean PVS volumes increased with increase in systolic and diastolic BP levels (P for trend = .003, P for trend<.001, respectively), even after excluding subjects with dementia.
(Wang et al., 2023)	Investigate whether or not impaired glymphatic drainage underlying obstructive sleep apnea is associated with cognitive dysfunction	Intensity differences, detected in ImageJ	T1w, T2w, and DCE-MRI, 3T	Obstructive Sleep Apnea patients (N=28) and Controls (N=31)	The relative area ratios of PVS in the bilateral frontal cortex and the BG were significantly higher in the OSA group, and even more in the severe OSA group than in the mild-

(*continued on next page*)

Table 10 (*continued*)

Study	Overview	PVS quantification method	MRI sequences	Sample N	Results
					moderate OSA group, showing higher accuracy for distinguishing these groups.
(Yu et al., 2023)	Examine the association between SVD markers (including PVS) with higher ratios of soluble-epoxide hydrolase derived linoleic acid diols (12,13-dihydroxyoctadecenoic acid [DiHOME] and 9,10-DiHOME) to their parent epoxides (12(13)-epoxyoctadecenoic acid [EpOME] and 9(10)-EpOME) in stroke	(Ramirez et al., 2015)	T1w, T2w, FLAIR, PD, 3T	N=80 patients with small vessel stroke (N=50, age 70.3 (7.7), 34% female) or large vessel stroke (N=30, age 67.4 (6.3), 23% female)	Ratios of 12,13-DiHOME/12(13)-EpOME and 9,10-DiHOME/9(10)-EpOME were associated with greater volumes of WMH (β=0.364, P<0.001; β=0.362, P<0.001) and white matter MRI-visible PVS (β=0.302, P=0.011; β=0.314, P=0.006).
(Zebarth et al., 2023)	Explore the association between type 2 diabetes mellitus (T2DM) and hypertension with MRI-visible PVS	(Ramirez et al., 2015)	T1w, T2w, FLAIR, PD, 3T	81 participants diagnosed with T2DM and 395 without T2DM at baseline, and 70 participants diagnosed with T2DM and 346 without T2DM at 1 year follow-up.	Patients with T2DM had greater wmPVS volume and there were greater wmPVS volumes in patients with T2DM and hypertension together. Counterfactual moderated mediation models found indirect effects of T2DM on volumes of other SVD and diffusion markers that were mediated by wmPVS: pWMH, dWMH, periventricular lacunes, and deep lacunes, and progression of deep lacunes over 1 year, in patients with hypertension, but not in patients without hypertension.

Legend: PVS: Perivascular Spaces, F1+2: Prothrombin Fragment 1 + 2, TAT: Thrombin-Antithrombin III complex, HD: Huntington's Disease, vWF: von Willebrand's Factor, GM: Grey Matter, WM: White Matter, CVD: Cerebrovascular Disease, CAA: Cerebral Amyloid Angiopathy, TBI: Traumatic Brain Injury, CSVD: Cerebral Small Vessel Disease, PVSVF: Perivascular spaces volume fraction, AD: Alzheimer's Disease, MCI: Mild Cognitive Impairment, ADNI-2: Alzheimer's Disease Neuroimaging Initiative second recruitment wave, ASD: Autism Spectrum Disorder, RMSE: Root Mean Square Error, T2DM: Type 2 Diabetes Mellitus, wmPVS (or WM PVS): Perivascular Spaces in the White Matter.
Note: Choi et al. (2020) is a method development study as well as an application study. Therefore, it is included in both: Tables 7 and 10, with the relevant information for each analysis.3.5.2. Factors explored in relation to PVS burden

Table 11
Frequency of computational PVS applications in included studies.

Method	N applications	Principle of PVS assessment
(Ballerini et al., 2016, 2018)	12	Frangi Filtering + thresholding
(Boespflug et al., 2018; Schwartz et al., 2019)	2	Morphological detection + thresholding
(Boespflug et al., 2018; Sato et al., 1998)	1	Morphological detection + thresholding
(Boutinaud et al., 2021)	1	Deep learning (CNN)
(Choi et al., 2020)	4	Frangi filtering + Deep learning (CNN)
(Dubost et al., 2019a)	3	Deep learning (CNN)
In-house methods	7	varied
(Lian et al., 2018)	4	Deep learning (CNN)
(Ramirez et al., 2011, 2015)	4	Thresholding
(Ranti et al., 2022)	1	Frangi Filtering + thresholding
(Rashid et al., 2023)	1	Deep learning (CNN) + thresholding
(Remedios et al., 2020)	1	Deep learning (CNN) + thresholding
(Schwartz et al., 2019)	4	Morphological detection
(Sepehrband et al., 2019, 2021)	10	Frangi Filtering + thresholding
(Smith et al., 2020)	1	Frangi Filtering + thresholding
(Wang et al., 2016b)	3	Adaptive thresholding
(Yushkevich et al., 2006)	1	Texture analysis – active contours

30,000 (Duperron et al., 2023; Evans et al., 2023) and five with more than 1,000. Broad population type and age-groupings used in application studies compared to method development and improvement studies are presented in Tables 4 and 5, respectively.

3.5.5. *Application results*

Six areas of interest emerged in common across a number of application studies: age, sex, hypertension, diabetes, sleep, white matter hyperintensities (WMH), and cognition.

3.5.5.1. Age. Eleven studies reported a positive association between computational PVS measures and age (Aribisala et al., 2023; Barisano et al., 2021; Choi et al., 2020; Evans et al., 2023; Huang et al., 2021b; Kern et al., 2023; Park et al., 2023; Piantino et al., 2021; Ranti et al., 2021; Wang et al., 2016a; Zong et al., 2020), one of which was a study in young adults (mean age = 28.8 years). But studies on life-time trajectories point at varying patterns of these associations throughout the lifespan (Kim et al., 2023a; Lynch et al., 2023). One study of adolescents (N=118) found no association between age and PVS burden (Piantino et al., 2020), and neither another study on children (Sotgiu et al., 2023). A study on chronic traumatic brain injury did not find PVS burden being associated with brain age (Hicks et al., 2023). Studies that analysed the PVS association with age in different regions had conflicting results, with the majority reporting a positive association/correlation with age in all regions, and one study finding a negative association between age and PVS volume in the temporal region ((Charisis et al., 2023), N=1026).

3.5.5.2. Sex. Nine studies provided information on PVS burden aggregated by sex. Two found no association between PVS burden and sex (Kim et al., 2023a; Wang et al., 2016a), while the majority (i.e., six out

of nine) found PVS burden to be greater in males than in females (Barisano et al., 2021; Evans et al., 2023; Kern et al., 2023; Lynch et al., 2023; Piantino et al., 2020; Sotgiu et al., 2023). It is worth noting, however, that (Evans et al., 2023) performed a regional analysis and also reported no sex differences in the number of PVS in the hippocampus. Only one study involving cognitively normal and mild cognitive impaired individuals found higher CSO PVS fraction in females compared with males (Sepehrband et al., 2021) after adjusting for age and years of education. However, the same study reported CSO PVS fraction being higher in males in the cognitively normal group and no sex differences in CSO PVS fraction in the mild cognitively impaired group in absence of potential confounds.

3.5.5.3. Hypertension. Eleven out of thirteen studies identified a positive association between hypertension and PVS burden (Ballerini et al., 2020b; Charisis et al., 2023; Cheng et al., 2022; Duperron et al., 2023; Evans et al., 2023; Haddad et al., 2022; Huang et al., 2021b; Tachibana et al., 2024; Wang et al., 2021; Wang et al., 2016a; Zebarth et al., 2023). Duperron et al. (2023), the largest study amongst the ones included, found causal associations of high blood pressure with BG and hippocampal PVS, and of BG PVS and hippocampal PVS with stroke, accounting for blood pressure, even after Mendelian randomisation. In Wang et al. (2021), basal ganglia PVS count was associated with hypertension, but not PVS volume. Piantino et al. (2021) found no association between systolic or diastolic blood pressure and PVS burden, and Choi et al. (2020) did not find blood pressure to be associated with PVS volumes.

3.5.5.4. Diabetes. No association between PVS burden and diabetes was found in two studies (Ballerini et al., 2020b; Wang et al., 2016a), but a positive association was identified in a third study between white matter PVS burden and diabetes (Wang et al., 2021), and in another study exploring specifically the putative role of PVS burden in type 2 diabetes mellitus (T2DM) (Zebarth et al., 2023). This study also found that indirect effects of T2DM on volumes of other SVD markers (i.e., WMH and lacunes) were mediated by the PVS burden in the white matter.

3.5.5.5. Sleep. The relationship between sleep and PVS burden was explored in nine studies (Aribisala et al., 2023; Berezuk et al., 2015; Hicks et al., 2023; Lysen et al., 2022; Barisano et al., 2021; Piantino et al., 2021; Shih et al., 2023; Sotgiu et al., 2023; Wang et al., 2023), with all except two (Barisano et al., 2021; Hicks et al., 2023) identifying an association between at least one metric of sleep and PVS burden. Berezuk et al. (2015) and Lysen et al. (2022) reported a negative correlation between both sleep efficiency and PVS burden. Berezuk et al. (2015) further reported a negative association between the duration of N3 (i.e., deep sleep) and PVS burden, and a positive association between wakefulness after sleep onset (i.e., number of interruptions to sleep) and BG-PVS burden. But Lysen et al. (2022) found no associations between any other metric of sleep and PVS burden in any location. In a very heterogeneous sample (Shih et al., 2023) found that older adults who had better sleep quality and sleep efficiency had larger BG-PVS volume fraction, while CSO-PVS volume fraction was not associated with sleep measures. But this study also found that the effect of sleep quality on PVS volume fraction was mediated by BMI, and that there were significant differences in PVS volume fraction across racial/ethnic groups. Piantino et al. (2021) reported a significant association between poor sleep and PVS volume, with PVS volume greater in those with poor sleep and mild traumatic brain injury (TBI) than those with good sleep and mild TBI. Aribisala et al. (2023) found that CSO-PVS volume mediated 5% of the associations found between sleep parameters and brain structural changes. Sotgiu et al. (2023) reported that white matter PVS were related with insomnia in autistic children, and Wang et al. (2023) found that PVS volume ratios were associated with obstructive sleep apnoea (OSA), showing higher accuracy for distinguishing groups of patients with different degrees (i.e., severity) of OSA.

3.5.5.6. White matter hyperintensities. Nine studies reported positive associations between PVS burden and WMH volumes (Aribisala et al., 2023; Ballerini et al., 2020b; Barnes et al., 2022; Evans et al., 2023; Huang et al., 2021a; Jian et al., 2023; Karvelas et al., 2023; Kern et al., 2023), with the latter finding the association only for PVS in the BG and not in the CSO. Two of them found also topological relationships between the occurrence of PVS and the location of WMH deep clusters (Barnes et al., 2022; Huang et al., 2021a). A study in chronic TBI (Hicks et al., 2023) reported a positive association between PVS burden, given as prevalent ratio rate, and bilateral lesions. However, it is unclear if the lesions referred are only as a consequence of the injuries or including also WMH.

3.5.5.7. Cognition. Fifteen studies explored the relationship between cognition and PVS with results varying depending on the characteristics of the cohorts and the cognitive domains assessed. Hicks et al. (2023), for example, reported PVS burden impacting verbal memory but not any other cognitive domain. Two studies found no direct or significant association between general cognition (general cognitive ability, Montreal Cognitive Assessment score) and PVS burden (Ramirez et al., 2022; Valdés Hernández et al., 2020). (Valdés Hernández et al., 2019) reported PVS burden as predictive of reduced fluid intelligence in Huntington's disease patients but not in family members without overt disease, while Sotgiu et al. (2023) did not find association between PVS burden and IQ in autistic children In mild cognitive impaired (MCI) and dementia, all studies reported different measures of PVS being more relevant in MCI (Bown et al., 2023; Sepehrband et al., 2021) and frontotemporal dementia (Moses et al., 2022) groups than in controls. Jokinen et al. (2020) reported PVS volume to be a significant predictor of processing speed, decline in processing speed, decline in memory, and of total vascular dementia assessment (VADAS-cog) score. PVS burden was related to poor cognition in CADASIL (Karvelas et al., 2023), and in Huntington's disease (Li et al., 2023; Valdés Hernández et al., 2019). Kamagata et al. (2022) reported higher PVS volume fraction (total, in basal ganglia, and white matter) in Alzheimer's disease (AD) patients compared to controls, and higher white matter PVS volume fraction in the mild cognitive impaired (MCI) group compared to controls. Hamilton et al. (2021a), Hamilton et al. (2021b) reported that worse total SVD burden (PVS-inclusive) was associated with cognitive decline, but did not report PVS-specific results.

3.6. Risk of bias assessments

Risk of bias assessments were conducted based on the QUADAS-2 framework, with potential sources of bias assessed including: patient selection, index method bias (i.e., does the method used to quantify PVS introduce bias), reference accuracy (i.e., accuracy of ground truth), reference blind to index (i.e., was PVS quantification influenced by prior knowledge of ground truth), same reference for all, inclusion of all participants, method/application matches review question, applicability, and overall assessment. Applicability refers to the plausibility of the methods or study analyses of being applied widely in different scenarios (i.e., imaging protocols, presence of noise, field strengths, scanner types and configurations, manufacturers, and datasets of patients with different clinical characteristics), as well as to the completeness in the description of the method or study design, which allows it to be reproducible, and, therefore applicable more widely (i.e., generalizable).

3.6.1. Method and improvement

Due to the small number of 'improvement' studies, these were grouped with 'method development' studies in the presentation of risk of bias assessments. In general, 42.31% of method and improvement studies were rated as low risk of bias, 17.31% were rated as instilling

some bias concerns, and 40.38% had high risk of bias. One study did not provide enough detail for a bias assessment. The individual domain with the most frequent high risk of bias scoring was 'applicability' (how well the index measure (e.g., method) can be applied to PVS quantification more widely (i.e., in other scenarios, datasets) in the context of the review question). Reasons provided when rating applicability as having a high risk of bias included a lack of detail in the methodology, lack of validation testing, and no ability to discriminate between PVS and other lesion types. A summary risk of bias plot for method and improvement studies is shown in Fig. 6.

3.6.2. Application

There was low risk of bias in 59.32% of application studies, some risk in 25.42%, and high risk in 15,25%. The domain most frequently scoring as having a high risk of bias was 'includes all participants', rated high risk in 49.15% of application studies. Often, a small number of patients were excluded from application studies due to poor image quality (noise and motion artefacts) which compromised PVS quantification performance, without a statistical analysis of the relevance of missing values as a consequence. A summary risk of bias plot for application studies is provided in Fig. 7.

4. Discussion

4.1. Overview

We conducted a systematic review of the development, improvement, and application of computational PVS quantification approaches, including studies published up to September 2023. We explored 67 approaches involving 48 methods presented as part of 45 publications, eight frameworks or suggestions for improving some of these methods, nine in-house pipelines or methodologies using different elements or combinations from some of the computational approaches presented, and two re-purposed implementations from approaches developed for other purposes, these applied to clinical research. We collated information on the main aims and outcomes of each study, and extracted and analysed data relating to MR imaging sequences and field strengths used, population types and sample sizes, method characteristics including training and validation, and results.

The number of studies developing or using computational PVS quantification approaches has increased steadily since the first identified study of this type in 2002 Kruggel et al. (2002) reaching a peak of 8 computational PVS assessment methods published in 2019, the year from which the number of studies applying these methods has been experiencing an exponential growth. Currently, research into PVS using quantification approaches comprises a large field, favoured by the increase in the ability to analyse large datasets for which visual scores are lacking, and the increased interest in the function and relevance of PVS in brain health.

The use of a morphological filter to enhance PVS-like structures, with Frangi being the most commonly used, and the use of a U-Net configuration with or without residual connexions, were the two most widely applied and promising approaches, which have been independently validated. The commonest PVS feature (s) that are measured are volume and count, obtained from the PVS segmentations. From them, PVS volume, absolute, or as a percentage in the region of interest, appears to be the most consistent PVS parameter used by the clinical studies that applied a computational approach to assess PVS. Individual PVS morphology (i.e., length, width, tortuosity, sphericity) are generally calculated using ellipsoid, tubular or skeletonisation approaches, but drawbacks of these conventional methods have been recently exposed and challenged by the use of Bèzier curves (Duarte-Coello et al., 2023).

Imaging data from older adults, or a wide age range of adults, has most frequently been used in both the development and application of computational PVS quantification approaches, consistent with studies using non-computational approaches to PVS quantification (Francis et al., 2019). MR imaging was most often obtained from 1.5T and 3T imaging, with a recent increase in the use of 7T imaging. T2w imaging was most commonly used across all study types, often in combination with T1w and FLAIR imaging, these mainly being used as part of the frameworks developed for eliminating confounds and generating regions of interest, although a number of application studies used T1w only for assessing the PVS. It has been noted, however, that vessel calcifications, also hypointense in T1w images, can confound the accuracy of PVS identification, and, therefore, segmentation, if only T1w images are used (Valdés Hernández et al., 2024), falsely inflating the number of PVS detected. We limited the scope of the present review to static, structural imaging of PVS, as opposed to including fluid dynamics, functional imaging, and/or cerebrovascular reactivity studies which may make greater use of alternative imaging modalities, including diffusion tensor imaging, 4D-flow, positron emission tomography (PET), single-photon emission computed tomography (SPECT). The contribution of each MR sequence contrast and their combinations to the detection of PVS is still unclear and deserves further study. Meantime, application studies using PVS quantification methods should be aware of the differences in MRI sequences' sensitivities and their combinations, when drawing conclusions on the effect of PVS burden in relation to clinical and demographic variables.

Special attention should be given at the differences in the PVS detectability at different magnetic field strengths (i.e., 1.5T vs. 3T vs. 7T). This, together with the spatial resolution in terms of voxel sizes, greatly influence the PVS quantification results. Assuming a perfectly calibrated and error-free quantification method, images obtained at 7T are expected to show more PVS than those obtained at 1.5T without this necessarily meaning that the brains scanned at these two different magnetic field strengths have different burden of PVS. Equally, quantification methods can be susceptible to partial volume effects due to different voxel sizes (Duarte-Coello et al., 2024). Therefore, it will be advisable for application studies using PVS quantification methods and images acquired from multiple scanners and imaging protocols, to

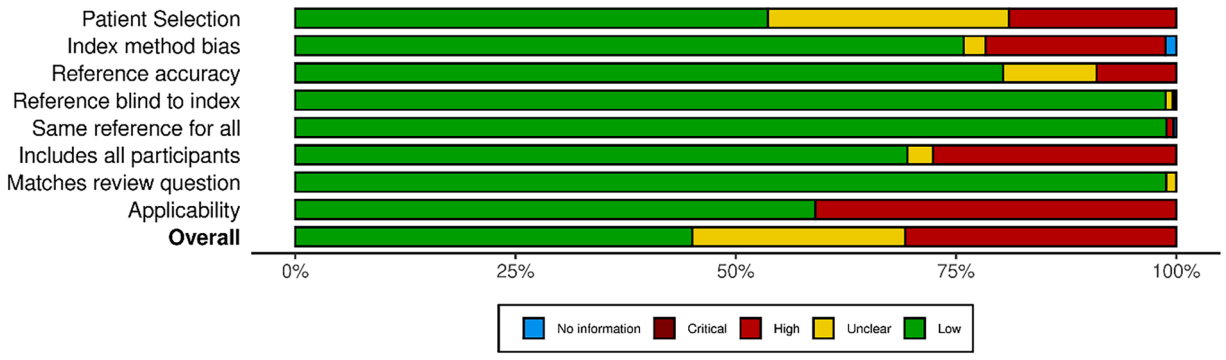

Fig. 6. Risk-of-bias summary plot for method development and improvement studies.

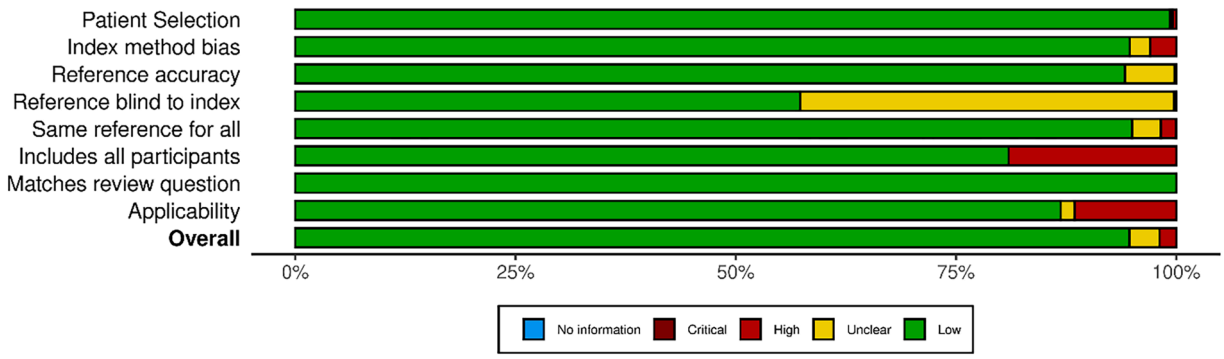

Fig. 7. Risk-of-bias summary plot for application studies.

divide the clinical sample by MRI protocol/magnetic field strength, separately tune the preferred PVS quantification method to the specific image subset, perform the analyses separately, and, finally, meta-analyse the results.

4.2. Method development studies

The most common approaches to computational PVS quantification were thresholding, thresholding and filtering, and deep learning (CNN) methods. Deep learning approaches have become almost ubiquitous since 2017, with 19 of the 48 method development studies using CNN methodology. They have higher processing speed and capacity than the more conventional methods, and a single architecture can be designed and trained to separately assess different confounding features, e.g., lacunes, PVS, and WMH. But the large number of parameters that CNN architectures manage and need to adjust require a breath of size and variability in the training dataset impossible to achieve at present. Then, as the resultant model is overfitted to the imaging parameters and clinical presentations of the dataset used for training, these models would need to be re-trained for every different cohort at hand. This entitles a reasonable number of ground truth manual segmentations, not always feasible and highly observer-dependant. While some of the architectures reviewed here have been made publicly available, we could not find any pre-trained CNN model to independently test the accuracy levels reported in their original publications. The conventional approaches that threshold the output from a morphological filter that enhances PVS-like structures, on the other hand, do not require large amount of data to be tuned, but still the threshold and some parameters would need to be adjusted depending on the imaging protocol and image quality. Also, separate developments would be required to remove confounding pathology and deal with artefacts. In terms of reproducibility, sustainability, and applicability, both types of approaches, being fully automatic, could reach high levels, but these would depend, for now, on the skills of the computer programmers that generate and manipulate them, and data availability.

Computational segmentation pipelines used different pre-processing steps. General steps involved co-registration of the different MRI sequences to the one in which PVS are assessed, and intensity normalisation. No justification of the intensity normalisation approach has been given or evaluated in any of the studies. A study classed as improvement (Valdés Hernández et al., 2024a) only evaluates the impact of the point, within the pipeline, in which a linear intensity normalisation is done. Evaluation of the impact of the type of intensity normalisation in the results is currently lacking. Few methods perform bias field correction. But the similarity indices and performance metric of all the methods presented is similar, raising questions about the impact bias field correction may have in the overall performance of the method. Few methods involve denoising too, which, contrary to the correction of inhomogeneities in the b1 magnetic field aimed at filtering out the low-frequencies, is designed to remove the high-frequencies in the image. But given the nature of the task, the application of a band-pass filter in the preprocessing stage may not be the best option to consider. Another preprocessing step worth mentioning is the generation of regions of interest (ROIs), mostly carried out using freesurfer. In some other cases, ROIs are the grey and white matter tissue classes. Given the importance of this step, its validation in different scenarios would have been required. For example, in the presence of narrow ventricles with disconnected horns resembling tubular structures, and in the presence of calcified vessels resembling tubular structures that are also hypointense in T1w images, to mention just two of the most common scenarios (Valdés Hernández et al., 2024a).

Computational PVS quantification approaches were validated against a range of reference standards; most often visual rating scores (27.08% of studies), although there was a relatively high proportion (22.92%) of them which used manual segmentations as a reference standard. While visual rating scores may be less time consuming and applicable to much larger sample sizes than producing manual segmentation data, high correlation between segmentation results and visual scores does not necessarily mean that the segmentations are good. González-Castro et al. (2017) showed that neuroradiological assessments can be subconsciously influenced by the degree of the overall disease present. Therefore, it is likely that, for example, visual rating scores of PVS in the basal ganglia in patients with SVD would be highly correlated with PVS segmentations, but perhaps not so in the basal ganglia of obstructive sleep apnoea patients that would not necessarily have any other confounding imaging feature in their brain scans. Further exploration of the correlation between different computational parameters with visual scores in cohorts with different characteristics is needed. Manual segmentations, on the other hand, enable comparison of more PVS metrics (e.g., volume, width, length) than visual-only assessments, but they have been only available for a limited number of scans or for one slice per region per scan, and most of the studies lack reports of inter-annotator reliability assessment of the manual annotations used.

Not all of the method development studies provided information on the performance or validation of their method, with three studies not using any reference standard of ground truth. Performance metrics used in those that did report results varied, although more common measures included correlations between computational and non-computationally derived PVS values, number of false positives/false negatives, and spatial similarity (Dice coefficient). It is important to note that method development studies reporting the strongest validation results between computational and manual/visual PVS quantification often had either small sample sizes or a significant user-intervention aspect to their methodology in their validation datasets. For example, Wuerfel et al. (2008) reported an intraclass correlation coefficient of 1 (a perfect score), but data from only 4 participants were used, and Ranti et al. (2022) report a DSC score of 0.99 (almost perfect spatial overlap) but their method includes a final ‘manual correction’ stage. It is also worth noting that differences in MRI sequences, field strengths and voxel sizes

can directly impact the performance of the algorithms and, therefore, the common metrics used to evaluate them (e.g., Dice coefficient) if images acquired at various field strengths are jointly used.

A large proportion of method development studies lacked sufficient information with regards to parameters to be adjusted in methods using filtering and thresholding approaches, differentiation between PVS and other lesions (notably lacunes, which can have similar appearance), or applicability (and adjustments required) when using multi-site or multi-modality imaging. Some studies provided little to no information about MR equipment and sequences used including critical factors like voxel size and slice thickness, nor about the population from which imaging data were derived or the process of participant selection. This is reflected in the large number of studies rated as having a high risk of bias for applicability. Deep learning is able to deal with changes in voxel size and slice thickness as long as the model has been trained with such a data. The vanilla implementation of the Frangi filter, for example, is also not able to deal with anisotropic data while the implementation of the Jerman filter in Matlab is. This information, therefore, impacts in the subsequent number of applications using the methods developed.

Given the varied approaches to assessing and reporting performance of novel PVS quantification methods, it may be beneficial to work towards a standard for validation and reporting. For example, a dedicated open-source PVS quantification validation dataset/repository would be worthwhile, with representative PVS and SVD, image sequence, image quality, and multi-site imaging, and phantom data. This would enable validation of novel methods by developers themselves and reproducibility assessments from outside parties. It is worth noting that although most method developments have used data acquired at the commonly used field strengths and from relevant populations – e.g., older individuals who are therefore likely to have bigger or more visible PVS, some atrophy, and confounding pathologies like WMH –, this does not imply that they would yield successful results if applied without variations, to MRI data from more, less, or simply different disease and age populations, even if acquired in the same scanners. It may also be of benefit to identify minimum reporting standards for validation performance, such as agreement on a preferred reference standard, minimum required validation sample size, and relationship, accuracy, and spatial overlap metrics.

4.3. Improvement studies

We identified eight studies concerned with improving computational PVS quantification. Targets for improvement included maintaining PVS detectability with image compression (Paz et al., 2009), reducing noise and motion artefacts (Bernal et al., 2020, 2021, 2022; Valdés Hernández et al., 2024a; Zong et al., 2021), comparing filtering approaches when applied to synthetic data (Bernal et al., 2022; Duarte Coello et al., 2024), works on physical and *in-silico* phantoms for establishing the limits of validity of PVS assessment methods (Duarte Coello et al., 2024), comparing PVS segmentations from T1w vs. T2w (Valdés Hernández et al., 2024a), drawing recommendations for threshold selection (Valdés Hernández et al., 2024a), tuning of filter parameters (Duarte Coello et al., 2024; Valdés Hernández et al., 2024a), and improving the calculation of PVS morphometrics (i.e., width and length) (Duarte Coello et al., 2023). While compression, noise, and motion artefacts appeared to have viable proposed solutions, one study identified remaining issues with differentiation between PVS and other hyperintense (in T2w) features, finding none of the more commonly used filter methods (Frangi, Jerman, RORPO) were effective at differentiating lesion types. This review has identified two ways in which methods have approached this issue: 1) by excluding WMH from the PVS ROIs, and 2) by combining multiple sequences simultaneously (e.g., Boespflug et al. (2018)), identify as PVS the voxels with CSF-like intensities in T1w, T2w, FLAIR and PD, while Sepehrband et al. (2019) segment on the combination of T1w and T2w and look for the intensity profile in FLAIR excluding the voxels on the top 10 percentile of the FLAIR signal distribution). But both approaches have drawbacks. The first one does not account for PVS inside WMH, consequently reporting few PVS in patients with wide and confluent WMH, just because the "clean" ROIs were small. The second one could also lead to erroneous results depending on the sensitivities of the MRI sequences involved, especially in the presence of thick slices and inter-slice gaps. Distinguishing between PVS and other hyperintense lesions remains an important target for improvement in computational PVS quantification.

4.4. Application studies

The three most frequently applied computational PVS quantification approaches identified in this review were the one firstly proposed by Ballerini et al. (2016) and implemented as part of different frameworks (24 applications), those derived from the work of Lian et al. (2018) (10 applications), and morphological detection as proposed by Schwartz et al. (2019) (6 applications). Ballerini et al. (2016) approach involved a Frangi filter approach with thresholding optimised based on visual PVS scores. Lian et al. (2018) approach was a deep learning (CNN) method, involving image enhancement and denoising stages prior to deploying a fully-automated CNN, trained on manually segmented PVS data. Schwartz et al. (2019) segmented PVS using a stepwise local homogeneity search of a white matter-masked T1w image, with FLAIR hyperintensity constraints and further linearity, width, and volume constraints. While these three approaches are the most frequently implemented, this is driven by the research groups in which the methods were developed, rather than an indication of a consensus on which PVS quantification approach to use based on methods' technicalities.

Factors identified in common among application studies included age, sex, hypertension, diabetes, WMH, sleep, and cognition, although comparable results were only available for a modest number of studies per factor. Other factors, like ethnicity, are starting to emerge, with two studies (Charisis et al., 2023; Shih et al., 2023) reporting differences in the spatial distribution (Charisis et al., 2023) and volume fraction (Shih et al., 2023) of PVS across racial/ethnic groups. Computational PVS measures used varied, but commonly included PVS count and volume, often segregated by region (e.g., basal ganglia PVS, centrum semiovale/white matter PVS). Increased age, hypertension, WMH, and sleep parameters were broadly associated with computational PVS metrics, although the only one that consistently (i.e., in all the nine studies that explored it) showed an association (in this case positive) with PVS burden was WMH either total volume or visual scores. This was followed by hypertension, with eleven out of twelve studies identifying a positive association between hypertension and PVS burden. The associations between age and PVS burden and hypertension and PVS burden have been previously documented in the literature, and been identified in non-computational studies (Francis et al., 2019). However, this review, different from previous reviews, as includes recent and large population studies involving adults from the whole lifespan or children and adolescents, points at the existence of various patterns of associations and correlations between age and PVS burden, with no association (Piantino et al., 2020; Sotgiu et al., 2023) or even negative associations in some brain regions (Lynch et al., 2023) in early life, a negative correlation until the mid-30s (Kim et al., 2023a), and a positive association/correlation afterwards with different strength degrees (Kim et al., 2023a). Other equally large population studies covering a large lifespan point to some factors that may relate to these findings. For example, (Shih et al., 2023) report that body mass index (BMI) influenced the basal ganglia PVS burden across middle-aged and older participants. A large GWAS study (Duperron et al., 2023) investigating the associations of small vessel disease markers found that 24 genome-wide significant PVS risk loci were associated with white matter PVS only in young adults, suggesting a genetically linked effect of age in PVS burden. In relation to sleep, the eight studies that explored its association with PVS evaluated different parameters: sleep efficiency, interruptions, quality, duration, falling asleep at different times during the day, for just mentioning some.

But all results suggest a positive association between PVS burden and poor sleep health. The dimension of the relationship between sleep and PVS (e.g., in clinical populations with different characteristics) has been less extensively explored, and may be a good candidate for further research.

Associations between sex and PVS burden were mixed, with two studies out of nine finding no association (Kim et al., 2023b; Wang et al., 2016a), one reporting that PVS burden was higher in females (Sepehrband et al., 2021), and six reporting that PVS burden was higher in males. These findings reflect the broader literature, which often has not reported on sex differences, or reports that potential sex differences in PVS burden remain unclear. Similarly, mixed results were identified for associations between PVS burden and diabetes. Of the four studies that referred to diabetes, two found no association (Ballerini et al., 2020c; Wang et al., 2016a) and two found a positive association between diabetes and white matter PVS (Wang et al., 2021; Zebarth et al., 2023). A previous systematic review and meta-analysis reported no associations identified between diabetes and PVS burden (Francis et al., 2019), but studies reporting on diabetes in relation to PVS burden are too few to draw any substantial conclusions as of yet.

PVS burden has been explored in association with cognition in a number of studies. In the present review, we found studies reported mixed evidence for poorer performance on cognitive testing in those with greater PVS burden. Two of the fifteen studies identified that examined cognition relied on a measure of total SVD burden, rather than PVS-specific associations. Both reported negative associations between SVD burden and cognitive decline (particularly decline in processing speed; (Hamilton et al., 2021a; Hamilton et al., 2021b)). From the rest, three studies reported no association between PVS burden and measures of cognition (Ramirez et al., 2022; Sotgiu et al., 2023; Valdés Hernández et al., 2020), and nine indicated a positive association between poor cognition, at least in one domain, and PVS burden. But those indicating a positive association studied specific clinical populations for which cognitive impairment was one of their phenotypes: Huntington's disease (Li et al., 2023; Valdés Hernández et al., 2019), CADASIL (Karvelas et al., 2023), TBI (Hicks et al., 2023), MCI (Bown et al., 2023; Kamagata et al., 2022; Sepehrband et al., 2021), frontotemporal dementia (Moses et al., 2022), and AD (Kamagata et al., 2022). One study involving elderly patients aged 65-84 enrolled in the LADIS study (Pantoni et al., 2004), also reported a positive association between PVS burden and cognition. But all participants in this study had mild cognitive complaints, motor disturbances, minor cerebrovascular events, mood disturbances, and/or other neurological problems (Jokinen et al., 2020). Other systematic reviews and meta-analyses in recent years have also yielded mixed results as to the association between PVS and cognition (Francis et al., 2019; Hilal et al., 2018; Jie et al., 2020), with further research required to shed a light on the role of PVS by stage in cognitive decline, since PVS could increase or decrease depending on compensatory mechanisms, or as part of possibly a neuroprotective or coping mechanism, prior to or amidst continual decline in cognitive functions.

4.5. Strengths and limitations

The systematic nature of this review, the broad search terminology and inclusion criteria, and the large number of years covered (i.e., up until September 2023), are perhaps the main strengths of this work. Although there would have been sources missed due to database indexing issues, articles not being published in English language, or access restrictions, the systematic and inclusive nature of our work have allowed us to cover most of the literature on the theme published up to this date, distil, and make available data to inform future research in the field of PVS research. We have summarised and meta-analysed the characteristics, advantages, scope, applicability, and shortcomings of the computational methods developed up to date to assess PVS burden. This work has also covered the works to support the improvement of these methods, establish their limits of validity, and facilitate their use by explaining the effect of tuning their different parameters and drafting recommendations based on the evaluation of the most widely used methods in different settings. But this review covers only findings from computationally-derived measurements. Owed by the availability of databases with imaging and associated neuroradiological assessments and clinical data, still a considerable number of studies use visual scores in their analyses. For illustration, from January to September 2023 alone, our search in Web of Science identified 47 publications of clinical studies with PVS either as outcome measure or as predictor (at least one of them in some cases) that used PVS visual scores, which were excluded from our analyses, against only 23 studies that used computationally-derived metrics and were, therefore, included. Consequently, conclusions cannot be drawn from our findings on factors related to PVS burden as they only reflect results from a percentage of all the studies in this area of research. A wider literature analysis including also data obtained from neuroradiological (i.e., visual) assessments would be necessary to better inform on the associations of PVS with clinical, demographic, genetic, cognitive, and lifestyle factors.

4.6. Conclusions and future directions

Computational approaches to PVS quantification have increased in prevalence in recent years. Novel automated PVS quantification approaches often use thresholding and filtering approaches, or deep learning (CNN) approaches, each with different advantages as well as shortcomings. The method to use will, ultimately, depend on resources availability (i.e., ground truth, disposal or not of a pre-trained model, computational capacity, and skills of the researchers/image analysts). Barriers to successful computational PVS quantification, including image compression, image quality, and nature and quality of the reference standard assessments have been identified, and potential solutions have been proposed. In particular, further work is needed to address the issue of lesion type discrimination (e.g., PVS differentiation from lacunes and small WMH in T2w contrast images, and calcified vessels or mineralisation around small arterioles in T1w contrast images). Although some methods were developed using images from different scanners and magnetic field strengths, methods' performance in the same population imaged at different magnetic field strengths are not known. Best practices and adjustments for assessing longitudinal changes in PVS are also not documented. Also, most methods were developed using representative samples with wide range of PVS and confounding disease burden, but results were not analysed taking these into account. Further studies that develop methods for quantifying disease markers should analyse accuracy results by disease load in order to inform better the scope of their applicability. Computational PVS approaches are increasingly being applied in epidemiological and clinical studies, with age, WMH, hypertension, different diseases involving cognitive deficits as part of their phenotypes, and sleep, emerging as factors associated with PVS burden. More research is needed to better understand the mechanisms and mediating factors in the associations that have been consistently found, and the reasons for discrepancies in the factors that have yielded conflicting results across the studies.

Funding

This study is mainly funded by the Hilary and Galen Weston Foundation under the Novel Biomarkers 2019 scheme (ref UB190097) administered by the Weston Brain Institute. This study received also funds from the Fondation Leducq Network of Excellence for the Study of Perivascular Spaces in Small Vessel Disease (16 CVD 05); the Row Fogo Charitable Trust (MCVH, FC, JMW) (BRO-D.FID3668413); Dementias Platform UK 2, which receives funds from the UK Medical Research Council (MR/T033371/1); and the UK Dementia Research Institute at the University of Edinburgh (award number UK DRI-4002) through UK DRI Ltd, principally funded by the UK Medical Research Council, and additional funding partner the British Heart Foundation (JMW, JMJW).

CRediT authorship contribution statement

Jennifer M.J. Waymont: Writing – original draft, Methodology, Investigation, Formal analysis, Data curation, Conceptualization. **Maria del C. Valdés Hernández:** Writing – original draft, Visualization, Validation, Supervision, Project administration, Methodology, Investigation, Formal analysis, Data curation, Conceptualization. **José Bernal:** Writing – review & editing, Methodology, Validation, Investigation, Formal analysis, Data curation. **Roberto Duarte Coello:** Writing – review & editing, Validation, Formal analysis, Data curation. **Rosalind Brown:** Writing – review & editing, Project administration, Formal analysis, Data curation. **Francesca M. Chappell:** Writing – review & editing, Validation, Supervision, Methodology, Data curation. **Lucia Ballerini:** Writing – review & editing, Validation, Investigation, Formal analysis, Data curation. **Joanna M. Wardlaw:** Writing – review & editing, Validation, Supervision, Project administration, Methodology, Funding acquisition, Conceptualization.

Declaration of competing interest

The authors do not have any other competing interests to declare.

Data availability

The data is provided in the submission.

Supplementary materials

Supplementary material associated with this article can be found, in the online version, at doi:10.1016/j.neuroimage.2024.120685.

References

Aribisala, B.S., Valdés Hernández, M.D.C., Okely, J.A., Cox, S.R., Ballerini, L., Dickie, D. A., Wiseman, S.J., Riha, R.L., Muñoz Maniega, S., Radakovic, R., Taylor, A., Pattie, A., Corley, J., Redmond, P., Bastin, M.E., Deary, I., Wardlaw, J.M., 2023. Sleep quality, perivascular spaces and brain health markers in ageing–a longitudinal study in the Lothian Birth Cohort 1936. Sleep Med. 106, 123–131. https://doi.org/10.1016/J.SLEEP.2023.03.016.

Ballerini, L., Booth, T., Valdés Hernández, M.D.C., Wiseman, S., Lovreglio, R., Muñoz Maniega, S., Morris, Z., Pattie, A., Corley, J., Gow, A., Bastin, M.E., Deary, I.J., Wardlaw, J., 2020b. Computational quantification of brain perivascular space morphologies: associations with vascular risk factors and white matter hyperintensities. A study in the Lothian Birth Cohort 1936. NeuroImage Clin. 25, 102120 https://doi.org/10.1016/J.NICL.2019.102120.

Ballerini, L., Fetit, A.E., Wunderlich, S., Lovreglio, R., McGrory, S., Valdes-Hernandez, M., MacGillivray, T., Doubal, F., Deary, I.J., Wardlaw, J., Trucco, E., 2020a. Retinal biomarkers discovery for cerebral small vessel disease in an older population. In B. W. Papież, A. I. L. Namburete, M. Yaqub, & J. A. Noble (Eds.). Medical Image Understanding and Analysis. Springer International Publishing, pp. 400–409. https://doi.org/10.1007/978-3-030-52791-4_31.

Ballerini, L., Lovreglio, R., Hernández, M.D.C.V., Gonzalez-Castro, V., Maniega, S.M., Pellegrini, E., Bastin, M.E., Deary, I.J., Wardlaw, J.M., 2016. Application of the ordered logit model to optimising frangi filter parameters for segmentation of perivascular spaces. Procedia Comput. Sci. 90, 61–67. https://doi.org/10.1016/J.PROCS.2016.07.011.

Ballerini, L., Lovreglio, R., Valdés Hernández, M.D.C., Ramirez, J., MacIntosh, B.J., Black, S.E., Wardlaw, J.M., 2018. Perivascular spaces segmentation in brain MRI using optimal 3D filtering. Sci. Rep. 8 (1), 2132. https://doi.org/10.1038/s41598-018-19781-5.

Ballerini, L., McGrory, S., Valdés Hernández, M.D.C., Lovreglio, R., Pellegrini, E., MacGillivray, T., Muñoz Maniega, S., Henderson, R., Taylor, A., Bastin, M.E., Doubal, F., Trucco, E., Deary, I.J., Wardlaw, J., 2020c. Quantitative measurements of enlarged perivascular spaces in the brain are associated with retinal microvascular parameters in older community-dwelling subjects. Cereb. Circ. Cogn. Behav. 1, 100002 https://doi.org/10.1016/J.CCCB.2020.100002.

Barisano, G., Lynch, K.M., Sibilia, F., Lan, H., Shih, N.C., Sepehrband, F., Choupan, J., 2022a. Imaging perivascular space structure and function using brain MRI. Neuroimage 257, 119329. https://doi.org/10.1016/J.NEUROIMAGE.2022.119329.

Barisano, G., Sepehrband, F., Collins, H.R., Jillings, S., Jeurissen, B., Taylor, J.A., Schoenmaekers, C., De Laet, C., Rukavishnikov, I., Nosikova, I., Litvinova, L., Rumshiskaya, A., Annen, J., Sijbers, J., Laureys, S., Van Ombergen, A., Petrovichev, V., Sinitsyn, V., Pechenkova, E., Grishin, A., Zu Eulenburg, P., Law, M., Sunaert, S., Parizel, P.M., Tomilovskaya, E., Roberts, D.R., Wuyts, F.L., 2022b. The effect of prolonged spaceflight on cerebrospinal fluid and perivascular spaces of astronauts and cosmonauts. Proc. Natl. Acad. Sci. USA 119 (17), e2120439119. https://doi.org/10.1073/pnas.2120439119.

Barisano, G., Sheikh-Bahaei, N., Law, M., Toga, A.W., Sepehrband, F., 2021. Body mass index, time of day and genetics affect perivascular spaces in the white matter. J. Cereb. Blood Flow Metab. 41 (7), 1563–1578. https://doi.org/10.1177/0271678X20972856.

Barnes, A., Ballerini, L., Valdés Hernández, M.D.C., Chappell, F.M., Muñoz Maniega, S., Meijboom, R., Backhouse, E.V, Stringer, M.S., Duarte Coello, R., Brown, R., Bastin, M.E., Cox, S.R., Deary, I.J., Wardlaw, J.M., 2022. Topological relationships between perivascular spaces and progression of white matter hyperintensities: a pilot study in a sample of the Lothian Birth Cohort 1936. Front. Neurol. 13 https://doi.org/10.3389/fneur.2022.889884.

Berezuk, C., Ramirez, J., Gao, F., Scott, C.J.M., Huroy, M., Swartz, R.H., Murray, B.J., Black, S.E., Boulos, M.I., 2015. Virchow-Robin spaces: correlations with polysomnography-derived sleep parameters. Sleep 38 (6), 853–858. https://doi.org/10.5665/sleep.4726.

Bernal, J., Valdés-Hernández, M., Ballerini, L., Escudero, J., Jochems, A.C.C., Clancy, U., Doubal, F.N., Stringer, M.S., Thrippleton, M.J., Touyz, R.M., Wardlaw, J.M., 2020. A framework for jointly assessing and reducing imaging artefacts automatically using texture analysis and total variation optimisation for improving perivascular spaces quantification in brain magnetic resonance imaging. In B. W. Papież, A. I. L. Namburete, M. Yaqub, & J. A. Noble (Eds.). Medical Image Understanding and Analysis. Springer International Publishing, pp. 171–183. https://doi.org/10.1007/978-3-030-52791-4_14.

Bernal, J., Valdés-Hernández, M.D.C., Escudero, J., Duarte, R., Ballerini, L., Bastin, M.E., Deary, I.J., Thrippleton, M.J., Touyz, R.M., Wardlaw, J.M., 2022. Assessment of perivascular space filtering methods using a three-dimensional computational model. Magn. Reson. Imaging 93, 33–51. https://doi.org/10.1016/J.MRI.2022.07.016.

Bernal, J., Xu, W., Valdés-Hernández, M.D.C., Escudero, J., Jochems, A.C.C., Clancy, U., Doubal, F.N., Stringer, M.S., Thrippleton, M.J., Touyz, R.M., Wardlaw, J.M., 2021. Selective motion artefact reduction via radiomics and k-space reconstruction for improving perivascular space quantification in brain magnetic resonance imaging. In B. W. Papież, M. Yaqub, J. Jiao, A. I. L. Namburete, & J. A. Noble Medical Image Understanding and Analysis. Springer International Publishing, pp. 151–164. https://doi.org/10.1007/978-3-030-80432-9_12.

Boespflug, E.L., Schwartz, D.L., Lahna, D., Pollock, J., Iliff, J.J., Kaye, J.A., Rooney, W., Silbert, L.C., 2018. MR imaging–based multimodal autoidentification of perivascular spaces (mMAPS): automated morphologic segmentation of enlarged perivascular spaces at clinical field strength. Radiology 286 (2), 632–642. https://doi.org/10.1148/radiol.2017170205.

Boutinaud, P., Tsuchida, A., Laurent, A., Adonias, F., Hanifehlou, Z., Nozais, V., Verrecchia, V., Lampe, L., Zhang, J., Zhu, Y.C., Tzourio, C., Mazoyer, B., Joliot, M., 2021. 3D segmentation of perivascular spaces on T1-weighted 3 Tesla MR images with a convolutional autoencoder and a U-shaped neural network. Front. Neuroinform. 15. https://www.frontiersin.org/articles/10.3389/fninf.2021.641600.

Bown, C.W., Khan, O.A., Liu, D., Remedios, S.W., Pechman, K.R., Terry, J.G., Nair, S., Davis, L.T., Landman, B.A., Gifford, K.A., Hohman, T.J., Carr, J.J., Jefferson, A.L., 2023. Enlarged perivascular space burden associations with arterial stiffness and cognition. Neurobiol. Aging 124, 85–97. https://doi.org/10.1016/J.NEUROBIOLAGING.2022.10.014.

Butler, T., Zhou, L., Ozsahin, I., Wang, X.H., Garetti, J., Zetterberg, H., Blennow, K., Jamison, K., de Leon, M.J., Li, Y., Kuceyeski, A., Shah, S.A., 2023. Glymphatic clearance estimated using diffusion tensor imaging along perivascular spaces is reduced after traumatic brain injury and correlates with plasma neurofilament light, a biomarker of injury severity. Brain Commun. 5 (3), fcad134. https://doi.org/10.1093/braincomms/fcad134.

Cai, K., Tain, R., Das, S., Damen, F.C., Sui, Y., Valyi-Nagy, T., Elliott, M.A., Zhou, X.J., 2015. The feasibility of quantitative MRI of perivascular spaces at 7 T. J. Neurosci. Methods 256, 151–156. https://doi.org/10.1016/J.JNEUMETH.2015.09.001.

Chan, S.T., Mercaldo, N.D., Ravina, B., Hersch, S.M., Rosas, H.D., 2021. Association of dilated perivascular spaces and disease severity in patients with huntington disease. Neurology 96 (6), e890–e894. https://doi.org/10.1212/WNL.0000000000011121.

Charisis, S., Rashid, T., Liu, H., Ware, J.B., Jensen, P.N., Austin, T.R., Li, K., Fadaee, E., Hilal, S., Chen, C., Hughes, T.M., Romero, J.R., Toledo, J.B., Longstreth Jr., W.T., Hohman, T.J., Nasrallah, I., Bryan, R.N., Launer, L.J., Davatzikos, C., Seshadri, S., Heckbert, S.R., Habes, M., 2023. Assessment of risk factors and clinical importance of enlarged perivascular spaces by whole-brain investigation in the multi-ethnic study of atherosclerosis. JAMA Netw. Open 6 (4), e239196. https://doi.org/10.1001/jamanetworkopen.2023.9196.

Chen, Y., Wang, M., Su, S., Dai, Y., Zou, M., Lin, L., Qian, L., Li, X., Zhang, H., Liu, M., Chu, J., Yang, J., Yang, Z., 2024. Assessment of the glymphatic function in children with attention-deficit/hyperactivity disorder. Eur. Radiol. 34 (3), 1444–1452. https://doi.org/10.1007/s00330-023-10220-2.

Cheng, A.Y.T., Stubbs, J.L., Barr, A.M., Gicas, K.M., Su, W., Thornton, A.E., Lang, D.J., Hamzah, Y., Leonova, O., MacEwan, W.G., Rauscher, A., Honer, W.G., Panenka, W. J., 2022. Risk factors for hippocampal cavities in a marginally housed population. Hippocampus 32 (8), 567–576. https://doi.org/10.1002/hipo.23450.

Choi, Y., Nam, Y., Choi, Y., Kim, J., Jang, J., Ahn, K.J., Kim, B., Shin, N.Y., 2020. MRI-visible dilated perivascular spaces in healthy young adults: a twin heritability study. Hum. Brain Mapp. 41 (18), 5313–5324. https://doi.org/10.1002/hbm.25194.

Debette, S., Schilling, S., Duperron, M.G., Larsson, S.C., Markus, H.S., 2019. Clinical significance of magnetic resonance imaging markers of vascular brain injury: a systematic review and meta-analysis. JAMA Neurol. 76 (1), 81–94. https://doi.org/10.1001/jamaneurol.2018.3122.

DerSimonian, R., Laird, N., 1986. Meta-analysis in clinical trials. Control. Clin. Trials 7 (3), 177–188. https://doi.org/10.1016/0197-2456(86)90046-2.

Descombes, X., Kruggel, F., Wollny, G., Gertz, H.J., 2004. An object-based approach for detecting small brain lesions: application to Virchow-Robin spaces. IEEE Trans. Med. Imaging 23 (2), 246–255. https://doi.org/10.1109/TMI.2003.823061.

Donahue, E.K., Bui, V., Foreman, R.P., Duran, J.J., Venkadesh, S., Choupan, J., Van Horn, J.D., Alger, J.R., Jakowec, M.W., Petzinger, G.M., O'Neill, J., 2022. Magnetic resonance spectroscopy shows associations between neurometabolite levels and perivascular space volume in Parkinson's disease: a pilot and feasibility study. Neuroreport 33 (7), 291–296. https://doi.org/10.1097/WNR.0000000000001781.

Duarte Coello, R., Valdés Hernández, M., Bernal Moyano, J., Wardlaw, J., 2023. Cubic Bézier curve approximation for the estimation of perivascular spaces measurements in MRI brain scans. In G. Waiter, T. Lambrou, G. Leontidis, N. Oren, T. Morris, S. Gordon, J. McGowan, & C. Nicolson (Eds.). In: Proceedings of the 27th Conference on Medical Image Understanding and Analysis 2023. Frontiers Media, SA, pp. 168–173. https://doi.org/10.3389/978-2-8325-1231-9.

Duarte Coello, R., Valdés Hernández, M.D.C., Zwanenburg, J.J.M., van der Velden, M., Kuijf, H.J., De Luca, A., Moyano, J.B., Ballerini, L., Chappell, F.M., Brown, R., Jan Biessels, G., Wardlaw, J.M., 2024. Detectability and accuracy of computational measurements of in-silico and physical representations of enlarged perivascular spaces from magnetic resonance images. J. Neurosci. Methods 403, 110039. https://doi.org/10.1016/J.JNEUMETH.2023.110039.

Dubost, F., Adams, H., Bortsova, G., Ikram, M.A., Niessen, W., Vernooij, M., de Bruijne, M., 2019a. 3D regression neural network for the quantification of enlarged perivascular spaces in brain MRI. Med. Image Anal. 51, 89–100. https://doi.org/10.1016/J.MEDIA.2018.10.008.

Dubost, F., Adams, H., Yilmaz, P., Bortsova, G., Tulder, G.van, Ikram, M.A., Niessen, W., Vernooij, M.W., de Bruijne, M., 2020. Weakly supervised object detection with 2D and 3D regression neural networks. Med. Image Anal. 65, 101767 https://doi.org/10.1016/J.MEDIA.2020.101767.

Dubost, F., Bortsova, G., Adams, H., Ikram, A., Niessen, W.J., Vernooij, M., De Bruijne, M., 2017. GP-Unet: lesion detection from weak labels with a 3D regression network. In M. Descoteaux, L. Maier-Hein, A. Franz, P. Jannin, D. L. Collins, & S. Duchesne (Eds.). Medical Image Computing and Computer Assisted Intervention–MICCAI 2017. Springer International Publishing, pp. 214–221. https://doi.org/10.1007/978-3-319-66179-7_25.

Dubost, F., Dünnwald, M., Huff, D., Scheumann, V., Schreiber, F., Vernooij, M., Niessen, W., Skalej, M., Schreiber, S., Oeltze-Jafra, S., de Bruijne, M., 2019c. Automated quantification of enlarged perivascular spaces in clinical brain MRI across sites. In L. Zhou, D. Sarikaya, S. M. Kia, S. Speidel, A. Malpani, D. Hashimoto, M. Habes, T. Löfstedt, K. Ritter, & H. Wang (Eds.). OR 2.0 Context-Aware Operating Theaters and Machine Learning in Clinical Neuroimaging. Springer International Publishing, pp. 103–111. https://doi.org/10.1007/978-3-030-32695-1_12.

Dubost, F., Yilmaz, P., Adams, H., Bortsova, G., Ikram, M.A., Niessen, W., Vernooij, M., de Bruijne, M., 2019b. Enlarged perivascular spaces in brain MRI: automated quantification in four regions. Neuroimage 185, 534–544. https://doi.org/10.1016/J.NEUROIMAGE.2018.10.026.

Duering, M., Biessels, G.J., Brodtmann, A., Chen, C., Cordonnier, C., de Leeuw, F.E., Debette, S., Frayne, R., Jouvent, E., Rost, N.S., ter Telgte, A., Al-Shahi Salman, R., Backes, W.H., Bae, H.J., Brown, R., Chabriat, H., De Luca, A., deCarli, C., Dewenter, A., Doubal, F.N., Ewers, M., Field, T.S., Ganesh, A., Greenberg, S., helmer, K.G., Hilal, S., Jochems, A.C.C., Jokinin, H., Kuijf, H., Lam, B.Y.K., Lenberg, J., MacIntosh, B.J., Maillard, P., Mok, V.C.T., Pantoni, L., Rudilosso, S., Satizabal, C.L., Schirmer, M.D., Schmidt, R., Smith, C., Staals, J., Thrippleton, M.J., van Veluw, S.J., Vemuri, P., Wang, Y., Werring, D., Zedde, M., Aknyemi, R.O., Del Brutto, O.H., Markus, H.S., Zhu, Y-C, Smith, E.E., Dichgans, M., Wardlaw, J.M., 2023. Neuroimaging standards for research into small vessel disease–advances since 2013. Lancet Neurol 22 (7), 602–618. https://doi.org/10.1016/S1474-4422(23)00131-X.

Duperron, M.G., Knol, M.J., Le Grand, Q., Evans, T.E., Mishra, A., Tsuchida, A., Roshchupkin, G., Konuma, T., Trégouët, D.A., Romero, J.R., Frenzel, S., Luciano, M., Hofer, E., Bourgey, M., Dueker, N.D., Delgado, P., Hilal, S., Tankard, R.M., Dubost, F., Debette, S., 2023. Genomics of perivascular space burden unravels early mechanisms of cerebral small vessel disease. Nat. Med. 29 (4), 950–962. https://doi.org/10.1038/s41591-023-02268-w.

Evans, T.E., Knol, M.J., Schwingenschuh, P., Wittfeld, K., Hilal, S., Ikram, M.A., Dubost, F., van Wijnen, K.M.H., Katschnig, P., Yilmaz, P., de Bruijne, M., Habes, M., Chen, C., Langer, S., Völzke, H., Ikram, M.K., Grabe, H.J., Schmidt, R., Adams, H.H.H., Vernooij, M.W., 2023. Determinants of perivascular spaces in the general population. Neurology 100 (2), e107–e122. https://doi.org/10.1212/WNL.0000000000201349.

Francis, F., Ballerini, L., Wardlaw, J.M., 2019. Perivascular spaces and their associations with risk factors, clinical disorders and neuroimaging features: a systematic review and meta-analysis. Int. J. Stroke 14 (4), 359–371. https://doi.org/10.1177/1747493019830321.

Frangi, A.F., Niessen, W.J., Vincken, K.L., Viergever, M.A., 1998. Multiscale vessel enhancement filtering. In: [Medical Image Computing and Computer-Assisted Intervention - MICCAI'98], 1496. Springer-Verlag Berlin, Berlin, pp. 130–137. Wells, W. M., Colchester, A., and Delp, S., eds. https://link.springer.com/content/pdf/10.1007/BFb0056195.pdf.

González-Castro, V., Valdés Hernández, M.D.C., Armitage, P.A., Wardlaw, J.M., 2016a. Texture-based classification for the automatic rating of the perivascular spaces in brain MRI. Procedia Comput. Sci. 90, 9–14. https://doi.org/10.1016/J.PROCS.2016.07.003.

González-Castro, V., Valdés Hernández, M.D.C., Armitage, P.A., Wardlaw, J.M., 2016b. Automatic rating of perivascular spaces in brain MRI using bag of visual words. In A. Campilho & F. Karray (Eds.). Image Analysis and Recognition. Springer International Publishing, pp. 642–649. https://doi.org/10.1007/978-3-319-41501-7_72.

González-Castro, V., Valdés Hernández, M.D.C., Chappell, F.M., Armitage, P.A., Makin, S., Wardlaw, J.M., 2017. Reliability of an automatic classifier for brain enlarged perivascular spaces burden and comparison with human performance. Clin. Sci. 131 (13), 1465–1481. https://doi.org/10.1042/CS20170051.

Guerrero, R., Qin, C., Oktay, O., Bowles, C., Chen, L., Joules, R., Wolz, R., Valdés-Hernández, M.C., Dickie, D.A., Wardlaw, J., Rueckert, D., 2018. White matter hyperintensity and stroke lesion segmentation and differentiation using convolutional neural networks. NeuroImage Clin. 17, 918–934. https://doi.org/10.1016/J.NICL.2017.12.022.

Haddad, S.M.H., Scott, C.J.M., Ozzoude, M., Berezuk, C., Holmes, M., Adamo, S., Ramirez, J., Arnott, S.R., Nanayakkara, N.D., Binns, M., Beaton, D., Lou, W., Sunderland, K., Sujanthan, S., Lawrence, J., Kwan, D., Tan, B., Casaubon, L., Mandzia, J., Bartha, R., 2022. Comparison of diffusion tensor imaging metrics in normal-appearing white matter to cerebrovascular lesions and correlation with cerebrovascular disease risk factors and severity. Int. J. Biomed. Imaging 5860364. https://doi.org/10.1155/2022/5860364, 2022.

Hamilton, O.K.L., Cox, S.R., Ballerini, L., Bastin, M.E., Corley, J., Gow, A.J., Muñoz Maniega, S., Redmond, P., Valdés Hernández, M.D.C., Wardlaw, J.M., Deary, I.J., 2021a. Associations between total MRI-visible small vessel disease burden and domain-specific cognitive abilities in a community-dwelling older-age cohort. Neurobiol. Aging 105, 25–34. https://doi.org/10.1016/J.NEUROBIOLAGING.2021.04.007.

Hamilton, O.K.L., Cox, S.R., Okely, J.A., Conte, F., Ballerini, L., Bastin, M.E., Corley, J., Taylor, A.M., Page, D., Gow, A.J., Muñoz Maniega, S., Redmond, P., Valdés-Hernández, M.del C., Wardlaw, J.M., Deary, I.J., 2021b. Cerebral small vessel disease burden and longitudinal cognitive decline from age 73 to 82: the Lothian Birth Cohort 1936. Transl. Psychiatry 11 (1), 376. https://doi.org/10.1038/s41398-021-01495-4.

Hayden, M.R., 2023. Overview and new insights into the metabolic syndrome: risk factors and emerging variables in the development of type 2 diabetes and cerebrocardiovascular disease. Medicina 59 (3), 561. https://doi.org/10.3390/MEDICINA59030561 (B Aires) 2023*Vol. 59, Page 561*.

Hicks, A.J., Sinclair, B., Shultz, S.R., Pham, W., Silbert, L.C., Schwartz, D.L., Rowe, C.C., Ponsford, J.L., Law, M., Spitz, G., 2023. Associations of enlarged perivascular spaces with brain lesions, brain age, and clinical outcomes in chronic traumatic brain injury. Neurology 101 (1), e63–e73. https://doi.org/10.1212/WNL.0000000000207370.

Higgins, J.P., Thompson, S.G., Deeks, J.J., Altmany, D.G., 2003. Measuring inconsistency in meta-analyses. Br. Med. J. 327 (7414), 557–560. https://doi.org/10.1136/bmj.327.7414.557.

Hilal, S., Tan, C.S., Adams, H.H.H., Habes, M., Mok, V., Venketasubramanian, N., Hofer, E., Ikram, M.K., Abrigo, J., Vernooij, M.W., Chen, C., Hosten, N., Volzke, H., Grabe, H.J., Schmidt, R., Ikram, M.A., 2018. Enlarged perivascular spaces and cognition. Neurology 91 (9), e832–e842. https://doi.org/10.1212/WNL.0000000000006079.

Hou, Y., Park, S.H., Wang, Q., Zhang, J., Zong, X., Lin, W., Shen, D., 2017. Enhancement of perivascular spaces in 7 T MR image using haar transform of non-local cubes and block-matching filtering. Sci. Rep. 7 (1), 1–12. https://doi.org/10.1038/s41598-017-09336-5. *2017 7:1*.

Huang, P., Zhang, R., Jiaerken, Y., Wang, S., Yu, W., Hong, H., Lian, C., Li, K., Zeng, Q., Luo, X., Yu, X., Xu, X., Wu, X., Zhang, M., 2021a. Deep white matter hyperintensity is associated with the dilation of perivascular space. J. Cereb. Blood Flow Metab. 41 (9), 2370–2380. https://doi.org/10.1177/0271678X211002279.

Huang, P., Zhu, Z., Zhang, R., Wu, X., Jiaerken, Y., Wang, S., Yu, W., Hong, H., Lian, C., Li, K., Zeng, Q., Luo, X., Xu, X., Yu, X., Yang, Y., Zhang, M., 2021b. Factors associated with the dilation of perivascular space in healthy elderly subjects. Front. Aging Neurosci. 13. https://www.frontiersin.org/articles/10.3389/fnagi.2021.624732.

Hupfeld, K.E., Richmond, S.B., McGregor, H.R., Schwartz, D.L., Luther, M.N., Beltran, N. E., Kofman, I.S., De Dios, Y.E., Riascos, R.F., Wood, S.J., Bloomberg, J.J., Mulavara, A.P., Silbert, L.C., Iliff, J.J., Seidler, R.D., Piantino, J., 2022. Longitudinal MRI-visible perivascular space (PVS) changes with long-duration spaceflight. Sci. Rep. 12 (1), 1–13. https://doi.org/10.1038/s41598-022-11593-y. *2022 12:1*.

Jian, X., Xu, F., Yang, M., Zhang, M., Yun, W., 2023. Correlation between enlarged perivascular space and brain white matter hyperintensities in patients with recent small subcortical infarct. Brain Behav. 13 (9), e3168. https://doi.org/10.1002/brb3.3168.

Jie, W., Lin, G., Liu, Z., Zhou, H., Lin, L., Liang, G., Ou, M., Lin, M., 2020. The relationship between enlarged perivascular spaces and cognitive function: a meta-analysis of observational studies. Front. Pharmacol. 11. https://www.frontiersin.org/journals/pharmacology/articles/10.3389/fphar.2020.00715.

Jokinen, H., Koikkalainen, J., Laakso, H.M., Melkas, S., Nieminen, T., Brander, A., Korvenoja, A., Rueckert, D., Barkhof, F., Scheltens, P., Schmidt, R., Fazekas, F., Madureira, S., Verdelho, A., Wallin, A., Wahlund, L.O., Waldemar, G., Chabriat, H., Hennerici, M., O'Brien, J., Inzitari, D., Lotjonen, J., Pantoni, L., Erkinjuntti, T., 2020. Global burden of small vessel disease–related brain changes on MRI predicts cognitive and functional decline. Stroke 51 (1), 170–178. https://doi.org/10.1161/STROKEAHA.119.026170.

Jung, E., Chikontwe, P., Zong, X., Lin, W., Shen, D., Park, S.H., 2019. Enhancement of perivascular spaces using densely connected deep convolutional neural network. IEEE Access. 7, 18382–18391. https://doi.org/10.1109/ACCESS.2019.2896911.

Jung, E., Zong, X., Lin, W., Shen, D., Park, S.H., 2018. Enhancement of Perivascular Spaces Using a Very Deep 3D Dense Network. Springer, pp. 18–25. https://doi.org/10.1007/978-3-030-00320-3_3.

Kamagata, K., Andica, C., Takabayashi, K., Saito, Y., Taoka, T., Nozaki, H., Kikuta, J., Fujita, S., Hagiwara, A., Kamiya, K., Wada, A., Akashi, T., Sano, K., Nishizawa, M., Hori, M., Naganawa, S., Aoki, S., Alzheimer's Disease Neuroimaging Initiative, 2022. Association of MRI indices of glymphatic system with amyloid deposition and cognition in mild cognitive impairment and alzheimer disease. Neurology 99 (24), e2648–e2660. https://doi.org/10.1212/WNL.0000000000201300.

Karvelas, N., Oh, B., Wang, E., Cobigo, Y., Tsuei, T., Fitzsimons, S., Ehrenberg, A., Geschwind, M., Schwartz, D., Kramer, J., Ferguson, A.R., Miller, B.L., Silbert, L., Rosen, H., Elahi, F.M., 2023. Enlarged perivascular spaces are associated with white matter injury, brain atrophy, cognitive decline and markers of inflammation in an autosomal dominant vascular neurodegenerative disease (CADASIL). bioRxiv, 553732. https://doi.org/10.1101/2023.08.17.553732, 2023.08.17.

Kern, K.C., Nasrallah, I.M., Bryan, R.N., Reboussin, D.M., Wright, C.B., 2023. Intensive systolic blood pressure treatment remodels brain perivascular spaces: a secondary analysis of the Systolic Pressure Intervention Trial (SPRINT). NeuroImage Clin. 40, 103513 https://doi.org/10.1016/J.NICL.2023.103513.

Kim, H.G., Shin, N.Y., Nam, Y., Yun, E., Yoon, U., Lee, H.S., Ahn, K.J., 2023a. MRI-visible dilated perivascular space in the brain by age: the human connectome project. Radiology 306 (3), e213254. https://doi.org/10.1148/radiol.213254.

Kim, J.Y., Nam, Y., Kim, S., Shin, N.Y., Kim, H.G., 2023b. MRI-visible perivascular spaces in the neonatal brain. Radiology 307 (2), e221314. https://doi.org/10.1148/radiol.221314.

Kruggel, F., Chalopin, C., Descombes, X., Kovalev, V., Rajapakse, J.C., 2002. Segmentation of pathological features in MRI brain datasets. In: Proceedings of the 9th International Conference on Neural Information Processing: Computational Intelligence for the E-Age, PICONIP 2002, 5, pp. 2673–2677. https://doi.org/10.1109/ICONIP.2002.1201981.

Lan, H., Lynch, K.M., Custer, R., Shih, N.C., Sherlock, P., Toga, A.W., Sepehrband, F., Choupan, J., 2023. Weakly supervised perivascular spaces segmentation with salient guidance of Frangi filter. Magn. Reson. Med. 89 (6), 2419–2431. https://doi.org/10.1002/mrm.29593.

Langan, M.T., Smith, D.A., Verma, G., Khegai, O., Saju, S., Rashid, S., Ranti, D., Markowitz, M., Belani, P., Jette, N., Mathew, B., Goldstein, J., Kirsch, C.F.E., Morris, L.S., Becker, J.H., Delman, B.N., Balchandani, P., 2022. Semi-automated segmentation and quantification of perivascular spaces at 7 Tesla in COVID-19. Front. Neurol. 13. https://www.frontiersin.org/journals/neurology/articles/10.3389/fneur.2022.846957.

Lee, B., Shin, N.Y., Park, C., Nam, Y., Lim, S.M., Ahn, K.J., 2021. Spatial similarity of MRI-visible perivascular spaces in healthy young adult twins. Preprint. https://doi.org/10.21203/rs.3.rs-1052220/v1.

Li, X., Ruan, C., Wu, Y., Musa, M., Zibrila, A.I., Zhang, Z., Salimeen, M., 2022. Variances of quantifying of Virchow–Robin spaces detecting the different functional status of glymphatic system in simple febrile seizures affected by seizures duration. Medicine (52), 101. https://doi.org/10.1097/MD.0000000000032606 (Baltimore).

Li, X.Y., Xie, J.J., Wang, J.H., Bao, Y.F., Dong, Y., Gao, B., Shen, T., Huang, P.Y., Ying, H. C., Xu, H., Roe, A.W., Lai, H.Y., Wu, Z.Y., 2023. Perivascular spaces relate to the course and cognition of Huntington's disease. Transl. Neurodegener. 12 (1), 30. https://doi.org/10.1186/s40035-023-00359-9.

Lian, C., Zhang, J., Liu, M., Zong, X., Hung, S.C., Lin, W., Shen, D., 2018. Multi-channel multi-scale fully convolutional network for 3D perivascular spaces segmentation in 7T MR images. Med. Image Anal. 46, 106–117. https://doi.org/10.1016/J.MEDIA.2018.02.009.

Liu, C., Habib, T., Salimeen, M., Pradhan, A., Singh, M., Wang, M., Wu, F., Zhang, Y., Gao, L., Yang, G., Li, X., Yang, J., 2020. Quantification of visible Virchow–Robin spaces for detecting the functional status of the glymphatic system in children with newly diagnosed idiopathic generalized epilepsy. Seizure 78, 12–17. https://doi.org/10.1016/J.SEIZURE.2020.02.015.

Lynch, K.M., Sepehrband, F., Toga, A.W., Choupan, J., 2023. Brain perivascular space imaging across the human lifespan. Neuroimage 271, 120009. https://doi.org/10.1016/J.NEUROIMAGE.2023.120009.

Lysen, T.S., Yilmaz, P., Dubost, F., Ikram, M.A., de Bruijne, M., Vernooij, M.W., Luik, A.I., 2022. Sleep and perivascular spaces in the middle-aged and elderly population. J. Sleep Res. 31 (2), e13485. https://doi.org/10.1111/jsr.13485.

Martinez-Ramirez, S., Van Rooden, S., Charidimou, A., Van Opstal, A.M., Wermer, M., Edip Gurol, M., Terwindt, G., Van Der Grond, J., Greenberg, S.M., Van Buchem, M., Viswanathan, A., 2018. Perivascular spaces volume in sporadic and hereditary (Dutch-type) cerebral amyloid angiopathy. Stroke 49 (8), 1913–1919. https://doi.org/10.1161/STROKEAHA.118.021137.

McGuinness, L., Higgins, J., 2020. Risk-of-bias VISualization (robvis): an R package and Shiny web app for visualizing risk-of-bias assessments. Res. Synth. Methods 1–7. https://doi.org/10.1002/jrsm.1411.

Moses, J., Sinclair, B., Law, M., O'Brien, T.J., Vivash, L., 2023. Automated methods for detecting and quantitation of enlarged perivascular spaces on MRI. J. Magn. Reson. Imaging 57 (1), 11–24. https://doi.org/10.1002/jmri.28369.

Moses, J., Sinclair, B., Schwartz, D.L., Silbert, L.C., O'Brien, T.J., Law, M., Vivash, L., 2022. Perivascular spaces as a marker of disease severity and neurodegeneration in patients with behavioral variant frontotemporal dementia. Front. Neurosci. 16 https://doi.org/10.3389/FNINS.2022.1003522.

Niazi, M., Karaman, M., Das, S., Zhou, X.J., Yushkevich, P., Cai, K., 2018. Quantitative MRI of perivascular spaces at 3T for early diagnosis of mild cognitive impairment. Am. J. Neuroradiol. 39 (9), 1622–1628. https://doi.org/10.3174/AJNR.A5734.

Pantoni, L., Basile, A.M., Pracucci, G., Asplund, K., Bogousslavsky, J., Chabriat, H., Erkinjuntti, T., Fazekas, F., Ferro, J.M., Hennerici, M., O'Brien, J., Scheltens, P., Visser, M.C., Wahlund, L.O., Waldemar, G., Wallin, A., Inzitari, D., 2004. Impact of age-related cerebral white matter changes on the transition to disability – the LADIS study: rationale, design and methodology. Neuroepidemiology 24 (1–2), 51–62. https://doi.org/10.1159/000081050.

Park, C., Shin, N.Y., Nam, Y., Yoon, U., Ahn, K., Lee, S.K., 2023. Characteristics of perivascular space dilatation in normal aging. Hum. Brain Mapp. 44 (8), 3232–3240. https://doi.org/10.1002/hbm.26277.

Park, S.H., Zong, X., Gao, Y., Lin, W., Shen, D., 2016. Segmentation of perivascular spaces in 7 T MR image using auto-context model with orientation-normalized features. Neuroimage 134, 223–235. https://doi.org/10.1016/J.NEUROIMAGE.2016.03.076.

Paz, J., Pérez, M., Schelkens, P., Rodríguez, J., 2009. Impact of JPEG 2000 compression on lesion detection in MR imaging. Med. Phys. 36 (11), 4967–4976. https://doi.org/10.1118/1.3233783.

Pereira, S., Mariz, J.A., Sousa, N., Correia, J.H., Silva, C.A., 2015. A fully automatic tool for counting Virchow-Robin spaces in magnetic resonance imaging for lacunar stroke study. In: Proceedings of the 2nd International Conference on Bioimaging, Part of 8th International Joint Conference on Biomedical Engineering Systems and Technologies, Bioimaging 2015, 2015. BIOSTEC, pp. 69–75. https://doi.org/10.5220/0005199700690075.

Perosa, V., Oltmer, J., Munting, L.P., Freeze, W.M., Auger, C.A., Scherlek, A.A., van der Kouwe, A.J., Iglesias, J.E., Atzeni, A., Bacskai, B.J., Viswanathan, A., Frosch, M.P., Greenberg, S.M., van Veluw, S.J., 2022. Perivascular space dilation is associated with vascular amyloid-β accumulation in the overlying cortex. Acta Neuropathol. 143 (3), 331–348. https://doi.org/10.1007/S00401-021-02393-1/FIGURES/6.

Pham, W., Lynch, M., Spitz, G., O'Brien, T., Vivash, L., Sinclair, B., Law, M., 2022. A critical guide to the automated quantification of perivascular spaces in magnetic resonance imaging. Front. Neurosci. 16 https://doi.org/10.3389/fnins.2022.1021311.

Piantino, J., Boespflug, E.L., Schwartz, D.L., Luther, M., Morales, A.M., Lin, A., Fossen, R. V., Silbert, L., Nagel, B.J., 2020. Characterization of MR imaging–visible perivascular spaces in the white matter of healthy adolescents at 3T. Am. J. Neuroradiol. 41 (11), 2139. https://doi.org/10.3174/ajnr.A6789.

Piantino, J., Schwartz, D.L., Luther, M., Newgard, C., Silbert, L., Raskind, M., Pagulayan, K., Kleinhans, N., Iliff, J., Peskind, E., 2021. Link between mild traumatic brain injury, poor sleep, and magnetic resonance imaging: visible perivascular spaces in veterans. J. Neurotrauma 38 (17), 2391–2399. https://doi.org/10.1089/neu.2020.7447.

Ramirez, J., Berberian, S.A., Breen, D.P., Gao, F., Ozzoude, M., Adamo, S., Scott, C.J.M., Berezuk, C., Yhap, V., Mestre, T.A., Marras, C., Tartaglia, M.C., Grimes, D., Jog, M., Kwan, D., Tan, B., Binns, M.A., Arnott, S.R., Symons, S., Masellis, M., Black, S.E., Lang, A.E., Bartha, R., ONDRI Investigators, 2022. Small and large magnetic resonance imaging–visible perivascular spaces in the basal ganglia of Parkinson's disease patients. Mov. Disord. 37 (6), 1304–1309. https://doi.org/10.1002/mds.29010.

Ramirez, J., Berezuk, C., McNeely, A.A., Scott, C.J.M., Gao, F., Black, S.E., 2015. Visible Virchow-Robin spaces on magnetic resonance imaging of alzheimer's disease patients and normal elderly from the sunnybrook dementia study. J. Alzheimer's Dis. 43, 415–424. https://doi.org/10.3233/JAD-132528.

Ramirez, J., Gibson, E., Quddus, A., Lobaugh, N.J., Feinstein, A., Levine, B., Scott, C.J.M., Levy-Cooperman, N., Gao, F.Q., Black, S.E., 2011. Lesion explorer: a comprehensive segmentation and parcellation package to obtain regional volumetrics for subcortical hyperintensities and intracranial tissue. Neuroimage 54 (2), 963–973. https://doi.org/10.1016/J.NEUROIMAGE.2010.09.013.

Ranti, D.L., Warburton, A.J., Rutland, J.W., Dullea, J.T., Markowitz, M., Smith, D.A., Kligler, S.Z.K., Rutter, S., Langan, M., Arrighi-Allisan, A., George, I., Verma, G., Murrough, J.W., Delman, B.N., Balchandani, P., Morris, L.S., 2022. Perivascular spaces as a marker of psychological trauma in depression: a 7-Tesla MRI study. Brain Behav. 12 (7), 32598. https://doi.org/10.1002/brb3.2598.

Ranti, D., Murrough, J., Balchandani, P., Morris, L., 2021. Trauma exposure and perivascular spaces in depression: a 7-Tesla MRI study. Biol. Psychiatry 89 (9), S188–S189. https://doi.org/10.1016/J.BIOPSYCH.2021.02.478.

Rashid, T., Liu, H., Ware, J.B., Li, K., Romero, J.R., Fadaee, E., Nasrallah, I.M., Hilal, S., Bryan, R.N., Hughes, T.M., Davatzikos, C., Launer, L., Seshadri, S., Heckbert, S.R., Habes, M., 2023. Deep learning based detection of enlarged perivascular spaces on brain MRI. Neuroimage Rep. 3 (1), 100162 https://doi.org/10.1016/J.YNIRP.2023.100162.

Remedios, S.W., Roy, S., Bermudez, C., Patel, M.B., Butman, J.A., Landman, B.A., Pham, D.L., 2020. Distributed deep learning across multisite datasets for generalized CT hemorrhage segmentation. Med. Phys. 47 (1), 89–98. https://doi.org/10.1002/mp.13880.

Sáenz de Villaverde Cortabarría, A., Zhang, J.F., Valdés Hernández, M.D.C., Clancy, U., Sakka, E., Ferguson, K.J., Wiseman, S., Hewins, W., Jaime García, D., Stringer, M., Thrippleton, M., Chappell, F., Doubal, F., Wu, Y.C., Wardlaw, J.M., 2023. Paranasal sinuses opacification on magnetic resonance imaging in relation to brain health in sporadic small vessel disease–systematic review and pilot analysis. J. Neurol. Sci. 451, 120735 https://doi.org/10.1016/J.JNS.2023.120735.

Sato, Y., Nakajima, S., Shiraga, N., Atsumi, H., Yoshida, S., Koller, T., Gerig, G., Kikinis, R., 1998. Three-dimensional multi-scale line filter for segmentation and visualization of curvilinear structures in medical images. Med. Image Anal. 2 (2), 143–168. https://doi.org/10.1016/S1361-8415(98)80009-1.

Schreiber, S., Bernal, J., Arndt, P., Schreiber, F., Müller, P., Morton, L., Braun-Dullaeus, R.C., Valdés-Hernández, M.D.C., Duarte, R., Wardlaw, J.M., Meuth, S.G., Mietzner, G., Vielhaber, S., Dunay, I.R., Dityatev, A., Jandke, S., Mattern, H., 2023. Brain vascular health in ALS is mediated through motor cortex microvascular integrity. Cells 12 (6). https://doi.org/10.3390/cells12060957.

Schwartz, D.L., Boespflug, E.L., Lahna, D.L., Pollock, J., Roese, N.E., Silbert, L.C., 2019. Autoidentification of perivascular spaces in white matter using clinical field strength

T1 and FLAIR MR imaging. Neuroimage 202, 116126. https://doi.org/10.1016/J.NEUROIMAGE.2019.116126.
Sepehrband, F., Barisano, G., Sheikh-Bahaei, N., Cabeen, R.P., Choupan, J., Law, M., Toga, A.W., 2019. Image processing approaches to enhance perivascular space visibility and quantification using MRI. Sci. Rep. 9 (1), 12351. https://doi.org/10.1038/s41598-019-48910-x.
Sepehrband, F., Barisano, G., Sheikh-Bahaei, N., Choupan, J., Cabeen, R.P., Lynch, K.M., Crawford, M.S., Lan, H., Mack, W.J., Chui, H.C., Ringman, J.M., Toga, A.W., 2021. Volumetric distribution of perivascular space in relation to mild cognitive impairment. Neurobiol. Aging 99, 28–43. https://doi.org/10.1016/J.NEUROBIOLAGING.2020.12.010.
Shih, N.C., Barisano, G., Lincoln, K.D., Mack, W.J., Sepehrband, F., Choupan, J., 2023. Effects of sleep on brain perivascular space in a cognitively healthy population. Sleep Med. 111, 170–179. https://doi.org/10.1016/J.SLEEP.2023.09.024.
Sibilia, F., Sheikh-Bahaei, N., Mack, W.J., Choupan, J., 2023. Perivascular spaces in Alzheimer's disease are associated with inflammatory, stress-related, and hypertension biomarkers. bioRxiv, 543504. https://doi.org/10.1101/2023.06.02.543504, 2023.06.02.
Smeijer, D., Ikram, M.K., Hilal, S., 2019. Enlarged perivascular spaces and dementia: a systematic review. J. Alzheimer's Dis. 72, 247–256. https://doi.org/10.3233/JAD-190527.
Smith, D.A., Verma, G., Ranti, D., Markowitz, M., Balchandani, P., Morris, L., 2020. Perivascular space semi-automatic segmentation (PVSSAS): a tool for segmenting, viewing and editing perivascular spaces. bioRxiv 11 (16), 385336. https://doi.org/10.1101/2020.11.16.385336, 2020.
Sotgiu, M.A., Lo Jacono, A., Barisano, G., Saderi, L., Cavassa, V., Montella, A., Crivelli, P., Carta, A., Sotgiu, S., 2023. Brain perivascular spaces and autism: clinical and pathogenic implications from an innovative volumetric MRI study. Front. Neurosci. 17 https://doi.org/10.3389/fnins.2023.1205489.
Spijkerman, J.M., Zwanenburg, J.J.M., Bouvy, W.H., Geerlings, M.I., Biessels, G.J., Hendrikse, J., Luijten, P.R., Kuijf, H.J., 2022. Automatic quantification of perivascular spaces in T2-weighted images at 7 T MRI. Cereb. Circ. Cogn. Behav. 3, 100142 https://doi.org/10.1016/J.CCCB.2022.100142.
Sudre, C.H., Gomez Anson, B., Lane, C.D., Jimenez, D., Haider, L., Varsavsky, T., Smith, L., Jäger, R.H., Jorge Cardoso, U.M., 2019. 3D multirater RCNN for multimodal multiclass detection and characterisation of extremely small objects. Proc. Mach. Learn. Res. 102, 447–456.
Sudre, C. H., van Wijnen, K., Dubost, F., Adams, H., Atkinson, D., Barkhof, F., Birhanu, M. A., Bron, E. E., Camarasa, R., Chaturvedi, N., Chen, Y., Chen, Z., Chen, S., Dou, Q., Evans, T., Ezhov, I., Gao, H., Sanguesa, M. G., Gispert, J. D., Gómez Ansón, B., Hughes, A.D., Ikram, M.A., Ingala, S., Jaeger, H.R., Kofler, F., Kuijf, H.J., Kutnar, D., Lee, M., Li, B., Lorenzini, L., Menze, B., Molinuevo, J.L., Pan, Y., Puybareau, E., Rehwald, R., Su, R., Shi, P., Smith, L., Tillin, T., Tochon, G., Urien, H., van der Velden, B.H.M., van der Velpen, I.F., Wiestler, B., Wolters, F.J., Yilmaz, P., de Groot, M., Vernooij, M.W., de Bruijne, M. (2022). Where is VALDO? VAscular Lesions Detection and segmentatiOn challenge at MICCAI 2021. 10.48550/arXiv.2208.07167.
Tachibana, A., Iga, J., Tatewaki, Y., Thyreau, B., Chen, H., Ozaki, T., Yoshida, T., Yoshino, Y., Shimizu, H., Mori, T., Furuta, Y., Shibata, M., Ohara, T., Hata, J., Taki, Y., Nakaji, S., Maeda, T., Ono, K., Mimura, M., Nakashima, K., Takebayashi, M., Ninomiya, T., Ueno, S., 2024. Late-life high blood pressure and enlarged perivascular spaces in the putaminal regions of community-dwelling Japanese older persons. J. Geriatr. Psychiatry Neurol. 37 (1), 61–72. https://doi.org/10.1177/08919887231195235.
Uchiyama, Y., Asano, T., Hara, T., Fujita, H., Hoshi, H., Iwama, T., Kinosada, Y., 2009. CAD Scheme for differential diagnosis of lacunar infarcts and normal Virchow-Robin spaces on brain MR images. In O. Dössel & W. C. Schlegel (Eds.). World Congress on Medical Physics and Biomedical Engineering. Springer Berlin Heidelberg, Munich, Germany, pp. 126–128. https://doi.org/10.1007/978-3-642-03904-1_36. *September 7 - 12,* 2009.
Uchiyama, Y., Kunieda, T., Asano, T., Kato, H., Hara, T., Kanematsu, M., Iwama, T., Hoshi, H., Kinosada, Y., Fujita, H., 2008. Computer-aided diagnosis scheme for classification of lacunar infarcts and enlarged Virchow-Robin spaces in brain MR images. In: Proceedings of the 30th Annual International Conference of the IEEE Engineering in Medicine and Biology Society, pp. 3908–3911. https://doi.org/10.1109/IEMBS.2008.4650064.
Valdés Hernández, M.D.C., Abu-Hussain, J., Qiu, X., Priller, J., Parra Rodríguez, M., Pino, M., Báez, S., Ibáñez, A., 2019. Structural neuroimaging differentiates vulnerability from disease manifestation in colombian families with Huntington's disease. Brain Behav. 9 (8), e01343. https://doi.org/10.1002/brb3.1343.
Valdés Hernández, M.D.C., Ballerini, L., Glatz, A., Muñoz Maniega, S., Gow, A.J., Bastin, M.E., Starr, J.M., Deary, I.J., Wardlaw, J.M, 2020. Perivascular spaces in the centrum semiovale at the beginning of the 8th decade of life: effect on cognition and associations with mineral deposition. Brain imaging Behav. 14 (5), 1865–1875. https://doi.org/10.1007/s11682-019-00128-1.
Valdés Hernández, M.D.C., Duarte Coello, R., Xu, W., Bernal, J., Cheng, Y., Ballerini, L., Wiseman, S.J., Chappell, F.M., Clancy, U., Jaime García, D., Arteaga Reyes, C., Zhang, J.F., Liu, X., Hewins, W., Stringer, M., Doubal, F., Thrippleton, M.J., Jochems, A., Brown, R., Wardlaw, J.M., 2024a. Influence of threshold selection and image sequence in *in-vivo* segmentation of enlarged perivascular spaces. J. Neurosci. Methods 403, 110037. https://doi.org/10.1016/J.JNEUMETH.2023.110037.
Valdés Hernández, M.D.C., Ferguson, K.J., Loon, P., Kirkwood, G., Zhang, J.F., Amft, N., Ralston, S.H., Wu, Y.C., Wardlaw, J.M., Wiseman, S.J., 2024b. Paranasal sinus occupancy assessed from magnetic resonance images–associations with clinical indicators in patients with systemic lupus erythematosus. Rheumatology 63 (1), 149–157. https://doi.org/10.1093/rheumatology/kead185.
Valdés Hernández, M.D.C., Piper, R.J., Wang, X., Deary, I.J., Wardlaw, J.M., 2013. Towards the automatic computational assessment of enlarged perivascular spaces on brain magnetic resonance images: a systematic review. J. Magn. Reson. Imaging 38 (4), 774–785. https://doi.org/10.1002/jmri.24047.
van Wijnen, K.M.H., Dubost, F., Yilmaz, P., Ikram, M.A., Niessen, W.J., Adams, H., Vernooij, M.W., de Bruijne, M., 2019. Automated lesion detection by regressing intensity-based distance with a neural network. In D. Shen, T. Liu, T. M. Peters, L. H. Staib, C. Essert, S. Zhou, P.-T. Yap, & A. Khan (Eds.). Medical Image Computing and Computer Assisted Intervention–MICCAI 2019. Springer International Publishing, pp. 234–242. https://doi.org/10.1007/978-3-030-32251-9_26.
Vikner, T., Karalija, N., Eklund, A., Malm, J., Lundquist, A., Gallewicz, N., Dahlin, M., Lindenberger, U., Riklund, K., Bäckman, L., Nyberg, L., Wåhlin, A., 2022. 5-year associations among cerebral arterial pulsatility, perivascular space dilation, and white matter lesions. Ann. Neurol. https://doi.org/10.1002/ANA.26475.
Wang, J., Tian, Y., Qin, C., Meng, L., Feng, R., Xu, S., Zhai, Y., Liang, D., Zhang, R., Tian, H., Liu, H., Chen, Y., Fu, Y., Chen, P., Zhu, Q., Teng, J., Wang, X., 2023. Impaired glymphatic drainage underlying obstructive sleep apnea is associated with cognitive dysfunction. J. Neurol. 270 (4), 2204–2216. https://doi.org/10.1007/s00415-022-11530-z.
Wang, S., Huang, P., Zhang, R., Hong, H., Jiaerken, Y., Lian, C., Yu, X., Luo, X., Li, K., Zeng, Q., Xu, X., Yu, W., Wu, X., Zhang, M., 2021. Quantity and morphology of perivascular spaces: associations with vascular risk factors and cerebral small vessel disease. J. Magn. Reson. Imaging 54 (4), 1326–1336. https://doi.org/10.1002/jmri.27702.
Wang, X., Chappell, F.M., Valdes Hernandez, M., Lowe, G., Rumley, A., Shuler, K., Doubal, F., Wardlaw, J.M., 2016a. Endothelial function, inflammation, thrombosis, and basal ganglia perivascular spaces in patients with stroke. J. Stroke Cerebrovasc. Dis. 25 (12), 2925–2931. https://doi.org/10.1016/j.jstrokecerebrovasdis.2016.08.007.
Wang, X., Valdés Hernández, M.D.C., Doubal, F., Chappell, F.M, Piper, R.J., Deary, I.J., Wardlaw, J.M., 2016b. Development and initial evaluation of a semi-automatic approach to assess perivascular spaces on conventional magnetic resonance images. J. Neurosci. Methods 257, 34–44. https://doi.org/10.1016/J.JNEUMETH.2015.09.010.
Wardlaw, J.M., Benveniste, H., Nedergaard, M., Zlokovic, B.V., Mestre, H., Lee, H., Doubal, F.N., Brown, R., Ramirez, J., MacIntosh, B.J., Tannenbaum, A., Ballerini, L., Rungta, R.L., Boido, D., Sweeney, M., Montagne, A., Charpak, S., Joutel, A., Black, S. E., Smith, K.J., colleagues from the Fondation Leducq Transatlantic Network of Excellence on the Role of the Perivascular Space in Cerebral Small Vessel Disease, 2020. Perivascular spaces in the brain: anatomy, physiology and pathology. Nature Rev. Neurol. 16 (3), 137–153. https://doi.org/10.1038/s41582-020-0312-z.
Wardlaw, J.M., Smith, E.E., Biessels, G.J., Cordonnier, C., Fazekas, F., Frayne, R., Lindley, R.I., O'Brien, J.T., Barkhof, F., Benavente, O.R., Black, S.E., Brayne, C., Breteler, M., Chabriat, H., DeCarli, C., de Leeuw, F.E., Doubal, F., Duering, M., Fox, N.C., Greenberg, S., Hachinski, V., Kilimann, I., Mok, V., van Oostenbrugge, R., Pantoni, L., Speck, O., Stephan, B.C.M., Teipel, S., Viswanathan, A., Werring, D., Chen, C., Smith, C., van Buchem, M., Norrving, B., Gorelick, P.B., Dichgans, M., 2013. Neuroimaging standards for research into small vessel disease and its contribution to ageing and neurodegeneration. Lancet Neurol. 12 (8), 822–838. https://doi.org/10.1016/S1474-4422(13)70124-8.
Whiting, P.F., Rutjes, A.W.S., Westwood, M.E., Mallett, S., Deeks, J.J., Reitsma, J.B., Leeflang, M.M.G., Sterne, J.A.C., Bossuyt, P.M.M., 2011. QUADAS-2: a revised tool for the quality assessment of diagnostic accuracy studies. Ann. Intern. Med. 155 (8), 529–536. https://doi.org/10.7326/0003-4819-155-8-201110180-00009.
Williamson, B.J., Khandwala, V., Wang, D., Maloney, T., Sucharew, H., Horn, P., Haverbusch, M., Alwell, K., Gangatirkar, S., Mahammedi, A., Wang, L.L., Tomsick, T., Gaskill-Shipley, M., Cornelius, R., Khatri, P., Kissela, B., Vagal, A., 2022. Automated grading of enlarged perivascular spaces in clinical imaging data of an acute stroke cohort using an interpretable, 3D deep learning framework. Sci. Rep. 12 (1), 788. https://doi.org/10.1038/s41598-021-04287-4.
Wuerfel, J., Haertle, M., Waiczies, H., Tysiak, E., Bechmann, I., Wernecke, K.D., Zipp, F., Paul, F., 2008. Perivascular spaces–MRI marker of inflammatory activity in the brain? Brain 131 (9), 2332–2340. https://doi.org/10.1093/brain/awn171.
Yang, E., Gonuguntla, V., Moon, W.J., Moon, Y., Kim, H.J., Park, M., Kim, J.H., 2021. Direct rating estimation of enlarged perivascular spaces (EPVS) in brain MRI using deep neural network. Appl. Sci. 11 (20) https://doi.org/10.3390/app11209398.
Yu, D., Liang, N., Zebarth, J., Shen, Q., Ozzoude, M., Goubran, M., Rabin, J.S., Ramirez, J., Scott, C.J.M., Gao, F., Bartha, R., Symons, S., Haddad, S.M.H., Berezuk, C., Tan, B., Kwan, D., Hegele, R.A., Dilliott, A.A., Nanayakkara, N.D., 2023. Soluble epoxide hydrolase derived linoleic acid oxylipins, small vessel disease markers, and neurodegeneration in stroke. J. Am. Heart. Assoc. 12 (1), e026901 https://doi.org/10.1161/JAHA.122.026901.
Yushkevich, P.A., Piven, J., Hazlett, H.C., Smith, R.G., Ho, S., Gee, J.C., Gerig, G., 2006. User-guided 3D active contour segmentation of anatomical structures: significantly improved efficiency and reliability. Neuroimage 31 (3), 1116–1128. https://doi.org/10.1016/J.NEUROIMAGE.2006.01.015.
Zebarth, J., Kamal, R., Perlman, G., Ouk, M., Xiong, L.Y., Yu, D., Lin, W.Z., Ramirez, J., Masellis, M., Goubran, M., MacIntosh, B.J., Black, S.E., Cogo-Moreira, H., Scott, C.J. M., Bartha, R., Symons, S., Haddad, S.M.H., Ozzoude, M., Nanayakkara, N., Beaton, D., Arnott, S., Doulatshahi, D., Swartz, R.H., Saposnik, G., Grimes, D., Lang, A., Fischer, C.E., Frank, A., Kumar, S., Pollock, B.G., Tang-Wai, D., Finger, E., Rabin, J.S., Swardfager, W., 2023. Perivascular spaces mediate a relationship between diabetes and other cerebral small vessel disease markers in cerebrovascular and neurodegenerative diseases. J. Stroke Cerebrovasc. Dis. 32 (9) https://doi.org/10.1016/j.jstrokecerebrovasdis.2023.107273.

Zhang, J., Gao, Y., Park, S.H., Zong, X., Lin, W., Shen, D., 2016. Segmentation of perivascular spaces using vascular features and structured random forest from 7T MR image. In L. Wang, E. Adeli, Q. Wang, Y. Shi, & H.-I. Suk (Eds.). Machine Learning in Medical Imaging. Springer International Publishing, pp. 61–68. https://doi.org/10.1007/978-3-319-47157-0_8.

Zhang, J., Gao, Y., Park, S.H., Zong, X., Lin, W., Shen, D., 2017. Structured learning for 3-D perivascular space segmentation using vascular features. IEEE Trans. Biomed. Eng. 64 (12), 2803–2812. https://doi.org/10.1109/TBME.2016.2638918.

Zhu, Y.C., Tzourio, C., Soumaré, A., Mazoyer, B., Dufouil, C., Chabriat, H., 2010. Severity of dilated virchow-robin spaces is associated with age, blood pressure, and MRI markers of small vessel disease. Stroke 41 (11), 2483–2490. https://doi.org/10.1161/STROKEAHA.110.591586.

Zong, X., Lian, C., Jimenez, J., Yamashita, K., Shen, D., Lin, W., 2020. Morphology of perivascular spaces and enclosed blood vessels in young to middle-aged healthy adults at 7T: dependences on age, brain region, and breathing gas. Neuroimage 218, 116978. https://doi.org/10.1016/J.NEUROIMAGE.2020.116978.

Zong, X., Nanavati, S., Hung, S.C., Li, T., Lin, W., 2021. Effects of motion and retrospective motion correction on the visualization and quantification of perivascular spaces in ultrahigh resolution T2-weighted images at 7T. Magn. Reson. Med. 86 (4), 1944–1955. https://doi.org/10.1002/mrm.28847.

Zong, X., Park, S.H., Shen, D., Lin, W., 2016. Visualization of perivascular spaces in the human brain at 7 T: sequence optimization and morphology characterization. Neuroimage 125, 895–902. https://doi.org/10.1016/J.NEUROIMAGE.2015.10.078.